VOLUME TWO

NASA SP-290

TURBINE DESIGN and APPLICATION

NATIONAL AERONAUTICS AND SPACE ADMINISTRATION

NASA SP-290

TURBINE DESIGN and APPLICATION

VOLUME TWO

Edited by Arthur J. Glassman
Lewis Research Center

Scientific and Technical Information Office 1973
NATIONAL AERONAUTICS AND SPACE ADMINISTRATION
Washington, D.C.

For sale by the Superintendent of Documents
U.S. Government Printing Office, Washington, D.C. 20402
Price $1.80 Stock Number 3300-00535
Library of Congress Catalog Card Number 79-185105

PREFACE

NASA has an interest in turbines related primarily to aeronautics and space applications. Airbreathing turbine engines provide jet and turboshaft propulsion, as well as auxiliary power for aircraft. Propellant-driven turbines provide rocket propulsion and auxiliary power for spacecraft. Closed-cycle turbine engines using inert gases, organic fluids, and metal fluids have been studied for providing long-duration electric power for spacecraft. Other applications of current interest for turbine engines include land-vehicle (cars, trucks, buses, trains, etc.) propulsion power and ground-based electrical power.

In view of the turbine-system interest and efforts at Lewis Research Center, a course entitled "Turbine Design and Application" was presented during 1968–69 as part of the In-House Graduate Study Program. The course was somewhat revised and again presented in 1972–73. Various aspects of turbine technology were covered including thermodynamic and fluid-dynamic concepts, fundamental turbine concepts, velocity diagrams, losses, blade aerodynamic design, blade cooling, mechanical design, operation, and performance.

The notes written and used for the course have been revised and edited for publication. Such a publication can serve as a foundation for an introductory turbine course, a means for self-study, or a reference for selected topics. The first volume presented the material covering thermodynamic and fluid-dynamic concepts, fundamental turbine concepts, and velocity diagram design. This second volume presents the material related to blade aerodynamic design and turbine energy losses.

Any consistent set of units will satisfy the equations presented. Two commonly used consistent sets of units and constant values are given after the symbol definitions. These are the SI units and the U.S. customary units. A single set of equations covers both sets of units by including all constants required for the U.S. customary units and defining as unity those not required for the SI units.

ARTHUR J. GLASSMAN

CONTENTS

CHAPTER 4

Blade Design

By Warner L. Stewart and
Arthur J. Glassman

The design of a turbine consists of three major steps. The first is the determination of the overall requirements of flow, work, and speed. These are usually established by the particular application. The second step is the evolution of velocity diagrams consistent with the desired efficiency and/or number of stages. This was discussed in chapter 3. The third step is the design of the blading that will produce the flow angles and velocities required by the velocity diagrams. This step involves the determination of the size, shape, and spacing of the blades.

This chapter covers some of the more important aspects of blade design. The height of the blade is set by the overall requirements of flow, speed, and inlet state conditions and the selected velocity diagram, which dictates the fluid state conditions throughout the turbine. The blade chord is usually selected to be a minimum value consistent with mechanical considerations. The chord must be long enough to allow accurate fabrication and assure structural integrity during operation. The selection of blade spacing, which can be expressed nondimensionally as solidity (ratio of chord to spacing) or axial solidity (ratio of axial chord to spacing), involves many considerations that will be discussed in the first part of this chapter. Blade profile design, which includes blade exit and inlet geometries as well as the connecting surface profiles, is then discussed in the last part of this chapter. Channel flow theory, which is the basis for the analytical procedures used to accomplish the profile design, is discussed in the next chapter.

SOLIDITY

One of the important aspects of turbine blading design is the selection of the blade solidity, which is the ratio of chord or axial chord to spacing. A minimum value is usually desired from the standpoint of reducing weight, cooling flow, and cost. However, chord reduction is limited by mechanical considerations, and increased spacing eventually results in decreased blade efficiency due to separated flow. This section will concern itself with the aerodynamic factors affecting solidity selection. The discussion will include the effect of velocity diagram requirements on solidity and the relation between blade loading and solidity. Also included will be a description of advanced blading concepts that are being studied for use to suppress separation and thereby reduce the permissible solidity.

Effect of Velocity Diagrams on Solidity

Figure 4–1 shows a typical set of blade inlet and exit diagrams as well as the static-pressure distribution around a blade. The velocities in this figure are shown as absolute velocities. The discussion in this chapter pertains to rotor blade rows as well as to stator blade rows. When referring to a rotor, we must use relative rather than absolute velocities in the equations and figures. Since in this chapter we are concerned with blade rows rather than with stages, the angle convention will differ slightly from that used in previous chapters. The exit tangential-velocity component and flow angle are taken as negative values. The inlet values are positive if the inlet and exit tangential-velocity components are in opposite directions, and negative if in the same direction.

If one considers the two-dimensional flow through a passage of unit height between two blades, then the tangential force exerted by the fluid as it flows from blade inlet (subscript 1) to exit (subscript 2) is

$$F_u = \frac{1}{g} s\rho_2 V_{x,2}(V_{u,1} - V_{u,2}) \tag{4–1}$$

where

F_u	tangential force, N; lb
g	conversion constant, 1; 32.17 (lbm)(ft)/(lbf)(sec^2)
s	blade spacing, m; ft
ρ	density, kg/m^3; lb/ft^3
V_x	axial component of velocity, m/sec; ft/sec
V_u	tangential component of velocity, m/sec; ft/sec

This tangential force exerted by the fluid must be the same as the force due to the static-pressure distribution around the blade, as was discussed in chapter 2. The lower part of figure 4–1 shows a typical static-pressure

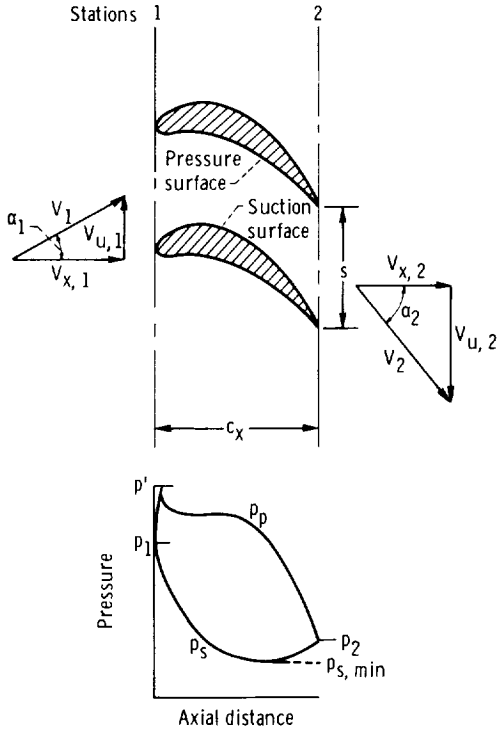

FIGURE 4–1. Typical blade-row velocity diagrams and surface static-pressure distribution.

distribution around the blade row as a function of axial distance. The area between the two curves represents the total blade force acting on the flow in the tangential direction. Thus,

$$F_u = c_x \int_0^1 (p_p - p_s)\, d\left(\frac{x}{c_x}\right) \tag{4–2}$$

where

c_x axial chord, m; ft
p_p pressure-surface static pressure, N/m^2; lb/ft^2
p_s suction-surface static pressure, N/m^2; lb/ft^2
x axial distance, m; ft

The axial solidity, σ_x, is

$$\sigma_x = \frac{c_x}{s} \tag{4–3}$$

Substituting equations (4–1) and (4–2) into equation (4–3) then yields

$$\sigma_x = \frac{\rho_2 V_{x,2}(V_{u,1} - V_{u,2})}{g \int_0^1 (p_p - p_s)\, d\left(\frac{x}{c_x}\right)} \tag{4–4}$$

At this point, we introduce two tangential loading coefficients that have been used to relate the actual blade loading to an ideal blade loading. The first is the widely used coefficient introduced by Zweifel (ref. 1). This coefficient is based on an ideal loading that assumes (1) the static pressure on the pressure surface to be constant and equal to the inlet total pressure and (2) the static pressure on the suction surface to be constant and equal to the exit static pressure. In equation form,

$$\psi_z = \frac{\int_0^1 (p_p - p_s)\, d\left(\frac{x}{c_x}\right)}{p_1' - p_2} \tag{4–5}$$

where

ψ_z Zweifel loading coefficient
p_1' inlet total pressure, N/m^2; lb/ft^2
p_2 exit static pressure, N/m^2; lb/ft^2

The second coefficient is similarly defined except that the assumed constant static pressure on the suction surface is equal to the minimum value of static pressure (see fig. 4–1) on that surface. This loading coefficient can never exceed a value of 1, and for all practical purposes, it must always be less than 1. The Zweifel coefficient, on the other hand, can exceed a value of 1. In equation form, this second loading coefficient ψ is defined as

$$\psi = \frac{\int_0^1 (p_p - p_s)\, d\left(\frac{x}{c_x}\right)}{p_1' - p_{s,min}} \tag{4–6}$$

where $p_{s,min}$ is the minimum static pressure on the suction surface in N/m^2 or lb/ft^2.

The velocity components in terms of velocity and flow angle are expressed as

$$V_u = V \sin \alpha \tag{4–7}$$

and

$$V_x = V \cos \alpha \tag{4–8}$$

where

V fluid velocity, m/sec; ft/sec
α fluid flow angle, deg

Substituting equations (4–5) or (4–6), (4–7), and (4–8) into equation (4–4) and using the trigonometric relation $\sin 2\alpha = 2 \sin \alpha \cos \alpha$ yields

$$\sigma_x = \left(\frac{\frac{1}{2g} \rho_2 V_2^2}{p_1' - p_{s,min}} \right) \frac{(K-1) \sin 2\alpha_2}{\psi} = \left(\frac{\frac{1}{2g} \rho_2 V_2^2}{p_1' - p_2} \right) \frac{(K-1) \sin 2\alpha_2}{\psi_z} \tag{4–9}$$

where K is the ratio of tangential velocity component ($V_{u,1}$) at the blade inlet to that ($V_{u,2}$) at the blade exit.

Derivation of incompressible-flow relations.—Relations involving solidity, velocity diagrams, and loading are usually evolved by assuming incompressible flow with no loss. With this assumption, density ρ is constant, and Bernoulli's equation

$$p' = p + \frac{1}{2g} \rho V^2 \tag{4–10}$$

can be used. Substituting equation (4–10) into equation (4–9) yields

$$\sigma_x = \frac{(K-1) \sin 2\alpha_2}{\psi \left(\frac{V_{max}^2}{V_2^2} \right)} = \frac{(K-1) \sin 2\alpha_2}{\psi_z} \tag{4–11}$$

where V_{max} is the velocity on the suction surface where $p = p_{s,min}$.

Let us now define a suction-surface diffusion parameter D_s as

$$D_s \equiv \frac{V_{max}^2}{V_2^2} \tag{4–12}$$

Many parameters of this type have been used to represent a measure of the deceleration of the flow on the suction surface. This deceleration is an indication of the susceptibility of the flow on the blade to separate. Using this definition (eq. (4–12)) in equation (4–11) yields

$$\sigma_x = \frac{(K-1) \sin 2\alpha_2}{\psi D_s} = \frac{(K-1) \sin 2\alpha_2}{\psi_z} \tag{4–13}$$

Equation (4–13) shows that the solidity parameter $\sigma_x \psi D_s$ or $\sigma_x \psi_z$ is constant for each particular velocity-diagram requirement. Since loading coefficient ψ, which cannot exceed a value of 1, does not vary greatly, it can be seen that decreasing solidity results primarily in increased suction-

surface diffusion (higher D_s), the consequence of which will be discussed later in this chapter. The solidity parameter is plotted against the tangential velocity ratio K for several values of exit flow angle in figure 4–2(a). A value of $K=0$ represents a reaction blade with axial inlet, a value of $K=-1$ represents an impulse blade, and a value of $K<-1$ represents a negative reaction blade. Positive values of K represent inlet and exit tangential velocities in the same direction and are encountered primarily in the tip sections of rotor blades. As seen from equation (4–13), solidity parameter is equal to zero for all exit angles for $K=1$. This represents the case where there is no turning of the flow. The solidity parameter increases with decreasing K values. Thus, if excessive suction-surface diffusion is to be avoided, solidity must increase as the velocity diagrams move from reaction toward impulse. It can be seen that for any given value of K, a maximum value of solidity parameter is obtained with an exit angle of 45°.

Equation (4–13) can be modified to a function of the inlet and exit angles to yield the equation derived in reference 1.

$$\sigma_x=\frac{2}{\psi_z}\frac{\cos\alpha_2}{\cos\alpha_1}\sin(\alpha_1-\alpha_2) \tag{4–14}$$

For brevity, this is expressed only in terms of the coefficient ψ_z. Equation (4–14) shows that the solidity parameter $\sigma_x\psi_z$ can be expressed in terms of the flow angles only. Solidity parameter is plotted against exit flow angle for several values of the inlet flow angle in figure 4–2(b). For a given exit angle, solidity parameter increases with increasing inlet angle. In the region of most interest ($\alpha_1>0°$, $\alpha_2<-45°$), solidity parameter for each inlet angle decreases with decreasing exit angle.

A third relation can be evolved, this one in terms of blade reaction R, which was defined in chapter 2 as

$$R\equiv 1-\frac{V_1^2}{V_2^2} \tag{4–15}$$

Substituting equation (4–8) into equation (4–15) yields

$$R=1-\left(\frac{\cos\alpha_2}{\cos\alpha_1}\right)^2 \tag{4–16}$$

for the two-dimensional, incompressible-flow case, where $V_{x,1}=V_{x,2}$. Substitution of equation (4–16) back into equation (4–14) then yields

$$\sigma_x=\frac{2}{\psi_z}\sqrt{1-R}\sin\Delta\alpha \tag{4–17}$$

where $\Delta\alpha$ is $\alpha_1-\alpha_2$.

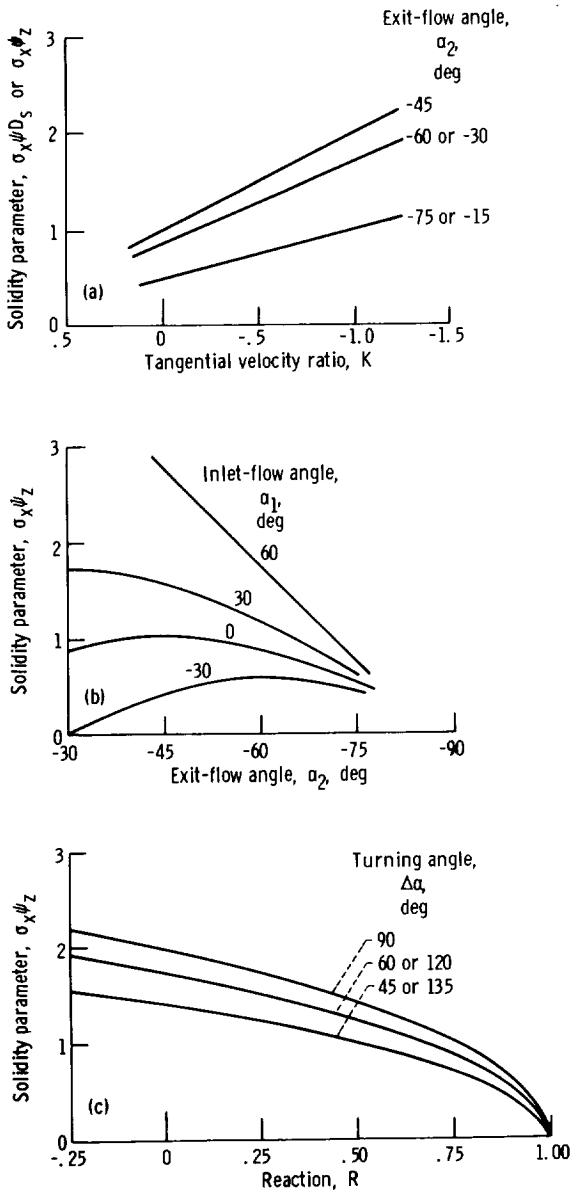

(a) Effect of tangential-velocity ratio and exit-flow angle.
(b) Effect of exit- and inlet-flow angles.
(c) Effect of reaction and turning angle.

FIGURE 4–2.—Effect of velocity diagrams on solidity.

Equation (4–17) expresses the solidity parameter in terms of blade reaction and turning angle. The solidity parameter is plotted against reaction for several values of turning angle in figure 4–2(c). It can be seen that, as indicated previously, the solidity parameter decreases with increasing reaction. The solidity parameter is a maximum for a turning angle of 90° and varies little with turning unless very high or very low turnings are used.

Radial variation.—Chapter 3 discussed the radial variations in velocity diagrams that must occur in order to satisfy both the varying blade speed and radial equilibrium. Since axial solidity was shown to vary with varying velocity diagrams, there will be a radial variation in the desired value of axial solidity. The nature of this radial variation will be illustrated by an example. Consider a single-stage turbine having axial inlet and exit flows (zero inlet and exit swirls), constant axial velocities, a constant hub-to-tip-radius ratio of 0.7, an impulse rotor hub with a stator-hub exit flow angle of −70°, and free-vortex swirl distribution. For this case, the flow angles at the hub and tip and the corresponding solidity-parameter values computed from equation (4–14) are shown in the following table:

	Stator			Rotor		
	Inlet angle, deg	Exit angle, deg	Solidity parameter, $\sigma_z\psi_z$	Inlet angle, deg	Exit angle, deg	Solidity parameter, $\sigma_z\psi_z$
Hub	0	−70	0.64	54	−54	1.90
Tip	0	−62	.83	−2	−63	.79

Note again that the angle convention being used in this chapter is somewhat different from that of previous chapters. Herein, stator exit angles are negative. Assume that the loading coefficient ψ_z is to be maintained constant radially. This is a reasonably desirable condition, and the assumption enables us to proportion solidity directly to the solidity parameter.

Let us now determine how the hub and tip values of solidity parameter shown in the preceding table can be made physically consistent. The axial solidity variation in any blade row must be inversely proportional to radius (because blade spacing is directly proportional to radius) and

directly proportional to axial chord. For the stator, the axial solidity parameter at the hub is 0.64. If axial chord were held constant, then the corresponding tip value of the axial solidity parameter would be $0.64 \times 0.7 = 0.45$, which is almost half of the desired value of 0.83. Therefore, a considerable axial taper from tip to hub is often used so that the axial chord can increase with radius and yield the higher solidities desired at the tip.

In the case of the rotor, the axial solidity parameter at the hub is 1.90. If axial chord were held constant, then the corresponding tip value of the axial solidity parameter would be $1.90 \times 0.7 = 1.33$, which is still larger than the desired value of 0.79. Therefore, axial taper from hub to tip is often used in rotor blades so that axial chord can decrease with increasing radius and yield the lower solidities desired at the tip. Taper from hub to tip in the rotor is not only aerodynamically desirable, but is also mechanically desirable from the standpoint of reducing blade stress. To simplify fabrication in many cases, especially for smaller turbines, axial taper is not used, and there results a radial variation in loading coefficient. With the axial solidity selected on the basis of the mean-section velocity diagrams, this radial variation in loading coefficient in many cases, especially those where the blading is not highly loaded, will not have a severe effect on turbine performance.

Effect of compressibility.—The term

$$\frac{\frac{1}{2g}\rho_2 V_2^2}{p_1' - p_{s,min}}$$

in equation (4–9) reduces to $1/D_s$ for incompressible flow conditions, as shown by equation (4–13). For a compressible flow case having the same loading coefficient ψ as for incompressible flow, division of equation (4–9) by equation (4–13) yields

$$\frac{\sigma_x}{\sigma_{x,inc}} = \frac{\frac{1}{2g}\rho_2 V_2^2 D_s}{p_1' - p_{s,min}} \tag{4–18}$$

where $\sigma_{x,inc}$ is the incompressible flow value as determined from an equation such as (4–13), (4–14), or (4–17). By introducing the relations between critical velocity ratio, density, and pressure (eqs. (1–3), (1–52), (1–61), (1–63), and (1–64)) and using the definition of D_s (eq. (4–12)), equation (4–18) is modified to

$$\frac{\sigma_x}{\sigma_{x,inc}} = \frac{\dfrac{\gamma}{\gamma+1}\left[1-\dfrac{\gamma-1}{\gamma+1}\left(\dfrac{V}{V_{cr}}\right)_2^2\right]^{1/(\gamma-1)}\left(\dfrac{V}{V_{cr}}\right)_2^2 D_s}{1-\left[1-\dfrac{\gamma-1}{\gamma+1}\left(\dfrac{V}{V_{cr}}\right)_2^2 D_s\right]^{\gamma/(\gamma-1)}} \tag{4-19}$$

where

γ ratio of specific heat at constant pressure to specific heat at constant volume

V_{cr} critical velocity, m/sec; ft/sec

Then, by using binomial expansion and by neglecting the secondary terms, equation (4–19) can be approximated as

$$\frac{\sigma_x}{\sigma_{x,inc}} = 1-\frac{\left(\dfrac{V}{V_{cr}}\right)_2^2}{\gamma+1}+\frac{D_s\left(\dfrac{V}{V_{cr}}\right)_2^2}{2(\gamma+1)} \tag{4-20}$$

The approximation represented by equation (4–20) is quite good for $(V/V_{cr})_2$ values up to about 1. The solidity ratio $\sigma_x/\sigma_{x,inc}$ is plotted against suction-surface diffusion parameter for several values of critical velocity ratio in figure 4–3. The compressibility effect becomes more pronounced as D_s either increases or decreases from a value of 2. At $D_s = 2$, there is no compressibility effect for any value of $(V/V_{cr})_2$. For D_s values of less than 2, the required solidity decreases with increasing values of $(V/V_{cr})_2$.

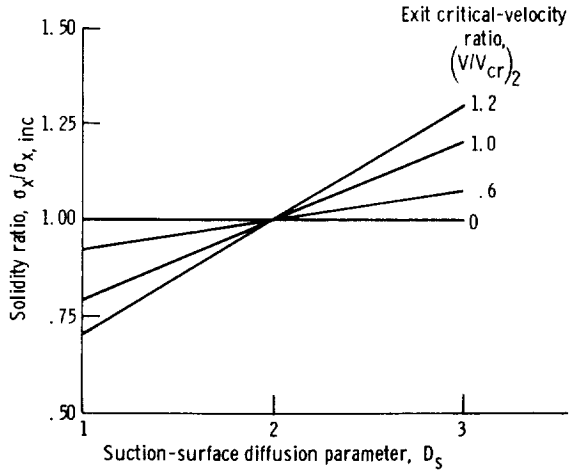

FIGURE 4–3.—Effect of compressibility on axial solidity.

For D_s values of more than 2, a region that is only of academic interest because it is beyond the limits of good design practice, the solidity ratio increases with increasing $(V/V_{cr})_2$. Experience has shown that D_s values should be maintained below about 2 to avoid excessive losses.

Relation of Loss to Solidity

It is well recognized that the loading of a turbine blade or of a compressor blade is an important function of both solidity and reaction. Correlation of blade loss with a compressor diffusion parameter was described in reference 2 and is used widely within the compressor field. This parameter includes two terms, one reflecting reaction and the second reflecting turning and solidity. An analogous diffusion parameter was evolved for the case of the turbine in reference 3, where an overall diffusion parameter is defined as the ratio of the sum of the decelerations in kinetic energy on the suction and pressure surfaces to the exit kinetic energy. If it is assumed that the pressure surface minimum velocity is low enough to neglect $(V_{p,min}=0)$, then the overall diffusion parameter is defined as

$$D \equiv \frac{V_{max}^2 - V_2^2 + V_1^2}{V_2^2} \tag{4-21}$$

With the use of the definitions of D_s (eq. (4–12)) and R (eq. (4–15)), equation (4–21) reduces to

$$D = D_s - R \tag{4-22}$$

As seen from equation (4–13),

$$\psi_x = \psi D_s \tag{4-23}$$

Substitution of equations (4–23) and (4–14) into equation (4–22) then yields

$$D = \frac{2}{\sigma_x \psi} \frac{\cos \alpha_2}{\cos \alpha_1} \sin \Delta\alpha - R \tag{4-24}$$

This relation is like that for compressors, with the two terms involving reaction and solidity.

Attempts have been made to correlate turbine blade loss with both overall (ref. 4) and suction-surface (ref. 5) diffusion parameters. A definite trend of increasing loss with increasing diffusion was established, but complete correlation could not be obtained. Such a correlation of blade loss with diffusion parameter alone would not be expected, since different values of reaction and solidity giving the same value of D do not give the same loss.

Consider first the effect of reaction on loss, as shown qualitatively in figure 4–4(a). As reaction is reduced from a relatively high value near

unity, there occurs a gradual increase in blade loss. Further reductions in reaction to negative values cause the loss to increase rapidly. This variation in loss with reaction is caused by the change in boundary-layer characteristics (which are discussed in chapter 6) as the nature of the flow varies from highly accelerating to diffusing. The negative reaction regime, although desired in many applications, is usually avoided because of the high loss encountered when conventional blading is used.

The effect of solidity on loss is indicated in figure 4–4(b). A minimum loss occurs at some optimum solidity. As solidity increases, the amount of frictional surface area per unit flow is increasing. As solidity is reduced, on the other hand, the loss per unit surface area is increasing because of the increased surface diffusion required. A minimum loss occurs as a result of these opposing factors. The value of the suction-surface diffusion

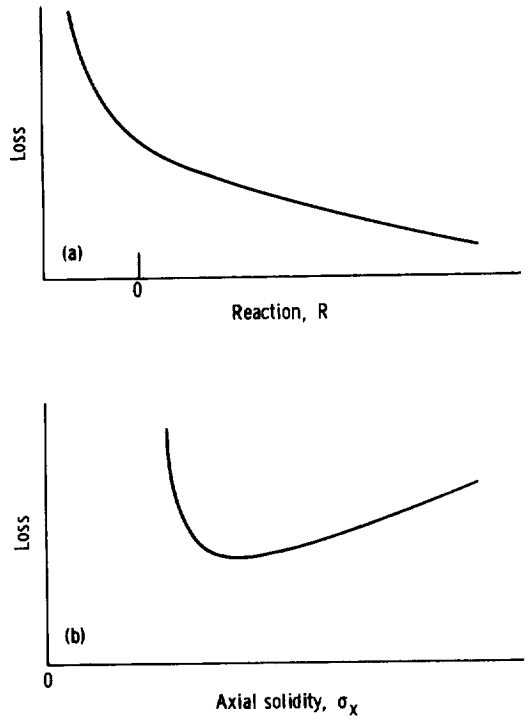

(a) Reaction.
(b) Solidity.
FIGURE 4–4.—Loss trend with reaction and solidity.

parameter corresponding to the optimum solidity is a function of many factors such as Reynolds number, shape of suction surface velocity distribution, and rate of turning. In general, as mentioned previously, values not exceeding about 2.0 are used.

Selection of Optimum Solidity

Both analytical and experimental attempts have been made to identify optimum solidity. According to reference 1, minimum loss occurs when the Zweifel loading coefficient ψ_x is equal to 0.8. By using this value in equation (4–14), optimum axial solidity can be determined as a function of the blade-row inlet and exit flow angles, and this is plotted in figure 4–5(a) for a wide range of angles. The dashed (long-short) curve represents the locus of points for impulse blading.

In order to determine the optimum values in terms of actual solidity, it is necessary to determine the stagger angle α_s, because

$$\sigma \approx \frac{\sigma_x}{\cos \alpha_s} \tag{4–25}$$

An analytical blade model was used in reference 6 to relate stagger angle to the flow angles and the axial solidity. Thus, optimum values of actual solidity were obtained as a function of inlet and exit angles, as shown in figure 4–5(b). The authors of reference 6 compared an optimum solidity determined in this way with the data of reference 7, where efficiency was measured with four different rotor solidities, as shown here in figure 4–6. The solidity determined as optimum in reference 6 from a figure such as figure 4–5(b) is seen to be quite close to that yielding maximum efficiency for this case.

Loss coefficients based on cascade data are presented in reference 8 as a function of pitch/chord ratio (inverse of solidity) and exit angle for reaction blades ($\alpha_1 = 0$) and impulse blades ($\alpha_1 = -\alpha_2$). These coefficients, in relative terms, are replotted here in figure 4–7 against solidity for various exit angles. These curves indicate the importance of selecting optimum solidity. For the larger (more negative) values of exit angle, the curves are rather flat in the region of minimum loss, and some deviation in solidity from optimum does not cause any significant increase in loss. As the exit angle gets smaller, the minimum loss region becomes more pronounced and the loss penalties become more severe as solidity departs from the optimum value. It must be recognized that curves such as those of figure 4–7 are usually obtained by using a given blade shape and varying the spacing. Thus, the blade shape and resultant velocity distribution cannot be optimized for each solidity, and the significance of such a correlation is somewhat clouded.

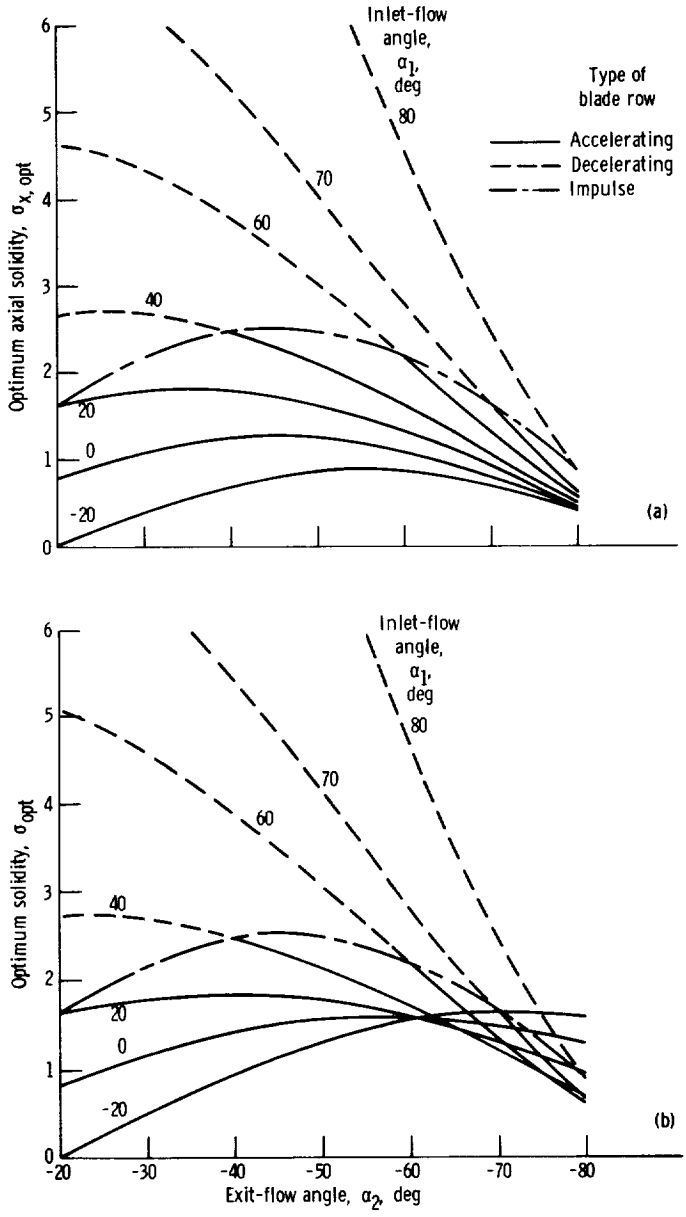

(a) Axial solidity.
(b) Actual solidity.

FIGURE 4–5.—Effect of inlet and exit angles on optimum solidity. Zweifel loading coefficient $\psi_z = 0.8$.

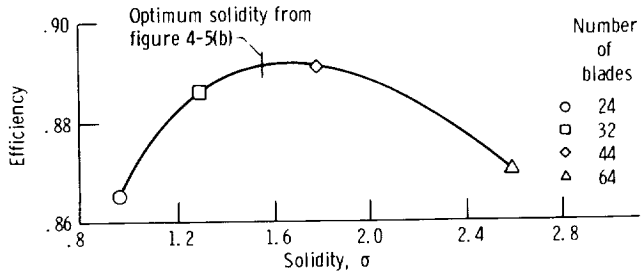

FIGURE 4–6. –Variation of efficiency with solidity for four turbines of reference 7.

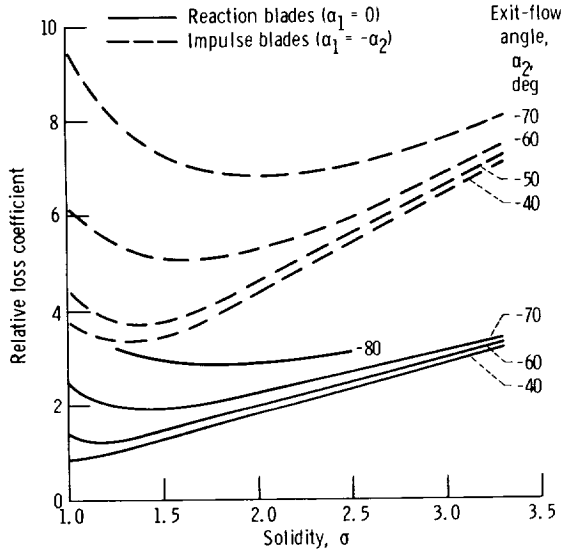

FIGURE 4–7. Effect of solidity and exit angle on blade-loss coefficient.

The optimum solidities obtained from the cascade results shown in figure 4–7 are plotted against exit angle in figure 4–8 and are compared with those obtained analytically and shown in figure 4–5(b). It is obvious that agreement between the experimental and the analytical results is not good for most exit-angle values. Although the experimental and the analytical curves do cross each other for both the reaction ($\alpha_1 = 0$) blading and the impulse ($\alpha_1 = -\alpha_2$) blading, the indicated variations in optimum solidity with exit angle are just not similar. All that can be said at this time is that the analytical results involve many assumptions, the experimental results pertain to one particular blade profile, and there are many factors that act to determine optimum solidity in a manner that we do

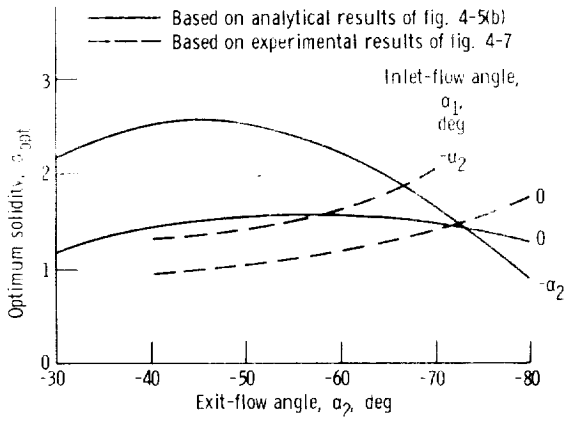

FIGURE 4-8. Comparison of optimum solidities.

not yet fully understand. Analytical results, such as those of figure 4-5, are more frequently used to determine optimum solidity than are experimental results, such as those shown in figure 4-7. Current design practice is to use ψ_s values of 0.9 to 1.0, which is slightly higher than the 0.8 recommended in reference 1.

Ultralow-Solidity Blading

In the past, the limitation to reductions in solidity has been separation occurring on the suction surface of the blade. To achieve lower solidities, some modifications in blade concept must be utilized such that separation is suppressed and the associated high losses do not occur.

The treatment of the boundary layer in the region of separation is one approach to reduced solidity. Such treatments could include removing the boundary layer by suction, energizing the boundary layer by blowing, or increasing the turbulence of the boundary layer by use of turbulators on the blade. Certain of these concepts have been explored with marginal success. Two alternate blade concepts that have, perhaps, better potential are the tandem and jet-flap blades, which are illustrated in figure 4-9. Studies applying the boundary-layer treatment concepts as well as the alternate blade concepts to stator blades and rotor blades are summarized in references 9 and 10, respectively. Cascade tests of low-solidity plain, tandem, and jet-flap blades are presented in references 11 to 14. Turbine test results with low-solidity tandem and jet-flap rotors are presented in references 15 and 16, respectively.

The tandem blade operates on the principle that, although a high value of suction-surface diffusion is utilized (perhaps 2), the front foil is terminated at about the point of separation. The remaining diffusion then

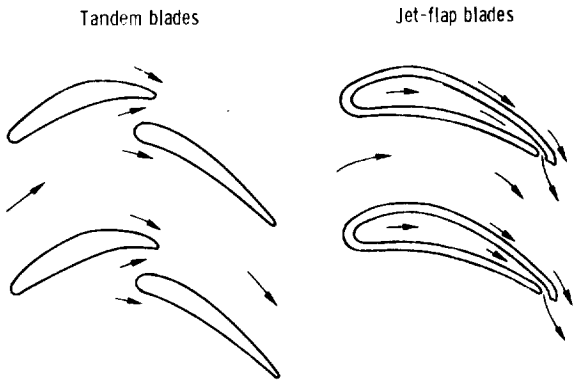

FIGURE 4-9. Low-solidity blading concepts.

takes place on the rear foil with a clean boundary layer and with perhaps 20 to 30 percent of the mainstream air going through the slot.

The jet-flap blade operates with a secondary air stream jetting out the trailing edge perpendicular to the main stream. This jet moves the rear stagnation point around the trailing edge, thereby substantially increasing the lift. In addition, the jet delivers some force to the blade through its own momentum. Figure 4-10 shows experimental velocity distributions

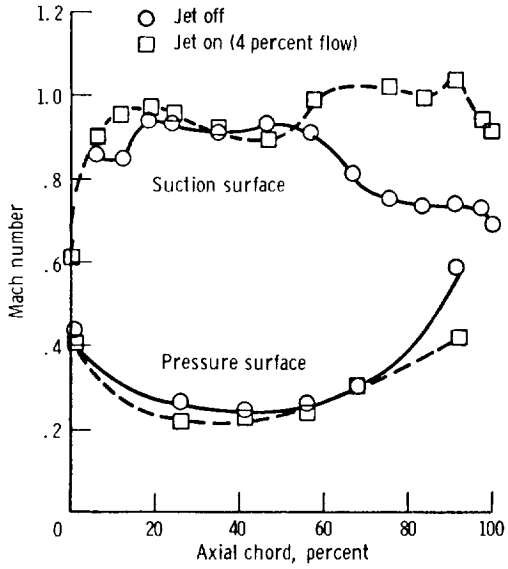

FIGURE 4-10. Jet-flap experimental velocity distributions.

around one such blade with the jet off and on. With the jet on, there is no longer a requirement for the velocities on the suction and pressure surfaces to be equal at the blade trailing edge. The loading diagram now approaches a rectangular shape, with the load coefficient ψ more closely approaching unity. Also, the diffusion on the suction surface is substantially reduced, thus suppressing the tendency to separate.

Both the jet-flap-blade and the tandem-blade concepts offer the potential for solidity reductions. The jet flap, however, will probably be considered only for applications where a secondary air flow is required for other purposes, such as blade cooling.

BLADE-PROFILE DESIGN

After the blade chord length has been selected and the blade spacing determined from solidity considerations, the blade itself must be designed. This involves determination of the inlet and exit geometries and the connecting surface profiles. The inlet and exit parts of the blade must be designed to provide a smooth, efficient transition between the blade channel and the free stream. The surface profiles connecting the inlet and exit must provide the required flow turning with minimum loss.

Exit

Consideration of the blade exit section includes the trailing edge, the throat, and the suction surface between the throat and the trailing edge.

Trailing edge.—In the design of turbines, it is wise to utilize the smallest trailing edge consistent with mechanical considerations. As shown in reference 17, an increase in trailing-edge thickness causes an increase in the blade loss. This effect is discussed further as part of the turbine-loss discussion in chapter 7. In addition, trailing-edge thickness also has a significant effect on the flow blockage in the blade exit region.

Consideration of the blockage effect will be made with the use of figure 4–11, which shows example blade sections with the nomenclature used. A new exit-velocity diagram is constructed at station $2a$, which is located just within the blade trailing-edge region. The reduced area due to the trailing-edge blockage results in a higher velocity at station $2a$ than at station 2, which is located just beyond the blade trailing-edge region. The equations that have been used to obtain this "within-the-blade" diagram at $2a$ include conservation of tangential momentum:

$$V_{u,2a} = V_{u,2} \tag{4–26}$$

and continuity:

$$(\rho V_x)_{2a}\left(1 - \frac{t}{s\cos\alpha_{2a}}\right) = (\rho V_x)_2 \tag{4–27}$$

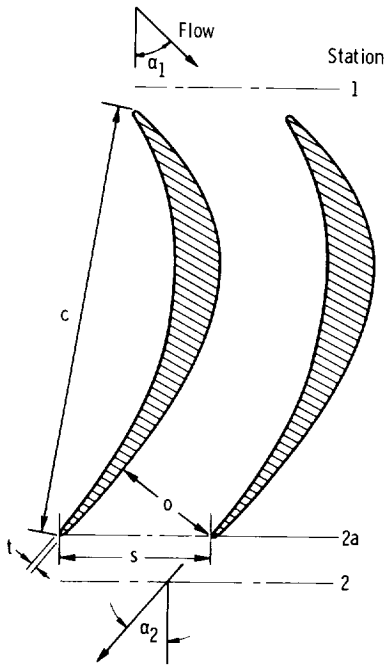

FIGURE 4–11. Blade section and nomenclature.

where t is the trailing-edge thickness, in meters or feet. The flow angle α_{2a} is determined from equations (4–26) and (4–27) by assuming the flow between stations $2a$ and 2 to be either incompressible (since the changes are usually small) or isentropic. The blade must be designed to have an exit angle of α_{2a} in order to produce a velocity-diagram angle α_2 at station 2 outside the blade row.

The Mach number at station $2a$ can also be determined from the preceding equations and assumptions. Because the angle α_2 is often large (65° or greater) and the flow Mach number at the blade exit (station 2) is often specified to be in the high subsonic region, the trailing-edge blockage can cause station $2a$ to become choked. It is, therefore, important to determine whether choking inside the blade row will occur such that the design flow rate cannot be obtained.

Throat.—Since, in general, a turbine blade row operates as a nozzle, with the flow accelerating up to the throat, or minimum area, the determination of the throat opening o (see fig. 4–11) becomes a rather critical aspect of the design procedure. One technique used successfully to give this dimension makes use of the "inside-the-trailing-edge" velocity diagram. If one assumes no change in flow conditions and a straight suction surface

between the throat and station $2a$, then the throat dimension can be obtained from the velocity diagram at station $2a$ by using the following equation:

$$\frac{o}{s} = \left(1 - \frac{t}{s \cos \alpha_{2a}}\right) \cos \alpha_{2a} \tag{4-28}$$

where o is the throat opening, in meters or feet.

If it is assumed that the velocity and loss do not change between the throat and the "free-stream" station 2, then

$$\frac{o}{s} = \cos \alpha_2 \tag{4-29}$$

When this method is used, the effect of trailing-edge thickness changes the angle of the throat position but not its length. Both methods (eqs. (4-28) and (4-29)) give similar throat dimensions. Reference 8 compares measured exit-flow angles with those predicted by equation (4-29). This comparison indicates close agreement at exit angles greater than 60° and deviations of up to 5° for exit angles down to 35°. This deviation could be due to lower solidities as well as larger gradients that would occur across the throat.

The throat-opening dimension as determined from equation (4-28) or (4-29) applies to the case where the blade-row exit flow is subsonic. If the flow within the blade row expands to a supersonic velocity, then this computed throat dimension must be modified to account for expansion from the sonic condition at the throat to the supersonic condition at the exit. For exit Mach numbers greater than about 1.3, the choking section (throat) must be located back within the channel such that a convergent-divergent passage is obtained. For low supersonic Mach numbers (up to, perhaps, 1.3), it has been found that satisfactory performance can be achieved if the throat is still located at the exit of the channel, and the additional flow expansion occurs downstream from the throat. In this case, the required channel exit dimension o would be computed by the following equation:

$$o = o_{ss}\left(\frac{A_{cr}}{A_{ss}}\right) \tag{4-30}$$

where

o_{ss} throat opening computed from equation (4-28) or (4-29) for supersonic velocity, m; ft

A_{cr} flow area for sonic flow, m^2; ft^2

A_{ss} flow area for supersonic flow, m^2; ft^2

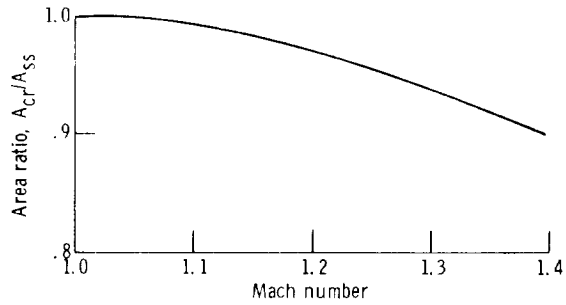

FIGURE 4-12. Variation in flow area with supersonic flow Mach number.

This area correction, with assumed isentropic flow between throat and exit, is shown in figure 4-12.

Suction surface downstream from throat.—The selection of the type of surface between the throat and trailing edge on the suction surface must be made from such considerations as structural integrity in the trailing-edge region, Mach number level and associated losses, desired level of suction-surface diffusion (D_s), and blade surface area resulting from the design.

A "straight back" design is used when low values of D_s (approximately unity) are specified and long trailing edges are permissible. High subsonic or transonic blading, as would be indicated by the discussion in the next paragraph, uses this type of surface in order to prevent flow acceleration on the tail of the blade and keep the associated losses low. Principal problems with a straight surface are that the low D_s values preclude low-solidity designs and the long trailing edge can become structurally flimsy.

Most conventional gas-turbine blading utilizes some amount of curvature between the throat and trailing-edge region. This permits some diffusion and additional loading on the tail of the blade, and it adds considerably to the structural integrity of the blade by introducing a wedge angle at the exit. If conventionally loaded blading is used, the effect of this curved surface on loss is not great. As indicated by figure 4-13 (which is from ref. 8), if the exit-flow Mach number is less than 0.8, the curvature effect is small. At higher exit Mach numbers (greater than 0.8), the effect on loss can become severe. Therefore, design curvatures should be lower in the higher Mach number regions. The type of curvature selected for the suction surface between the throat and trailing edge has an effect on the suction-surface velocity distribution. In general, the velocity distribution is improved if the curvature decreases from throat to trailing edge instead of remaining constant.

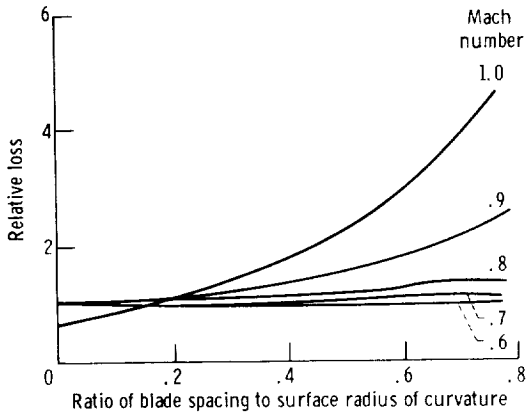

FIGURE 4-13. Variation of profile loss with Mach number and surface curvature between throat and exit (from ref. 8).

Inlet

The leading-edge geometry of a turbine blade row is usually less critical than the exit-region geometry. At the blade inlet, a relatively large leading-edge radius can usually be used, because the Mach number is generally low at the inlet and then increases through the blade row. The leading edge becomes a serious concern for low-reaction blading and high Mach number blading. In the case of low-reaction blading, excessively high velocities in the inlet region can lead to high values of suction-surface diffusion and a tendency toward increased losses. With high inlet Mach numbers, care must be taken that the area contraction is not so severe as to choke the blade at the inlet. Equations (4-26) and (4-27), which were used for the blade exit, can also be used to determine a blade-inlet opening and "within-the-blade" flow angle and Mach number to check for blade-inlet choking.

Although circular leading edges are usually specified, this is arbitrary and could limit the freedom of velocity-distribution selection in the leading-edge region. The large curvatures associated with circular leading edges can result in undesirable velocity peaks on both the suction- and pressure-surface portions of the leading edge. Other geometries, such as ellipses, which permit variations in curvature around the leading edge, can be used to minimize or eliminate the velocity peaks.

Blade-Surface Profile

Once the leading- and trailing-edge geometries have been selected, the task remaining is to join them with a profile that yields the required flow

turning and a satisfactory velocity distribution around the blade. The design procedure must describe the flow conditions through the blade rows to an accuracy sufficient to impose design controls (e.g., diffusion limits). Two of the major flow considerations are illustrated in figure 4–14. Velocity gradients occur across the channel from the suction to the pressure surface as a result of the static-pressure difference required to turn the flow. Radial variations in streamline position and, therefore, velocity occur as a result of radial-equilibrium considerations. Since both of these factors influence the blade-surface velocity distribution, the design procedures used should be at least of a quasi-three-dimensional nature. The channel flow analysis theory that serves as the basis for these design procedures and the computer programs available to perform the computations are discussed in the next chapter.

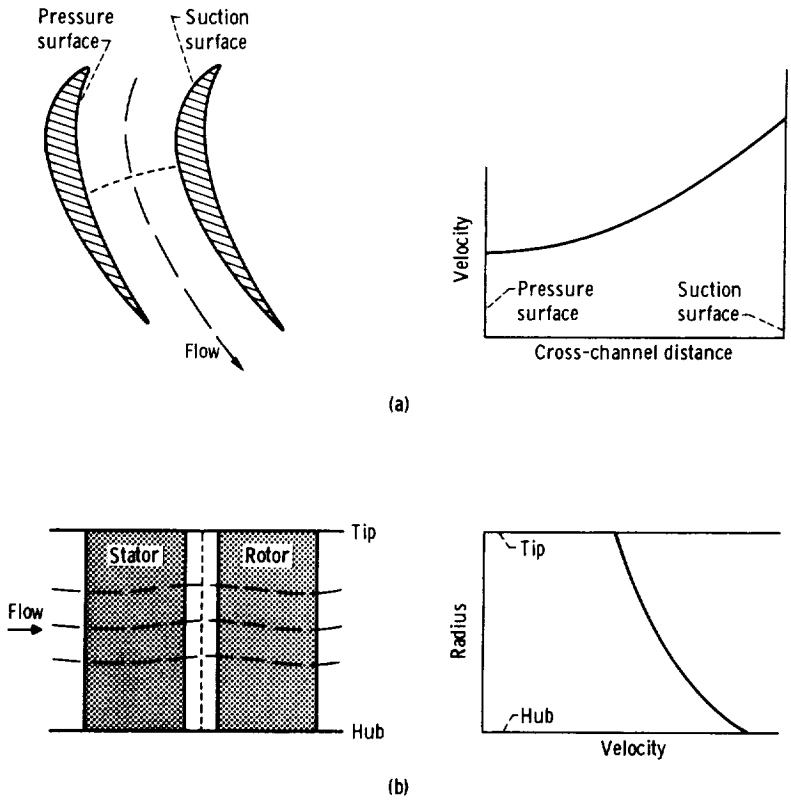

(a) Cross-channel variation.
(b) Radial variation.
FIGURE 4–14.—Turbine blade-row velocity variations.

REFERENCES

1. Zweifel, O.: The Spacing of Turbo-Machine Blading, Especially with Large Angular Deflection. Brown Boveri Rev., vol. 32, no. 12, Dec. 1945, pp. 436–444.
2. Lieblein, Seymour; Schwenk, Francis C.; and Broderick, Robert L.: Diffusion Factor for Estimating Losses and Limiting Blade Loadings in Axial-Flow-Compressor Blade Elements. NACA RM E53D01, 1953.
3. Stewart, Warner L.; Glassman, Arthur J.; and Vanco, Michael R.: Examination of Axial-Flow Turbine Blade-Loading Characteristics Using Diffusion Parameters. Paper 67–WA/GT–8, ASME, Nov. 1967.
4. Stewart, Warner L.; Whitney, Warren J.; and Miser, James W.: Use of Effective Momentum Thickness in Describing Turbine Rotor-Blade Losses. NACA RM E56B29, 1956.
5. Wong, Robert Y.; and Stewart, Warner L.: Correlation of Turbine-Blade-Element Losses Based on Wake Momentum Thickness with Diffusion Parameter for a Series of Subsonic Turbine Blades in Two-Dimensional Cascade and for Four Transonic Turbine Rotors. NACA RM E55B08, 1955.
6. Miser, James W.; Stewart, Warner L.; and Whitney, Warren J.: Analysis of Turbomachine Viscous Losses Affected by Changes in Blade Geometry. NACA RM E56F21, 1956.
7. Heller, Jack A.; Whitney, Rose L.; and Cavicchi, Richard H.: Experimental Investigation of a Conservatively Designed Turbine at Four Rotor-Blade Solidities. NACA RM E52C17, 1952.
8. Ainley, D. G.; and Mathieson, G. C. R.: An Examination of the Flow and Pressure Losses in Blade Rows of Axial-Flow Turbines. Rep. R&M 2891, Aeronautical Research Council, Gt. Britain, 1955.
9. Bettner, James L.; and Nosek, Stanley M.: Summary of Tests on Two Highly Loaded Turbine Blade Concepts in Three-Dimensional Cascade Sector. Paper 69–WA/GT–5, ASME, Nov. 1969.
10. Lueders, H. G.; and Roelke, R. J.: Some Experimental Results of Two Concepts Designed to Increase Turbine Blade Loading. J. Eng. Power, vol. 92, no. 2, Apr. 1970, pp. 198–206.
11. Stabe, Roy G.: Design and Two-Dimensional Cascade Test of Turbine Stator Blade with Ratio of Axial Chord to Spacing of 0.5. NASA TM X–1991, 1970.
12. Nosek, Stanley M.; and Kline, John F.: Two-Dimensional Cascade Investigation of a Turbine Tandem Blade Design. NASA TM X–1836, 1969.
13. Nosek, Stanley M.; and Kline, John F.: Two-Dimensional Cascade Test of a Jet-Flap Turbine Rotor Blade. NASA TM X–2183, 1971.
14. Stabe, Roy G.: Design and Two-Dimensional Cascade Test of a Jet-Flap Turbine Stator Blade with Ratio of Axial Chord to Spacing of 0.5. NASA TM X–2426, 1971.
15. Bettner, James L.: Design and Experimental Results of a Highly Loaded, Low Solidity Tandem Rotor. NASA CR–1803, 1971.
16. Bettner, James L.: Design and Experimental Results of a Highly Loaded, Low Solidity, Jet Flap Rotor. NASA CR–1968, 1972.
17. Prust, Herman W., Jr.; and Helon, Ronald M.: Effect of Trailing-Edge Geometry and Thickness on the Performance of Certain Turbine Stator Blading. NASA TN D–6637, 1972.

SYMBOLS

A	flow area, m^2; ft^2
c	chord, m; ft
D	diffusion parameter
F	force, N; lb
g	conversion constant, 1; 32.17 (lbm) (ft)/(lbf) (sec^2)
K	ratio of inlet to exit tangential components of velocity ($V_{u,1}/V_{u,2}$)
o	throat opening, m; ft
p	absolute pressure, N/m^2; lb/ft^2
R	reaction
s	blade spacing, m; ft
t	trailing-edge thickness, m; ft
V	absolute velocity, m/sec; ft/sec
x	axial distance, m; ft
α	fluid absolute angle from axial direction, deg
α_s	blade stagger angle from axial direction, deg
γ	ratio of specific heat at constant pressure to specific heat at constant volume
ρ	density, kg/m^3; lb/ft^3
σ	solidity
ψ	loading coefficient defined by equation (4–6)
ψ_s	loading coefficient defined by equation (4–5)

Subscripts:

cr	critical
inc	incompressible
max	maximum value
min	minimum value
opt	optimum
p	pressure surface
s	suction surface
ss	supersonic
u	tangential component
x	axial component
1	blade row inlet
2	blade row exit
2*a*	within trailing edge of blade row

Superscript:

	absolute total state

CHAPTER 5

Channel Flow Analysis

By Theodore Katsanis

The design of a proper blade profile, as indicated in the last section of chapter 4, requires calculation of the blade-row flow field in order to determine the velocities on the blade surfaces. This chapter presents the analysis theory for several methods used for this calculation and also discusses associated computer programs that were developed at NASA Lewis Research Center.

The actual velocity distribution throughout a blade-row flow field cannot be calculated at this time because of the extreme complexity of nonsteady, viscous, three-dimensional flow through geometrically complex passages. To calculate a theoretical velocity distribution, therefore, certain simplifying assumptions must be made. The three-dimensional flow is simplified to flow on or through various two-dimensional surfaces. Such surfaces are illustrated in figure 5–1 for the case of a radial-inflow turbine. Similar surfaces are used for an axial-flow turbine. A flow solution on the mean hub-to-shroud stream surface (commonly called the meridional surface), shown in figure 5–1(a), does not yield blade-surface velocities directly, but provides information required for the blade-to-blade surface (fig. 5–1(b)) and orthogonal surface (fig. 5–1(c)) solutions, which yield the desired blade-surface velocities.

There are two parts to a method of analysis to obtain a velocity distribution over one of these surfaces. The first part is the mathematical formulation of the problem, and the second part is the numerical solution of the mathematical problem. For the mathematical formulation of the problem, we will discuss stream- and potential-function methods and velocity-gradient (stream-filament) methods. The stream- and potential-

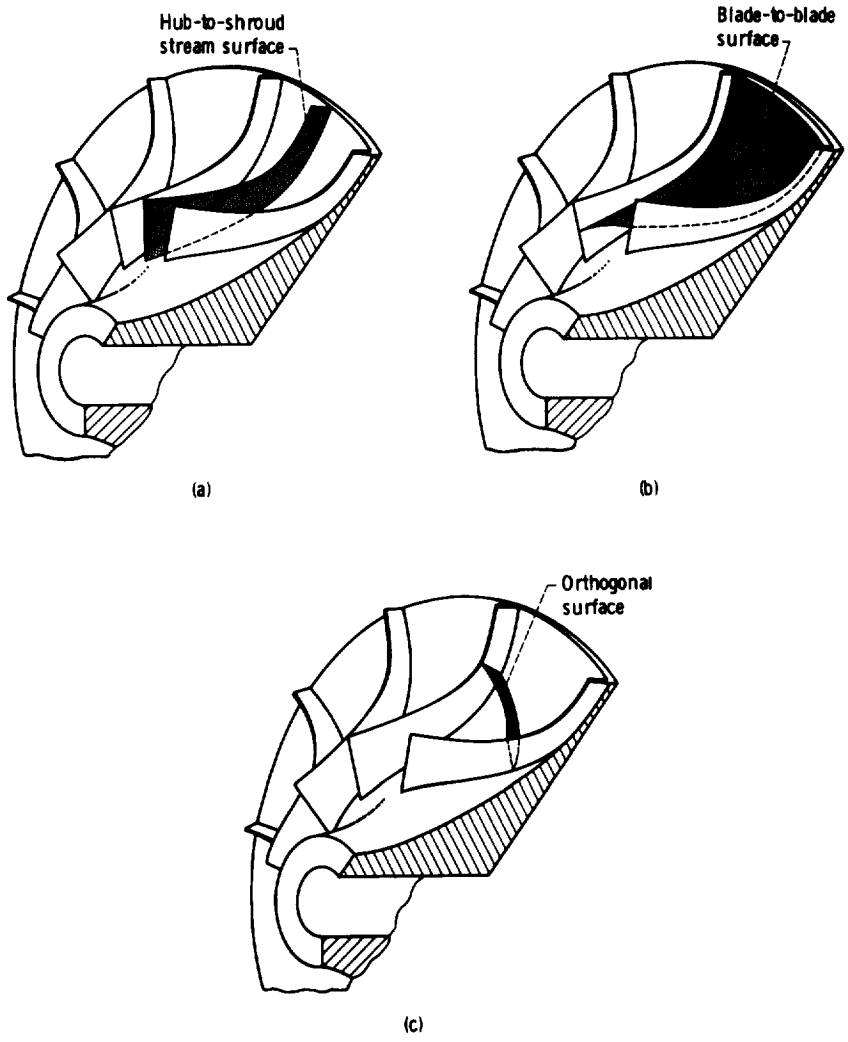

(a) Hub-to-shroud stream surface. (b) Blade-to-blade surface.
(c) Orthogonal surface across flow passage.
FIGURE 5–1.—Surfaces used for velocity-distribution calculations.

function methods will be described relative to the blade-to-blade surface solution. A similar type of analysis can be made for the meridional surface. The velocity-gradient equation to be presented is general and can be used for solutions on any of the surfaces.

The following assumptions are made in deriving the various methods of analysis discussed herein:

(1) The flow is steady relative to the blade. This means that the surface velocity at any given point on the blade does not vary with time. Thus, if the blade is rotating, the flow would not be steady relative to a fixed coordinate system.

(2) The fluid obeys the ideal-gas law

$$p = \rho RT \tag{5-1}$$

where

p absolute pressure, N/m^2; lb/ft^2
ρ density, kg/m^3; lb/ft^3
R gas constant, J/(kg)(K); (ft)(lbf)/(lbm)(°R)
T absolute temperature, K; °R

or is incompressible (ρ = constant).

(3) The fluid is nonviscous. A nonviscous fluid has no boundary layer. The blade-surface velocity is calculated, therefore, as if the free stream extends to the blade surface.

(4) The fluid has a constant heat capacity.

(5) The flow is isentropic.

(6) The total temperature and total pressure are uniform across the inlet.

(7) For the stream- and potential-function analyses, the additional assumption is made that the flow is absolutely irrotational. Therefore,

$$\text{curl } \mathbf{V} = \nabla \times \mathbf{V} = \mathbf{0} \tag{5-2}$$

where $\mathbf{V}$ is the absolute velocity vector. Intuitively, this means that particles do not change their *absolute* orientation with time, although their shape may change. For example, figure 5–2 shows a hypothetical particle at times t and $t+\Delta t$. In the absolute frame of reference, the particle changes its location and shape at a later instant of time, but the net rotation is zero. Of course, in a frame of reference relative to the blade, the particle has rotated, because the frame of reference has rotated.

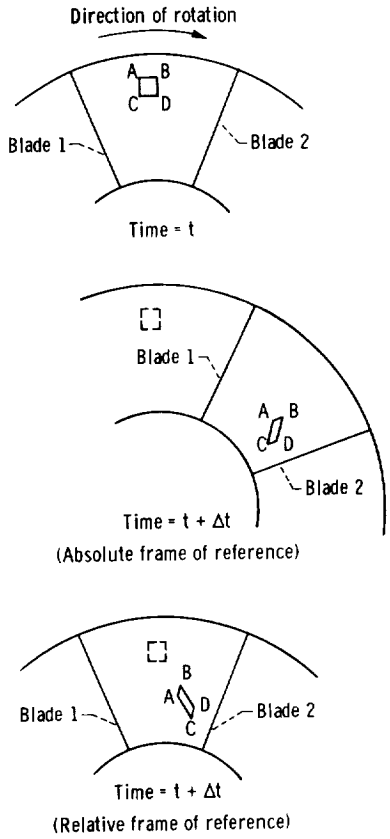

FIGURE 5–2.—Absolutely irrotational flow.

Some numerical techniques for solving the mathematical equations will also be discussed. However, it must be emphasized that there are many techniques for solving these equations, and we will discuss only a few. An excellent theoretical discussion of flow in two-dimensional cascades is given in Chapter IV of reference 1.

STREAM- AND POTENTIAL-FUNCTION ANALYSES

Stream-Function Method

The stream function can be defined several ways, but perhaps the simplest is in terms of streamlines. Suppose we consider two blades of a cascade as shown in figure 5–3. It is assumed that there is two-dimensional

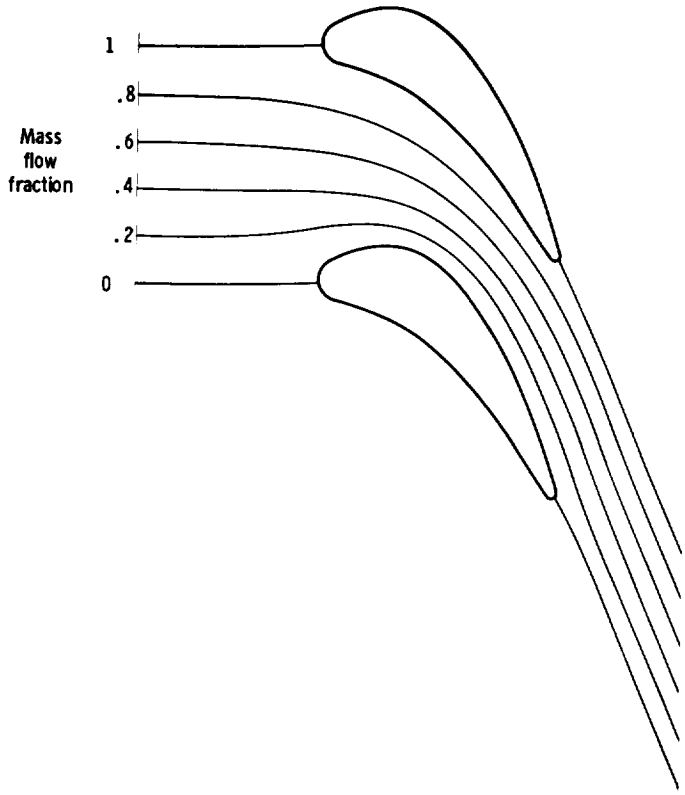

FIGURE 5–3.—Streamlines for a stator cascade.

axial flow here, so that the radius r from the centerline is constant and there is no variation of the flow in the radial direction. There may be rotation about the centerline.

Shown in figure 5–3 are a number of streamlines. The mass flow between the blades is w. The number by each streamline indicates the fraction of w passing between the upper surface of the lower blade and the given streamline. Thus, the upper surface (which is a streamline) has the value 0, and the lower surface of the upper blade has the value of 1, while the remaining streamlines have values between 0 and 1. Note that a value can be associated with any point in the passage. This value is called the stream-function value and can be used to define the stream function.

It will be recalled that mass flow can be calculated for a one-dimensional (or uniform) flow by

$$w = \rho V A \tag{5–3}$$

where

w rate of mass flow, kg/sec; lb/sec
V fluid absolute velocity, m/sec; ft/sec
A flow area normal to the direction of the velocity V, m^2; ft^2

This can be extended to a varying flow by using an integral expression:

$$w = \int_A \rho V \, dA \tag{5-4}$$

Since this stream-function analysis applies to both stationary and rotating cascades (blade rows), the fluid velocity will be expressed in terms of relative velocity W, which for a stationary blade row reduces to absolute velocity V. We will assume that our cascade has a uniform height b. Then, the mass flow $w_{1,2}$ between any two points Q_1 and Q_2 in the passage (see fig. 5–4) can be calculated by

$$w_{1,2} = \int_{Q_1}^{Q_2} \rho W_n b \, dq \tag{5-5}$$

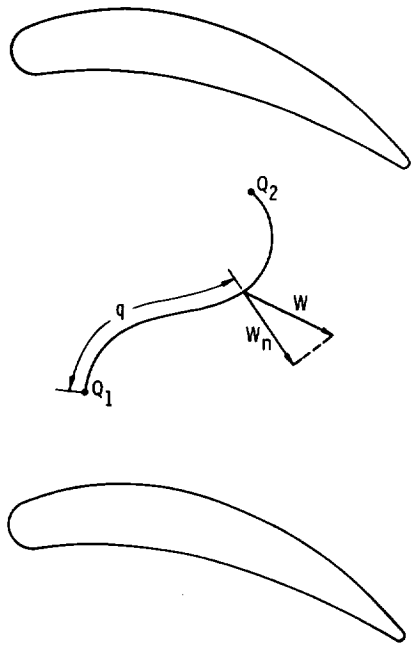

FIGURE 5–4.—Arbitrary curve joining two points in flow passage.

where W_n is the relative velocity component in the direction of the right-hand normal of the line going from Q_1 to Q_2. This sign convention means that $w_{1,2}$ will be negative if Q_2 is below a streamline passing through Q_1. The integral is a line integral between the points Q_1 and Q_2 and is independent of path for steady flow relative to the cascade.

With the use of equation (5–5), an analytical expression can be written for the stream function u at a point (x, y):

$$u(x, y) = \frac{\int_{Q_0}^{(x,y)} \rho W_n b \, dq}{w} \tag{5–6}$$

where Q_0 is any point on the upper surface of the lower blade, and the integral is taken along any curve between Q_0 and (x, y). This is indicated in figure 5–5.

Since the integral in equation (5–6) is independent of path, it is relatively easy to calculate the partial derivatives of u. For example, we will calculate $\partial u/\partial x$ at the point (x, y). Let $x_0 < x$ such that the point (x_0, y) is still in the flow passage, as shown in figure 5–6. Then

$$u(x, y) = \frac{\int_{C_1} \rho W_n b \, dq + \int_{C_2} \rho W_n b \, dq}{w} \tag{5–7}$$

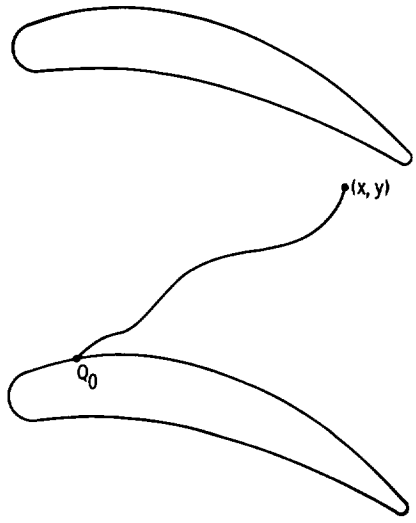

FIGURE 5–5.—Curve joining (x,y) with a point on the upper surface of the lower blade.

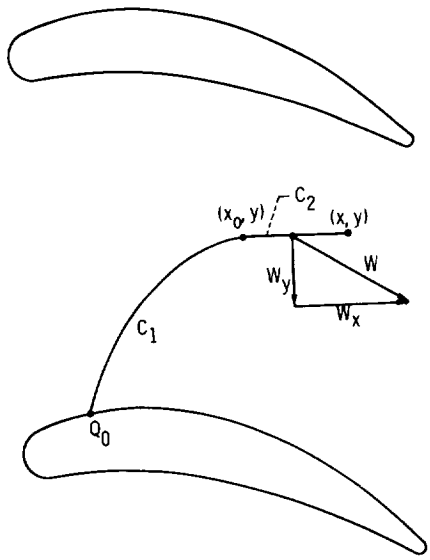

FIGURE 5–6.—Curve joining horizontal line through (x,y) with a point on the upper surface of the lower blade.

where C_1 is an arbitrary curve between Q_0 and (x_0, y), and C_2 is a horizontal line between (x_0, y) and (x, y). The integral along C_1 does not depend on x. Along C_2, we have $W_n = -W_y$ and $dq = dx$. Hence,

$$\frac{\partial u}{\partial x}(x, y) = -\frac{\partial}{\partial x}\int_{x_0}^{x} \frac{\rho W_y b\, dx}{w} \tag{5–8}$$

or

$$\frac{\partial u}{\partial x} = -\frac{\rho W_y b}{w} \tag{5–9}$$

In a similar manner, we can calculate

$$\frac{\partial u}{\partial y} = \frac{\rho W_x b}{w} \tag{5–10}$$

Now we will make use of the fact that the flow is absolutely irrotational. From the definition of the curl operator and the above assumption,

$$\text{curl } \mathbf{V} = \left(\frac{\partial V_z}{\partial y} - \frac{\partial V_y}{\partial z}\right)\mathbf{i} + \left(\frac{\partial V_x}{\partial z} - \frac{\partial V_z}{\partial x}\right)\mathbf{j} + \left(\frac{\partial V_y}{\partial x} - \frac{\partial V_x}{\partial y}\right)\mathbf{k} = \mathbf{0} \tag{5–11}$$

where $\mathbf{i}$, $\mathbf{j}$, and $\mathbf{k}$ are the unit vectors in the x, y, and z directions, respec-

tively, and V_x, V_y, and V_z are the absolute velocity components (in m/sec or ft/sec) in the x, y, and z directions, respectively. Since we are considering two-dimensional flow only,

$$V_z = 0 \tag{5–12}$$

and

$$\frac{\partial V_x}{\partial z} = \frac{\partial V_y}{\partial z} = 0 \tag{5–13}$$

Hence, equation (5–11) requires only that

$$\frac{\partial V_y}{\partial x} = \frac{\partial V_x}{\partial y} \tag{5–14}$$

Since

$$V_x = W_x \tag{5–15}$$

and

$$V_y = W_y + \omega r \tag{5–16}$$

where ω is the angular speed (in rad/sec) and the radius r is constant, equation (5–14) can be expressed in terms of relative velocities as

$$\frac{\partial W_y}{\partial x} = \frac{\partial W_x}{\partial y} \tag{5–17}$$

Actually, the flow is irrotational with respect to the moving coordinates in this particular case. Now, from equations (5–10) and (5–9),

$$W_x = \frac{w}{\rho b} \frac{\partial u}{\partial y} \tag{5–18}$$

$$W_y = -\frac{w}{\rho b} \frac{\partial u}{\partial x} \tag{5–19}$$

Substituting equations (5–18) and (5–19) into equation (5–17) yields

$$\frac{\partial}{\partial x}\left(\frac{1}{\rho}\frac{\partial u}{\partial x}\right) + \frac{\partial}{\partial y}\left(\frac{1}{\rho}\frac{\partial u}{\partial y}\right) = 0 \tag{5–20}$$

since w and b are both constant.

For incompressible flow, ρ is constant, and

$$\nabla^2 u = \frac{\partial^2 u}{\partial x^2} + \frac{\partial^2 u}{\partial y^2} = 0 \tag{5–21}$$

which is Laplace's equation. Any function satisfying Laplace's equation is called a harmonic function. There is a great deal of theory concerning

harmonic functions that is related to the theory of analytic functions of complex variables.

The important thing to know here is that there are a tremendous number of functions that satisfy equation (5–21), and we must find a solution that satisfies certain boundary conditions. The solution to either Laplace's equation (5–21) or equation (5–20) will be determined by specifying two things: (1) a finite region, and (2) a boundary condition along the entire boundary of the region.

The first thing that must be specified is the solution region. A typical two-dimensional cascade is shown in figure 5–7. Since the flow is the same in every passage, we can consider a finite solution region as shown in figure 5–8. It is assumed that AH is sufficiently far upstream so that the flow is uniform along this part of the boundary and that the flow angle β_{in} is known. Similarly, it is assumed that the flow is uniform along DE, and that the flow angle β_{out} is known. From the way the stream function was defined, we can specify boundary conditions on the entire boundary ABCDEFGHA. Along BC, $u=0$; and along FG, $u=1$. Along AB, HG, CD, and FE, a periodic condition exists; that is, the value of u along HG and FE is exactly 1 greater than it is along AB and CD. Along AH and DE, $\partial u/\partial \eta$ is known, where η is the distance in the direction of the outer normal.

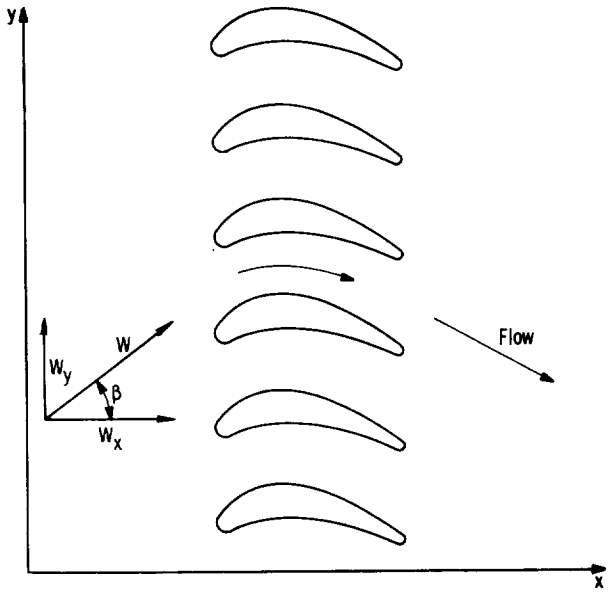

FIGURE 5–7.—Two-dimensional infinite cascade.

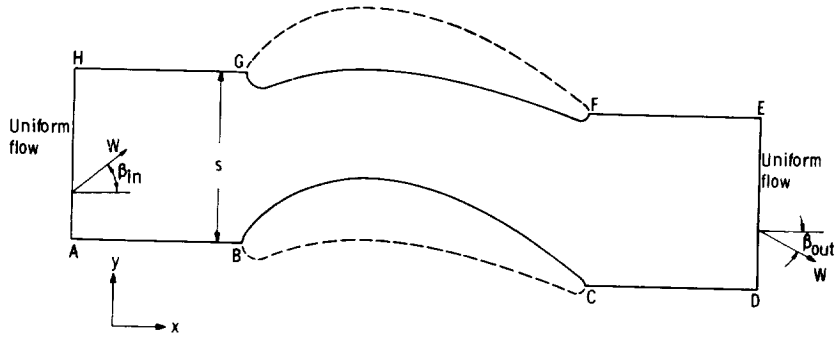

FIGURE 5–8.—Finite solution region.

Consider the differential of u in the direction of the velocity W:

$$du=\frac{\partial u}{\partial x}\,dx+\frac{\partial u}{\partial y}\,dy=0 \tag{5–22}$$

The differential is 0 because the stream function is constant along a streamline, and the velocity vector must be tangent to a streamline. Along AH,

$$\frac{\partial u}{\partial \eta}=-\frac{\partial u}{\partial x} \tag{5–23}$$

and substitution from equation (5–22) yields

$$\frac{\partial u}{\partial \eta}=\frac{\partial u}{\partial y}\frac{dy}{dx} \tag{5–24}$$

However,

$$\frac{dy}{dx}=\tan\beta \tag{5–25}$$

Further, $\partial u/\partial y$ is constant along AH, since it is assumed that the flow is uniform there. Therefore,

$$\frac{\partial u}{\partial y}=\frac{[u(\mathrm{H})-u(\mathrm{A})]}{s}=\frac{1}{s} \tag{5–26}$$

where s is the blade spacing in the y direction. Substituting equations (5–25) and (5–26) in equation (5–24) gives along AH

$$\left(\frac{\partial u}{\partial \eta}\right)_{in}=\frac{\tan\beta_{in}}{s} \tag{5–27}$$

Similarly, along DE, one can calculate

$$\left(\frac{\partial u}{\partial \eta}\right)_{out} = -\frac{\tan \beta_{out}}{s} \tag{5–28}$$

We now have a boundary condition along the entire boundary of the region shown in figure 5–8. These boundary conditions will always determine a unique solution to Laplace's equation (5–21). For compressible flow (eq. (5–20)), a unique solution is always determined if the flow is strictly subsonic throughout the region.

There are numerous techniques for solving equation (5–20) or (5–21). After the stream function is obtained, blade-surface velocities and velocities throughout the passage can be obtained by differentiation of the stream function. This is what is known as the direct problem. A method of solving this problem will be discussed later. The indirect, or inverse, problem is to specify a desired velocity distribution on the blade surface and from this determine a blade shape that will give this velocity distribution. This will not be discussed here.

Potential-Function Method

For two-dimensional irrotational flow, a potential function can be defined. If lines of equal potential are drawn, they will be orthogonal to streamlines. The potential function will not be defined in the same detail as the stream function, but the main properties and relations will be given. If the potential function Φ exists (i.e., the flow is irrotational), then it can be defined so that

$$\frac{\partial \Phi}{\partial x} = V_x \tag{5–29}$$

and

$$\frac{\partial \Phi}{\partial y} = V_y \tag{5–30}$$

We will refer to absolute velocities here, since we must have flow irrotational relative to the coordinate system used. This, coupled with the assumption of absolute irrotational flow, implies that the coordinate system does not rotate. This does not exclude use of the potential function for pure axial flow, since the rotation has no effect if there is no change in radius; that is, the flow is actually irrotational with respect to the blades, as we saw in the discussion of the stream function.

From the continuity relationship for steady flow,

$$\frac{\partial(\rho V_x)}{\partial x} + \frac{\partial(\rho V_y)}{\partial y} = 0 \tag{5–31}$$

Substituting equations (5–29) and (5–30) in equation (5–31) yields

$$\frac{\partial}{\partial x}\left(\rho\frac{\partial\Phi}{\partial x}\right)+\frac{\partial}{\partial y}\left(\rho\frac{\partial\Phi}{\partial y}\right)=0 \tag{5–32}$$

If the flow is incompressible, ρ is constant, and

$$\nabla^2\Phi=\frac{\partial^2\Phi}{\partial x^2}+\frac{\partial^2\Phi}{\partial y^2}=0 \tag{5–33}$$

So, the potential function satisfies Laplace's equation. Thus, for incompressible, irrotational flow, both the stream function and the potential function satisfy the same differential equation (Laplace's equation). The difference lies in the boundary conditions.

We can consider the same solution region shown in figure 5–8. We can specify boundary conditions over the entire boundary as follows: Along BC and FG,

$$\frac{\partial\Phi}{\partial\eta}=V_n=0 \tag{5–34}$$

where V_n is the velocity normal to the blade surface. Along AH,

$$\left(\frac{\partial\Phi}{\partial\eta}\right)_{in}=-(V_x)_{in} \tag{5–35}$$

and along DE,

$$\left(\frac{\partial\Phi}{\partial\eta}\right)_{out}=(V_x)_{out} \tag{5–36}$$

The inlet and outlet axial velocities are given by the equations

$$(V_x)_{in}=\frac{w}{\rho_{in}bs} \tag{5–37}$$

and

$$(V_x)_{out}=\frac{w}{\rho_{out}bs} \tag{5–38}$$

Along AB, GH, CD, and EF, a periodic condition exists. Since the flow is uniform along AH,

$$\left(\frac{\partial\Phi}{\partial y}\right)_{in}=\frac{[\Phi(\mathrm{H})-\Phi(\mathrm{A})]}{s}=(V_y)_{in} \tag{5–39}$$

Substituting

$$V_y=V_x\tan\beta \tag{5–40}$$

into equation (5–39) yields

$$\Phi(\mathrm{H}) = \Phi(\mathrm{A}) + s(V_x)_{in} \tan \beta_{in} \tag{5–41}$$

Because of the periodicity, Φ is exactly $s(V_x)_{in} \tan \beta_{in}$ greater along HG than along AB. Similarly, at the outlet,

$$\Phi(\mathrm{E}) = \Phi(\mathrm{D}) + s(V_x)_{out} \tan \beta_{out} \tag{5–42}$$

Equation (5–42) gives the difference in Φ along the lines FE and CD.

This completes the boundary conditions for equation (5–32) or (5–33). The boundary conditions, however, do not determine a unique solution, but only a solution within an arbitrary additive constant. If the value of Φ is specified at one point, these boundary conditions will determine a unique solution to equation (5–33) for incompressible flow, or to equation (5–32), for strictly subsonic compressible flow throughout the region.

As for the stream function, there are numerous methods for solving equation (5–32) or (5–33) subject to the preceding or equivalent boundary conditions. A method for solving the inverse problem of specifying the velocity distribution to determine the blade shape is described in references 2 and 3.

Choice of Stream- or Potential-Function Method

If the flow is steady, irrotational, and incompressible, there is little to choose between the stream function and the potential function. In this case, the choice is made on the basis of ease of solution for the boundary conditions (the differential equation is the same: Laplace's equation). However, if any of the three assumptions (steady, irrotational, or incompressible flow) is not applicable, then we may be restricted as to the choice of stream function or potential function.

The existence of the stream function is proven from the continuity equation. For the stream function to be defined, the mass flow crossing a line between two points must be independent of path. This requires that the flow be either incompressible or steady. Some additional assumption is necessary for the flow to be unique. We used the assumption that the flow was absolutely irrotational, which turned out to be irrotational relative to the blade for the axial-flow case considered. However, other assumptions could be made for other problems. Another restriction on the stream function is that it can be defined only for two-dimensional flow. This can easily be seen since the stream function is defined as a percentage of mass flow between two points, and this is meaningless in three dimensions.

The existence of the potential function can be shown if the flow is irrotational relative to the given coordinate system. This is necessary

because we must have equality of mixed second partial derivatives; that is, if

$$\frac{\partial^2 \Phi}{\partial x \partial y} = \frac{\partial^2 \Phi}{\partial y \partial x} \tag{5–43}$$

then

$$\frac{\partial}{\partial x} V_y = \frac{\partial}{\partial y} V_x \tag{5–44}$$

and the flow must be irrotational. A similar situation exists in three-dimensional flow; that is, the potential function exists only if the flow is irrotational with respect to the coordinate system being used. Finally, an assumption must be made to assure a unique solution. This can be done by using the continuity equation.

Finite-Difference Solution for Stream-Function Method

As stated before, there are many ways of solving various problems posed by stream-function or potential-function theory. We will consider in further detail the finite-difference solution of the direct problem for the stream function for the simplest case of steady, incompressible, irrotational flow. In this case, we must solve Laplace's equation subject to the boundary conditions discussed in the section on the stream function. The method of solution for the potential function is quite similar, but with a lower rate of convergence for the finite difference solution.

The first step is to establish a rectangular grid of mesh points in the region shown in figure 5–8. A typical grid is shown in figure 5–9. Then a finite-difference approximation to Laplace's equation (eq. (5–21)) can be written at each mesh point where the stream function is unknown. A typical mesh point with four neighboring mesh points is shown in figure 5–10. The point in consideration is labeled 0, and the four neighboring points are labeled 1 to 4, as shown. The distance between points 1 and 0 is denoted h_1, and similarly, the other distances are h_2, h_3, and h_4 as indicated in figure 5–10. The value of u at points 0 to 4 are labeled u_0 to u_4, respectively. With the use of a Taylor series expansion for u in the x- and y-directions, equation (5–21) can be approximated by using only values of u at mesh points. (Further explanation of this is given in ch. 6 of ref. 4.) When this is done, the following expression is obtained:

$$\left[\frac{2u_1}{h_1(h_1+h_2)} + \frac{2u_2}{h_2(h_1+h_2)} - \frac{2u_0}{h_1 h_2}\right] + \left[\frac{2u_3}{h_3(h_3+h_4)} + \frac{2u_4}{h_4(h_3+h_4)} - \frac{2u_0}{h_3 h_4}\right] = 0 \tag{5–45}$$

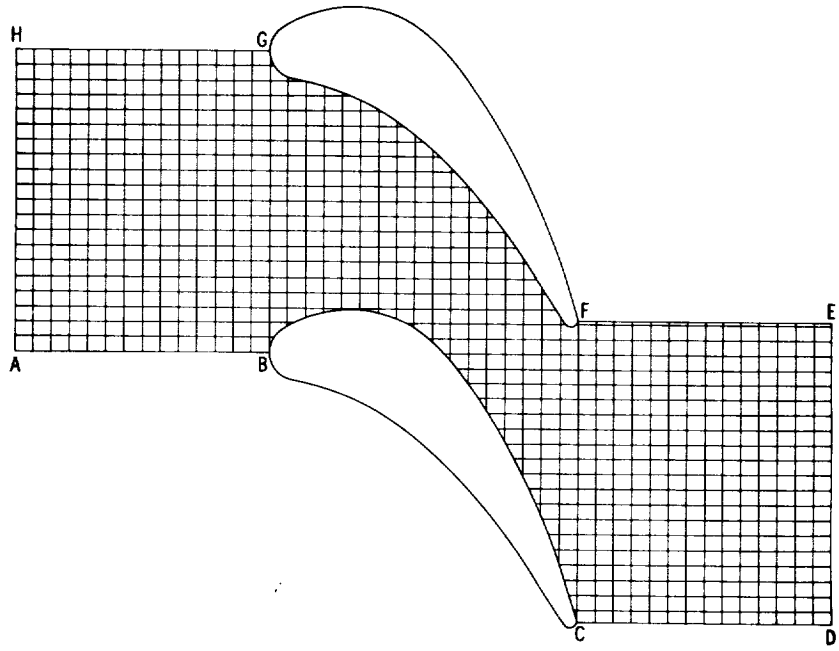

FIGURE 5–9.—Mesh used for a finite-difference solution.

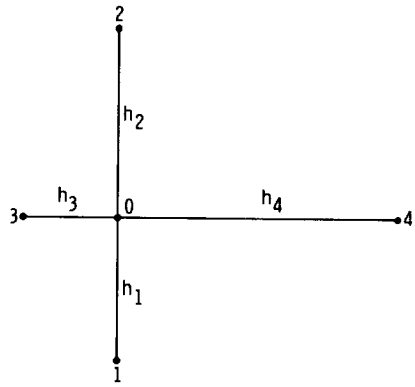

FIGURE 5–10.—Notation for adjacent mesh points and mesh spaces.

Solving equation (5–45) for u_0 yields the expression

$$u_0 = \sum_{i=1}^{4} a_i u_i \tag{5–46}$$

where

$$a_1 = \frac{h_3 + h_4}{a_0 h_1} \tag{5–47}$$

$$a_2 = \frac{h_3 + h_4}{a_0 h_2} \tag{5–48}$$

$$a_3 = \frac{h_1 + h_2}{a_0 h_3} \tag{5–49}$$

$$a_4 = \frac{h_1 + h_2}{a_0 h_4} \tag{5–50}$$

$$a_0 = (h_3 + h_4)\left(\frac{1}{h_1} + \frac{1}{h_2}\right) + (h_1 + h_2)\left(\frac{1}{h_3} + \frac{1}{h_4}\right) \tag{5–51}$$

Equation (5–46) holds at every interior mesh point. If one of the neighboring points is on a blade surface, then the value of u at that point can be used. At other points along the boundary, equation (5–46) cannot be used, but the boundary conditions can be used to obtain alternate equations at these points. For example, along the upstream boundary AH in figure 5–9, $\partial u/\partial \eta$ is given by equation (5–27). If point 0 is on line AH, then, a finite difference approximation gives

$$u_0 = u_4 + h_4\left(\frac{\tan \beta_{in}}{s}\right) \tag{5–52}$$

Similarly, if point 0 is on line DE,

$$u_0 = u_3 - h_3\left(\frac{\tan \beta_{out}}{s}\right) \tag{5–53}$$

For the points along AB and CD, equations can be derived by using the periodic boundary condition. If the point 0 (fig. 5–11) is on the boundary between A and B, the point 1 is outside the boundary. However, it is known that $u_1 = u_{1,s} - 1$, where the point 1,s is a distance s above point 1 in the y-direction, as shown in figure 5–11. Substituting this

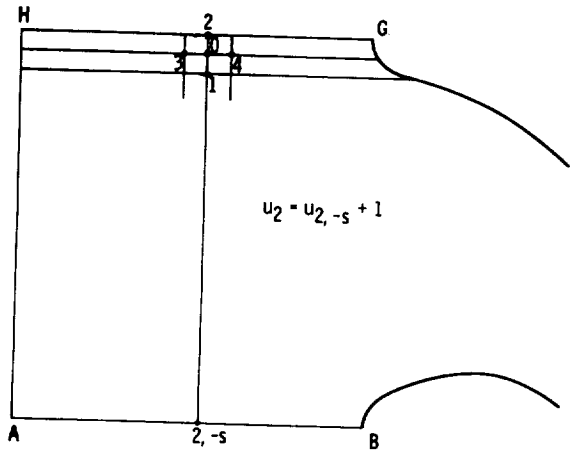

FIGURE 5–11.—Mesh point on line AB.

condition in equation (5–46) gives

$$u_0 = a_1 u_{1,s} + \sum_{i=2}^{4} a_i u_i - a_1 \tag{5–54}$$

This equation holds along CD (fig. 5–8) also.

The points along HG need not be considered, since they are just 1 greater than the corresponding point along AB. The equation for the first mesh line below HG, therefore, must be modified, since point 2 is on line HG. In this case, $u_2 = u_{2,-s} + 1$, where the point $2,-s$ is a distance s below point 2 in the negative y-direction, as indicated in figure 5–12. Substituting this condition in equation (5–46) gives

$$u_0 = a_1 u_1 + a_2 u_{2,-s} + a_3 u_3 + a_4 u_4 + a_2 \tag{5–55}$$

This equation also applies to the first mesh line below FE (fig. 5–8).

One of equations (5–46) or (5–52) to (5–55) can be applied to each mesh point for which the stream function is unknown in the region of interest to give the same number of linear equations as there are unknowns. These points where the stream function is unknown will be referred to simply as unknown mesh points.

Suppose that there are n unknown mesh points. We then have n equations in n unknowns. The points can be numbered consecutively from 1 to n. The values of u will then be u_1 at the first point, u_2 at the second point, and so forth up to u_n at the last point. At each point, one equation will apply. The equation at a typical point, i, could be written

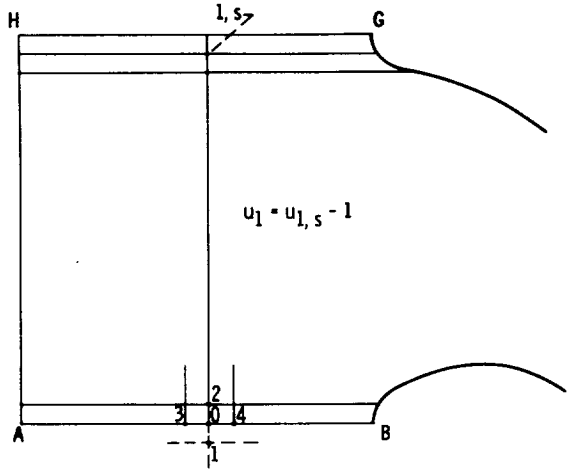

FIGURE 5–12.—Mesh point on first line below HG.

$$\sum_{j=1}^{n} a_{ij}u_j = k_i \tag{5–56}$$

The values of the a_{ij} are determined by one of equations (5–47) through (5–55). All but five, at most, of the a_{ij} are zero, and the $a_{ii} = -1$. The value of k_i is always zero, except for the outermost unknown points around the boundary. It can be shown that the a_{ij} matrix is always nonsingular; hence there is always a unique solution for the u_j.

A numerical solution to equation (5–56) can be obtained by iterative techniques. These techniques are particularly valuable in solving systems of linear equations of this type; that is, where there are a large number of unknowns, but few terms in each equation. Storage requirements are small, and roundoff error is minimized with iterative methods. To start the iteration, an initial estimate of u at every unknown mesh point is required. The simplest iterative procedure is relaxation. This consists of changing the estimated value of u at each point in succession so as to satisfy the equation for that point. After this is done at every point, the procedure is repeated until there is negligible change in the values of u. The procedure is simple and it always converges for this problem. However, the convergence rate is extremely slow, so that excessive computer time is required. The convergence can be accelerated greatly by increasing the change in u at each iteration by a factor ω, called the overrelaxation factor. When $\omega = 1$, the procedure is straight relaxation, and when $\omega > 1$, it is overrelaxation. It is proven in reference 4 that overrelaxation (or underrelaxation) is convergent if $0 < \omega < 2$. However, the greatest rate of convergence occurs when $1 < \omega < 2$. In fact, there is an optimum value of ω

between 1 and 2 which gives the most rapid convergence. This optimum overrelaxation factor can be calculated as explained in reference 4.

To give an explicit expression for the overrelaxation procedure, we will use a superscript on the u_i. That is, u_i^m is the m^{th} iterate of u_i. The initial estimates are denoted u_i^0 and may be any value. For example, an initial estimate of $u_i^0 = 0$ is satisfactory. Then, if u_i^m is known for all i, we can calculate u_i^{m+1}, for $i = 1, 2, \ldots, n$ in succession by

$$u_i^{m+1} = u_i^m + \omega \left\{ -\sum_{j=1}^{i-1} a_{ij} u_j^{m+1} - \sum_{j=i+1}^{n} a_{ij} u_j^m + k_i - u_i^m \right\} \quad (5\text{–}57)$$

After a solution for u is obtained by overrelaxation (or any other method), it is necessary to calculate the velocities with the use of equations (5–9) and (5–10) as

$$W_x = \frac{w\left(\frac{\partial u}{\partial y}\right)}{\rho b} \quad (5\text{–}58)$$

and

$$W_y = -\frac{w\left(\frac{\partial u}{\partial x}\right)}{\rho b} \quad (5\text{–}59)$$

The partial derivatives $\partial u/\partial x$ and $\partial u/\partial y$ must be estimated from the calculated discrete values of u_i. This can be readily done, either by finite differences, or by fitting a smooth curve, such as a spline curve, through the points. The resultant velocity is calculated from the two components at unknown mesh points. On the blade surface, the velocity is calculated from one component and the blade tangent angle.

Computer Programs for Stream-Function Analyses

As can be seen, the solution of Laplace's equation and the calculation of velocities is a lengthy calculation procedure which is best done by computer. Several computer programs have been written at the NASA Lewis Research Center for the analysis of flow through turbomachine blading by stream-function methods. Most of these programs are for blade-to-blade analysis (region shown in fig. 5–9). The program called TURBLE, which is described in reference 5, can be used to analyze axial, radial, or mixed flow. In accordance with the constraints associated with the stream-function method, the flow must be subsonic throughout the entire solution region. The TSONIC program, described in reference 6, super-

sedes TURBLE in that it performs all the same calculations and, in addition, extends the solution to transonic (local supersonic velocities) flow problems. Transonic solutions are obtained by using a velocity-gradient equation of the type described in the next section to extend a preliminary (lower mass flow rate) subsonic stream-function solution. A program called TANDEM, which is described in reference 7, can be used to analyze flow in tandem or slotted blade rows or blade rows with splitters. Another program, called MAGNFY and described in reference 8, obtains a detailed solution in the leading- or trailing-edge regions of any blade or in the slot region of tandem or slotted blades. The TANDEM and MAGNFY programs are restricted to subsonic flow.

Flow in the meridional plane (mean hub-to-shroud flow surface, as indicated by fig. 4–14(b) or fig. 5–1(a)), of any axial- or mixed-flow turbomachine can be analyzed by a program called MERIDL, which is described in references 9 and 10. Transonic solutions can be obtained by the use of a velocity-gradient equation to extend a preliminary subsonic stream-function solution.

VELOCITY-GRADIENT ANALYSIS

As indicated previously, the stream-function and potential-function methods of analysis are limited to solutions that are entirely subsonic within the computation region. By use of a velocity-gradient equation and additional assumptions, however, the subsonic solution can be extended to give an approximate solution in the transonic flow regime. It is also possible to use a velocity-gradient method of analysis alone to obtain subsonic, transonic, or supersonic solutions without assumptions other than the basic ones indicated earlier. The velocity-gradient analysis is often called a stream-filament analysis because the velocity-gradient equation involves the streamline, or stream-filament, curvature and position.

A velocity-gradient method of analysis can only give solutions within a guided passage; that is, a passage where both ends of all streamline orthogonals intersect a solid boundary. Therefore, the usefulness of this method depends on the degree of flow guidance provided by the turbine blades. For a well-guided passage (high solidity and/or small angles), such as shown in figure 4–11, most of the suction surface is within the guided region, and the associated surface velocity distribution can be well defined. On the other hand, for a low-solidity blade row, such as that shown in figure 5–9, less than half of the suction surface is within the guided region, and surface velocities can be computed only on the front half of the suction surface. In this latter case, the stream-function analysis must be used if better definition of the suction-surface velocity distribution is required.

Method

The idea of a velocity-gradient method can be demonstrated by considering a simple case. Suppose we have two-dimensional flow through a narrow passage as shown in figure 5–13. We assume the height of the passage to be b, and the width d. If the mass flow is known, the average velocity can be calculated approximately from continuity by

$$W_{avg} = \frac{w}{\rho b d} \tag{5–60}$$

However, there is a variation in velocity across the width of the passage, and in turbomachinery it is this velocity difference we are interested in. With a force-equilibrium equation, by balancing centrifugal force against the pressure gradient as was done in chapter 3 for consideration of radial equilibrium, it can be shown that

$$\frac{dW}{dq} = \frac{W}{r_c} \tag{5–61}$$

where q is the distance from the suction (convex) surface, and r_c is the radius of curvature for the streamline. The sign convention for r_c is important; r_c is positive if it is concave upward, and negative if it is concave downward. For the simple case shown in figure 5–13, equation (5–61) can be integrated along a radial line by assuming the streamline radius of curvature to be equal in magnitude to the passage radius. There results, for integration from the inner radius to any point in the passage,

$$\frac{W}{W_s} = \frac{r_s}{r} \tag{5–62}$$

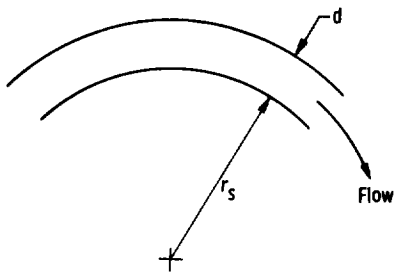

FIGURE 5–13.—Flow through a curved passage.

where

W_s relative velocity on inner, or suction, surface, m/sec; ft/sec
r_s radius of inner, or suction, surface, m; ft
r radius of passage, m; ft

The mass flow through the passage is expressed as

$$w = \int_{r_s}^{r_s+d} \rho W b \, dr \tag{5–63}$$

and substitution of equation (5–62) into (5–63) and integration, with constant density assumed, yields

$$W_s = \frac{w}{\rho b r_s \ln\left(1+\frac{d}{r_s}\right)} \tag{5–64}$$

In a similar manner, the outer, or pressure, surface velocity can be computed as

$$W_p = \frac{w}{\rho b r_s \left(1+\frac{d}{r_s}\right) \ln\left(1+\frac{d}{r_s}\right)} \tag{5–65}$$

Thus, an estimate of the blade-surface velocities can be obtained simply by using equation (5–62), which is a velocity-gradient equation. We are not necessarily restricted to two-dimensional flow. If there were some variation of velocity in the height of the passage, a velocity gradient could be calculated in that direction also.

We will now consider a very general velocity-gradient equation. Since we are interested in turbomachinery, we will use a rotating cylindrical coordinate system with radius r, angle θ, and axis x, as shown in figure 5–14. Also indicated are the velocity components, W_r, W_x, and W_θ. The meridional component W_m is the resultant of W_r and W_x. The meridional plane is a plane containing the x axis. Also shown in figure 5–14 are α, the angle between W_m and the x axis, and β, the angle between W and the meridional plane. The following relations hold for the components:

$$W_\theta = W \sin \beta \tag{5–66}$$

$$W_m = W \cos \beta \tag{5–67}$$

$$W_r = W_m \sin \alpha \tag{5–68}$$

$$W_x = W_m \cos \alpha \tag{5–69}$$

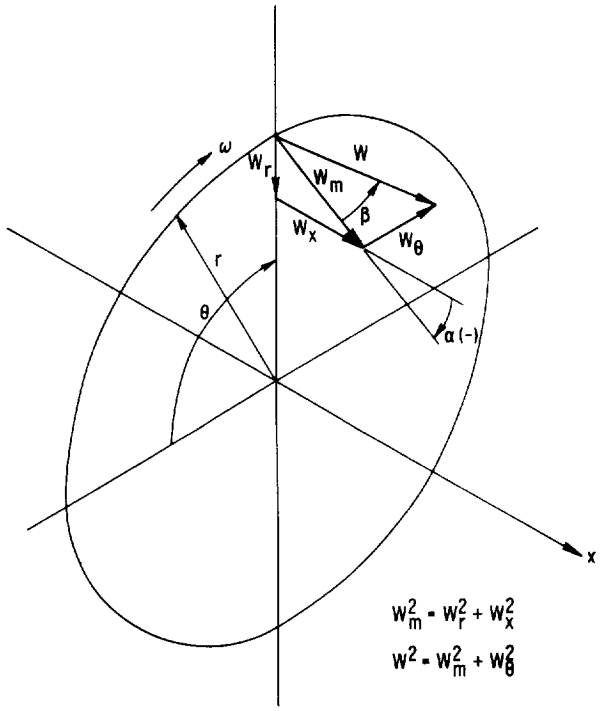

FIGURE 5–14.—Cylindrical coordinate system and velocity components.

In addition to the r-, θ-, and x-coordinate, it is convenient to use an m-coordinate. The m-coordinate is the distance along a meridional streamline, as shown in figure 5–15. The m-distance is less than the true streamline distance if the angle $\beta \neq 0$. The meridional streamline is the projection of a streamline in the meridional plane; that is, the θ-coordinate is neglected. The curvature of the meridional streamline is $1/r_c$, where r_c is the radius of curvature of the meridional streamline. The sign of r_c is positive if the streamline is concave upward.

We want the velocity gradient along an arbitrary curve. Let q be the distance along this curve. For the case of constant total temperature and constant angular momentum (rV_u) at the inlet,

$$\frac{dW}{dq} = a\frac{dr}{dq} + b\frac{dx}{dq} + c\frac{d\theta}{dq} \tag{5–70}$$

where

$$a = \frac{W\cos\alpha\cos^2\beta}{r_c} - \frac{W\sin^2\beta}{r} + \sin\alpha\cos\beta\frac{dW_m}{dm} - 2\omega\sin\beta \tag{5–71}$$

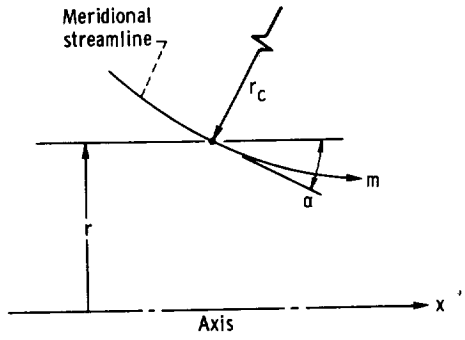

FIGURE 5–15.—The m-coordinate.

$$b = -\frac{W \sin \alpha \cos^2 \beta}{r_c} + \cos \alpha \cos \beta \frac{dW_m}{dm} \tag{5–72}$$

$$c = W \sin \alpha \sin \beta \cos \beta + r \cos \beta \left(\frac{dW_\theta}{dm} + 2\omega \sin \alpha \right) \tag{5–73}$$

These equations are derived as equations (B13) and (B14) of reference 11. In using any velocity-gradient equation, it is necessary to solve a differential equation involving streamline-geometry parameters, such as curvature, α, and β. These are not known precisely in advance. However, for a guided channel, these parameters can be estimated reasonably well.

A great number of special cases can be obtained from equations (5–70) to (5–73). For example, suppose we have an annular passage with no blades, as shown in figure 5–16, and no velocity component in the tangential (θ) direction (into page). We can calculate dW/dn, where n is the distance normal to the streamline. Let $q = n$ in equation (5–70). Since $W_\theta = 0$, then $d\theta/dn = 0$ and $\beta = 0$. Further, from figure 5–16, it can be

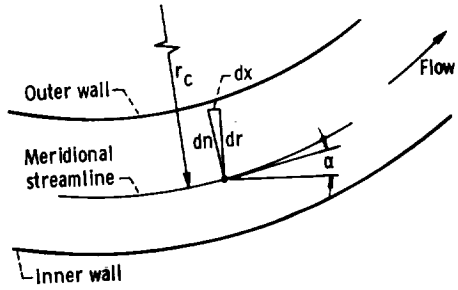

FIGURE 5–16.—Annular passage with no blades.

seen that $dr/dn = \cos \alpha$ and $dx/dn = -\sin \alpha$. Then, from equations (5–70) to (5–73),

$$\frac{dW}{dn} = \frac{W}{r_c} \tag{5–74}$$

Thus, for this case, equation (5–70) reduces to the simple form of equation (5–61).

Computer Programs

Several computer programs for the analysis of flow through turbomachine blading by velocity-gradient methods have been written at the NASA Lewis Research Center. One that was used for many years is the CTTD program, which is described in reference 12 and is limited to axial-flow turbines. This program has now been superseded by the more general and easier to use CHANEL program, which is described in reference 13. The CHANEL program can be used to analyze axial-, radial-, or mixed-flow turbines or compressors. Velocity-gradient equations are used to determine velocity variations both from hub to tip along meridional-streamline orthogonals and from blade to blade along hub-, mean-, and tip-streamline orthogonals. This results in a flow solution for an orthogonal surface, as illustrated in figure 5–17, which satisfies a specified mass flow rate. Computations are made for a number of these surfaces along the blade passage. This program can also be used to compute the maximum (choking) mass flow rate for the channel. The program gives good results for medium- to high-solidity blading. As indicated previously, more definition than can be provided by this program may be needed for low-solidity blading, because solutions can only be obtained for fully guided sections of the passage.

Velocity-gradient methods have also been used to obtain meridional-plane and blade-to-blade plane solutions. The basic method for a meridional-plane analysis for mixed-flow centrifugal impellers is presented in reference 14, which uses the velocity-gradient equation along streamline orthogonals. Since the orthogonal lengths are not known in advance, it was more convenient to base a computer program on the use of the velocity-gradient equation along fixed straight lines, which were called quasi-orthogonals. Such programs for meridional-plane analysis are presented in reference 11 for a radial-inflow turbine impeller and in reference 15 for backward-swept or radial impellers and vaned diffusers of centrifugal compressors. A program for a blade-to-blade plane analysis that uses quasi-orthogonals for a radial-inflow turbine impeller is described in reference 16.

A further use of the velocity-gradient equation, as mentioned previously in this chapter, is to extend a subsonic stream-function solution to

obtain local supersonic velocities. The subsonic solution is used to obtain the flow angles and streamline curvatures required for the velocity-gradient equation. Programs for transonic-flow solutions based on this method are presented in references 9 and 10 for a meridional solution and in reference 6 for a blade-to-blade solution.

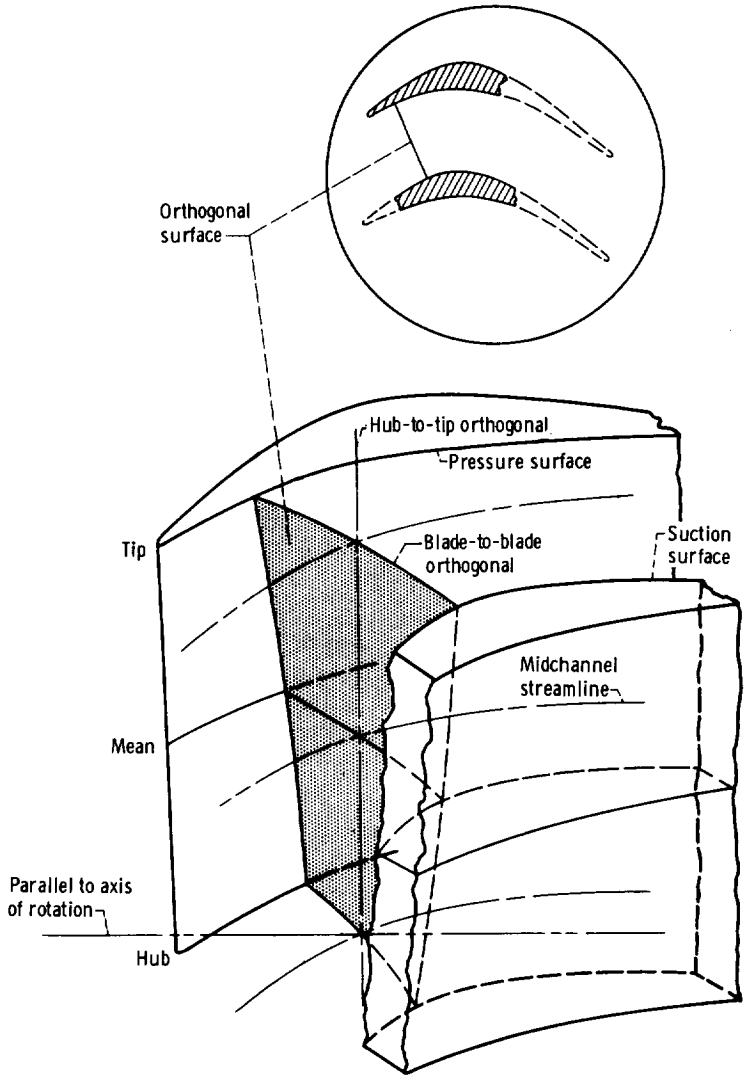

FIGURE 5–17.—Turbine blades with three-dimensional orthogonal surface across flow passage.

REFERENCES

1. JOHNSEN, IRVING A.; AND BULLOCK, ROBERT O., EDS.: Aerodynamic Design of Axial-Flow Compressors. NASA SP-36, 1965.
2. COSTELLO, GEORGE R.: Method of Designing Cascade Blades with Prescribed Velocity Distributions in Compressible Potential Flows. NACA Rep. 978, 1950.
3. COSTELLO, GEORGE R.; CUMMINGS, ROBERT L.; AND SINNETTE, JOHN T., JR.: Detailed Computational Procedure for Design of Cascade Blades with Prescribed Velocity Distributions in Compressible Potential Flows. NACA Rep. 1060, 1952.
4. VARGA, RICHARD S.: Matrix Iterative Analysis. Prentice-Hall, Inc., 1962.
5. KATSANIS, THEODORE; AND MCNALLY, WILLIAM D.: Revised FORTRAN Program for Calculating Velocities and Streamlines on a Blade-to-Blade Stream Surface of a Turbomachine. NASA TM X-1764, 1969.
6. KATSANIS, THEODORE: FORTRAN Program for Calculating Transonic Velocities on a Blade-to-Blade Stream Surface of a Turbomachine. NASA TN D-5427, 1969.
7. KATSANIS, THEODORE; AND MCNALLY, WILLIAM D.: FORTRAN Program for Calculating Velocities and Streamlines on a Blade-to-Blade Stream Surface of a Tandem Blade Turbomachine. NASA TN D-5044, 1969.
8. KATSANIS, THEODORE; AND MCNALLY, WILLIAM D.: FORTRAN Program for Calculating Velocities in a Magnified Region on a Blade-to-Blade Stream Surface of a Turbomachine. NASA TN D-5091, 1969.
9. KATSANIS, THEODORE; AND MCNALLY, WILLIAM D.: FORTRAN Program for Calculating Velocities and Streamlines on the Hub-Shroud Mid-Channel Flow Surface of an Axial- or Mixed-Flow Turbomachine. I—User's Manual. NASA TN D-7343, 1973.
10. KATSANIS, THEODORE; AND MCNALLY, WILLIAM D.: FORTRAN Program for Calculating Velocities and Streamlines on the Hub-Shroud Mid-Channel Flow Surface of an Axial- or Mixed-Flow Turbomachine. II—Programmer's Manual. NASA TN D-7344, 1974.
11. KATSANIS, THEODORE: Use of Arbitrary Quasi-Orthogonals for Calculating Flow Distribution in the Meridional Plane of a Turbomachine. NASA TN D-2546, 1964.
12. KATSANIS, THEODORE; AND DELLNER, LOIS T.: A Quasi-Three-Dimensional Method for Calculating Blade-Surface Velocities for an Axial Flow Turbine Blade. NASA TM X-1394, 1967.
13. KATSANIS, THEODORE: FORTRAN Program for Quasi-Three-Dimensional Calculation of Surface Velocities and Choking Flow for Turbomachine Blade Rows. NASA TN D-6177, 1971.
14. HAMRICK, JOSEPH T.; GINSBURG, AMBROSE; AND OSBORNE, WALTER M.: Method of Analysis for Compressible Flow Through Mixed-Flow Centrifugal Impellers of Arbitrary Design. NACA Rep. 1082, 1952.
15. VANCO, MICHAEL R.: FORTRAN Program for Calculating Velocities in the Meridional Plane of a Turbomachine. I—Centrifugal Compressor. NASA TN D-6701, 1972.
16. KATSANIS, THEODORE: Use of Arbitrary Quasi-Orthogonals for Calculating Flow Distribution on a Blade-to-Blade Surface in a Turbomachine. NASA TN D-2809, 1965.

SYMBOLS

A	flow area, m^2; ft^2
a_i	coefficients for equation (5–46)
b	cascade height, m; ft
d	passage width, m; ft
h	distance between mesh points, m; ft
k_i	constant in equation (5–56)
m	distance along meridional streamline, m; ft
n	distance normal to streamline, m; ft
p	absolute pressure, N/m^2; lb/ft^2
q	distance along arbitrary curve, m; ft
R	gas constant, J/(kg)(K); (ft)(lbf)/(lbm)(°R)
r	radius, m; ft
s	blade spacing, m; ft
T	absolute temperature, K; °R
t	time, sec
u	stream function
V	absolute velocity, m/sec; ft/sec
W	relative velocity, m/sec; ft/sec
w	mass flow rate, kg/sec; lb/sec
α	fluid absolute angle of inclination from axial direction in the meridional plane, deg
β	fluid flow angle, relative to blades, out of the meridional plane (in the tangential direction), deg
η	distance in direction of outer normal to cascade boundary, m; ft
θ	angular distance in direction of rotation, rad
ρ	density, kg/m^3; lb/ft^3
Φ	potential function
ω	angular velocity, rad/sec overrelaxation factor

Subscripts:

c	curvature
in	inlet
m	meridional component
n	component normal to streamline
out	outlet
p	pressure surface
r	radial component
s	suction surface
x	axial component
y	component in y-direction
z	component in z-direction

θ	tangential component
0, 1, 2, 3, 4	mesh-point designations

CHAPTER 6

Introduction to Boundary-Layer Theory

By William D. McNally

As shown in chapter 2, the pressure ratio across a turbine provides a certain amount of ideal energy that is available to the turbine for producing work. The portion of the ideal energy that is not converted to work is considered to be a loss. One of the more important and difficult aspects of turbine design is the prediction of the losses.

Before losses can be predicted, it is necessary to understand their causes. The primary cause of losses is the boundary layer that develops on the blade and end-wall surfaces. Other losses occur because of shocks, tip-clearance flows, disk friction (windage), flow incidence, and partial-admission operation. This chapter gives an introduction to boundary-layer theory, which is used to calculate the parameters needed to estimate viscous (friction) losses. Methods for determining the basic viscous loss and the associated trailing-edge and mixing losses are presented in the next chapter.

NATURE OF BOUNDARY LAYER

When a real fluid (such as air) flows past a turbine blade at normal velocities, the influence of viscosity on the flow is confined to a relatively thin layer in the immediate neighborhood of the blade. This layer is called the boundary layer. At the outer edge of this layer the flow is frictionless, and conditions there agree with those calculated with the use of ideal (frictionless, nonviscous) flow assumptions. At the wall, on the other hand, the velocity of the fluid is zero in all directions (no-slip condition).

It is the frictional, or viscous, forces in this thin layer that reduce the fluid velocity from its free-stream, frictionless value to zero at the wall.

A boundary layer on a turbine blade is illustrated in figure 6–1. The boundary layer develops from a small finite thickness at the stagnation point at the leading edge of the blade and grows along both the suction and pressure surfaces. The initial portion of the boundary layer is always laminar. In a laminar boundary layer, fluid layers parallel to the blade surface slide over each other. Any minute local fluctuations in velocity are sufficiently damped so that they have negligible influence on the smoothness of the overall flow. The velocity at a point is either steady with time or changes in some smooth way, as figure 6–2(a) indicates.

Most flows being ducted to a turbine, or entering it from a combustor, are turbulent in nature. The fluctuating components of velocity have a significant influence in this type of flow. With this overall flow, the boundary layer on the blades cannot remain laminar for any great distance. It usually passes through a transition region and becomes a turbulent boundary layer. In the transition region, weak disturbances in the flow are amplified, and this leads to the random fluctuations in velocity that are characteristic of turbulent flow. In the turbulent boundary layer, as in turbulent flow, the velocity at any point oscillates in a random fashion about a mean value, as figure 6–2(b) indicates.

Figure 6–1 also shows a separated region in the turbulent boundary layer. Separation can likewise occur in the laminar boundary layer. When a boundary layer separates, the fluid moves away from the blade surface. The manner in which this happens is illustrated in figure 6–3. As the free-stream velocity decreases along the rear portion of the suction surface of a turbine blade, static pressure correspondingly increases. This positive

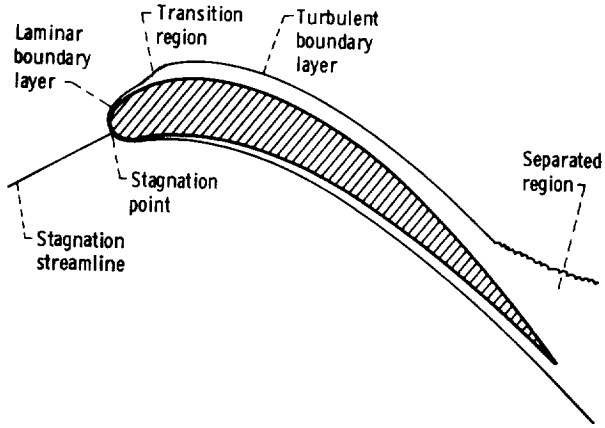

FIGURE 6–1.—Boundary layer on blade.

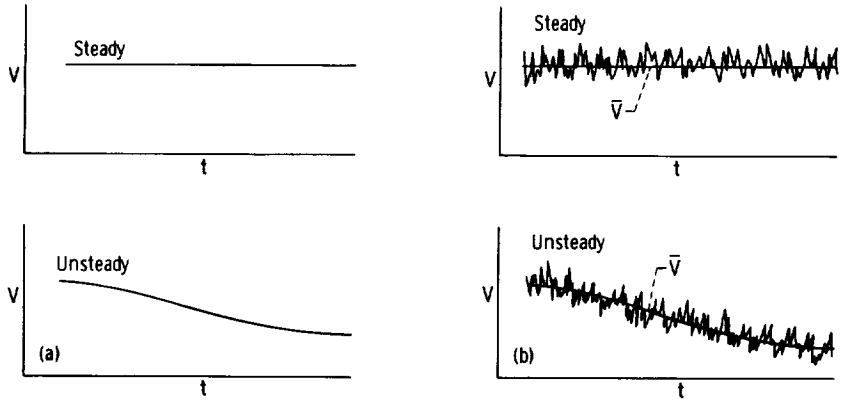

(a) Laminar flow. (b) Turbulent flow.

FIGURE 6–2.—Variation of velocity with time at a point.

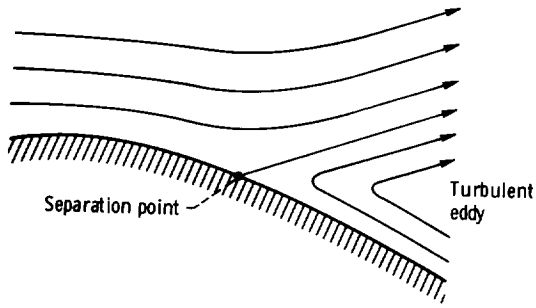

FIGURE 6–3.—Boundary-layer separation.

pressure gradient (adverse pressure gradient) retards the flow in the boundary layer and causes it to lose energy. The flow in the boundary layer can be retarded to such a degree that very close to the wall it moves in a direction opposite to that of the mean flow passing the blade. This is separation. The point at which the flow reverses itself is the separation point. The laminar boundary layer at the leading edge of a turbine blade can also separate and immediately reattach itself to the surface as a turbulent boundary layer. This is illustrated in figure 6–4.

Finally, it should be noted that both laminar and turbulent boundary layers can be either incompressible or compressible, depending on the level of the Mach number. Just as there are different equations to represent laminar and turbulent boundary-layer flow, there are different equations for the incompressible and compressible variations of each.

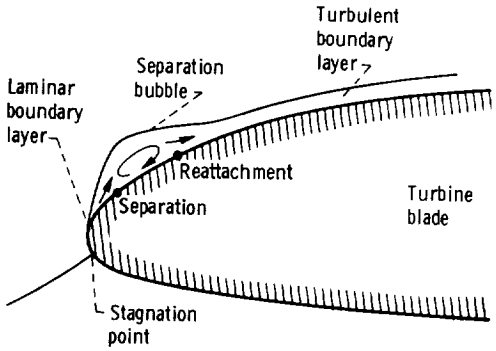

FIGURE 6–4.—Laminar separation and reattachment.

Boundary layers should be considered compressible if the free-stream relative Mach number exceeds values of 0.3 to 0.4. The boundary-layer equations for these various cases are derived and solution methods are discussed in this chapter.

DERIVATION OF BOUNDARY-LAYER EQUATIONS

The general equations of motion of viscous fluids are called the Navier-Stokes equations. In normal coordinate systems, there are three such equations, one for each of the coordinate directions. The boundary-layer equations can be derived from the Navier-Stokes equations. The Navier-Stokes equations themselves can be derived by applying the law of conservation of momentum to a fluid element. This exercise is lengthy, and will not be repeated here. References 1 and 2 both have the complete derivation, in two somewhat different forms.

There are various forms of the Navier-Stokes equations, depending on what assumptions are made during their derivation. The following equation represents the Navier-Stokes equations combined into vector form for a compressible fluid with constant viscosity:

$$\frac{d\mathbf{u}}{dt}=g\mathbf{f}-\frac{g}{\rho}\nabla p+\frac{\mu}{\rho}\nabla^2\mathbf{u}+\frac{1}{3}\frac{\mu}{\rho}\nabla(\nabla\cdot\mathbf{u}) \qquad (6\text{–}1)$$

where

$\mathbf{u}$ general velocity vector, m/sec; ft/sec
t time, sec
g conversion constant, 1; 32.17 (lbm)(ft)/(lbf)(sec^2)
$\mathbf{f}$ general body force acting on a unit mass of fluid, N/kg; lbf/lbm

ρ density, kg/m³; lbm/ft³
p static pressure, N/m²; lbf/ft²
μ dynamic viscosity, (N)(sec)/m²; lbm/(ft)(sec)

In this equation, **u** represents a general velocity vector with components u, v, and w in the three coordinate directions x, y, and z, respectively.

$$\mathbf{u} = u\mathbf{i} + v\mathbf{j} + w\mathbf{k} \tag{6–2}$$

where **i**, **j**, and **k** are the unit vectors in the three coordinate directions. The total, or substantial, derivative of **u** is $d\mathbf{u}/dt$. In any of the coordinate directions,

$$\frac{d}{dt} = \frac{\partial}{\partial t} + u\frac{\partial}{\partial x} + v\frac{\partial}{\partial y} + w\frac{\partial}{\partial z} \tag{6–3}$$

In equation (6–1), the Laplacian operator ∇^2 is applied to the vector **u** rather than to a scalar function. If the term $\nabla^2\mathbf{u}$ is expanded into simple vector quantities, equation (6–1) becomes

$$\frac{d\mathbf{u}}{dt} = g\mathbf{f} - \frac{g}{\rho}\nabla p + \frac{\mu}{\rho}\nabla(\nabla\cdot\mathbf{u}) - \frac{\mu}{\rho}[\nabla\times(\nabla\times\mathbf{u})] + \frac{1}{3}\frac{\mu}{\rho}\nabla(\nabla\cdot\mathbf{u}) \tag{6–4}$$

Expressing the ∇ operator in terms of gradients, curls, and divergences, which may be more familiar to the reader, equation (6–4) becomes

$$\frac{d\mathbf{u}}{dt} = g\mathbf{f} - \frac{g}{\rho}\operatorname{grad} p + \frac{\mu}{\rho}\operatorname{grad}(\operatorname{div}\mathbf{u}) - \frac{\mu}{\rho}\operatorname{curl}(\operatorname{curl}\mathbf{u}) + \frac{1}{3}\frac{\mu}{\rho}\operatorname{grad}(\operatorname{div}\mathbf{u}) \tag{6–5}$$

In order to derive the boundary-layer equations, equation (6–1) has to be expanded into three scalar equations, one for each of the coordinate directions. The three resulting equations are

$$\frac{\partial u}{\partial t} + u\frac{\partial u}{\partial x} + v\frac{\partial u}{\partial y} + w\frac{\partial u}{\partial z} = gf_x - \frac{g}{\rho}\frac{\partial p}{\partial x} + \frac{\mu}{\rho}\left(\frac{\partial^2 u}{\partial x^2} + \frac{\partial^2 u}{\partial y^2} + \frac{\partial^2 u}{\partial z^2}\right) + \frac{1}{3}\frac{\mu}{\rho}\frac{\partial}{\partial x}\left(\frac{\partial u}{\partial x} + \frac{\partial v}{\partial y} + \frac{\partial w}{\partial z}\right) \tag{6–6}$$

$$\frac{\partial v}{\partial t} + u\frac{\partial v}{\partial x} + v\frac{\partial v}{\partial y} + w\frac{\partial v}{\partial z} = gf_y - \frac{g}{\rho}\frac{\partial p}{\partial y} + \frac{\mu}{\rho}\left(\frac{\partial^2 v}{\partial x^2} + \frac{\partial^2 v}{\partial y^2} + \frac{\partial^2 v}{\partial z^2}\right) + \frac{1}{3}\frac{\mu}{\rho}\frac{\partial}{\partial y}\left(\frac{\partial u}{\partial x} + \frac{\partial v}{\partial y} + \frac{\partial w}{\partial z}\right) \tag{6–7}$$

$$\frac{\partial w}{\partial t}+u\frac{\partial w}{\partial x}+v\frac{\partial w}{\partial y}+w\frac{\partial w}{\partial z}=gf_z-\frac{g}{\rho}\frac{\partial p}{\partial z}+\frac{\mu}{\rho}\left(\frac{\partial^2 w}{\partial x^2}+\frac{\partial^2 w}{\partial y^2}+\frac{\partial^2 w}{\partial z^2}\right)$$

$$+\frac{1}{3}\frac{\mu}{\rho}\frac{\partial}{\partial z}\left(\frac{\partial u}{\partial x}+\frac{\partial v}{\partial y}+\frac{\partial w}{\partial z}\right) \quad (6\text{–}8)$$

where f_x, f_y, and f_z are the components of the body force **f**.

Laminar Incompressible Boundary Layer

In order to derive Prandtl's boundary-layer equations for laminar incompressible flow, the following assumptions will be made:

(1) Viscosity is a constant. This has already been assumed in the writing of the preceding equations.

(2) Flow is incompressible. Since for incompressible flow the continuity equation is

$$\nabla\cdot\mathbf{u}=\text{div }\mathbf{u}=\left(\frac{\partial u}{\partial x}+\frac{\partial v}{\partial y}+\frac{\partial w}{\partial z}\right)=0 \quad (6\text{–}9)$$

the final terms in equations (6–6) to (6–8) can be eliminated.

(3) Flow is two-dimensional. This eliminates equation (6–8) from consideration, as well as all terms involving w or $\partial/\partial z$ in equations (6–6) and (6–7).

(4) Flow is steady. This eliminates $\partial/\partial t$ terms.

(5) Body forces are negligible in relation to inertia and viscous forces. Thus, f_x and f_y can be discarded from equations (6–6) and (6–7).

With these assumptions, the Navier-Stokes equations reduce to the following two equations for the x- and y-directions:

$$u\frac{\partial u}{\partial x}+v\frac{\partial u}{\partial y}=-\frac{g}{\rho}\frac{\partial p}{\partial x}+\frac{\mu}{\rho}\left(\frac{\partial^2 u}{\partial x^2}+\frac{\partial^2 u}{\partial y^2}\right) \quad (6\text{–}10)$$

$$u\frac{\partial v}{\partial x}+v\frac{\partial v}{\partial y}=-\frac{g}{\rho}\frac{\partial p}{\partial y}+\frac{\mu}{\rho}\left(\frac{\partial^2 v}{\partial x^2}+\frac{\partial^2 v}{\partial y^2}\right) \quad (6\text{–}11)$$

Likewise, the continuity equation becomes

$$\frac{\partial u}{\partial x}+\frac{\partial v}{\partial y}=0 \quad (6\text{–}12)$$

In order to make equations (6–10) to (6–12) suitable for the analysis of boundary-layer flow, the equations are traditionally made dimensionless, and an order-of-magnitude check is performed on the various terms to show that some are negligible with respect to others. Figure 6–5 shows the velocities and coordinate directions pertinent to the boundary layer.

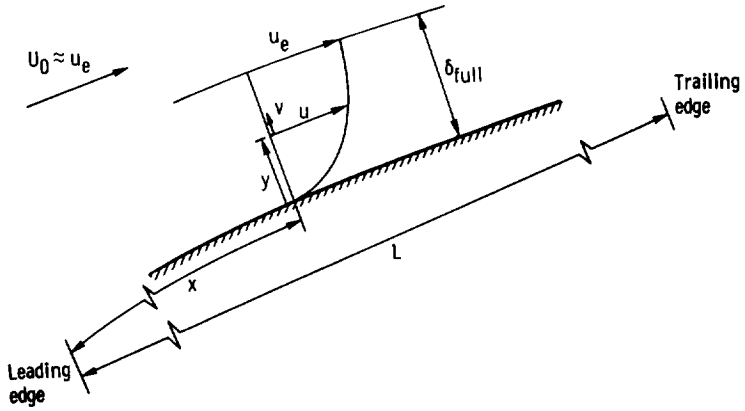

FIGURE 6–5.—Boundary-layer velocities and dimensions.

The following dimensionless parameters are defined:

$$X = \frac{x}{L} \tag{6–13a}$$

$$Y = \frac{y}{L} \tag{6–13b}$$

$$U = \frac{u}{U_0} \tag{6–13c}$$

$$V = \frac{v}{U_0} \tag{6–13d}$$

$$P = \frac{gp}{\rho U_0^2} \tag{6–13e}$$

$$Re = \frac{\rho L U_0}{\mu} \tag{6–13f}$$

where

X dimensionless x-coordinate
L characteristic length (in this case, the blade chord), m; ft
Y dimensionless y-coordinate
U dimensionless velocity in x-direction
U_0 free-stream velocity upstream of blade, m/sec; ft/sec
V dimensionless velocity in y-direction

P dimensionless pressure
Re Reynolds number

From figure 6–5, we see that since x is proportional to L, X is of order 1. And since y is proportional to the boundary-layer thickness δ_{full}, Y is of order $\delta_{full}/L = \epsilon$, a quantity much less than 1. Likewise, since u is of order U_0, $U = u/U_0$ is of order 1. And $V = v/U_0$ is of order ϵ, since velocities in the y-direction in the boundary layer are much smaller than those in the x-direction.

In order to put equations (6–10) to (6–12) in terms of dimensionless quantities, equations (6–10) and (6–11) are multiplied by L/U_0^2, and equation (6–12) is multiplied by L/U_0. The resulting dimensionless equations are

$$U\frac{\partial U}{\partial X}+V\frac{\partial U}{\partial Y}=-\frac{\partial P}{\partial X}+\frac{1}{Re}\left(\frac{\partial^2 U}{\partial X^2}+\frac{\partial^2 U}{\partial Y^2}\right) \tag{6–14}$$

$$U\frac{\partial V}{\partial X}+V\frac{\partial V}{\partial Y}=-\frac{\partial P}{\partial Y}+\frac{1}{Re}\left(\frac{\partial^2 V}{\partial X^2}+\frac{\partial^2 V}{\partial Y^2}\right) \tag{6–15}$$

$$\frac{\partial U}{\partial X}+\frac{\partial V}{\partial Y}=0 \tag{6–16}$$

The order of magnitude of the various terms in these equations can now be compared with each other. Since X and U are of order 1, and Y and V are of order ϵ,

$$\frac{\partial U}{\partial X}\approx\frac{1}{1}=1 \tag{6–17a}$$

$$\frac{\partial U}{\partial Y}\approx\frac{1}{\epsilon} \tag{6–17b}$$

$$\frac{\partial V}{\partial X}\approx\frac{\epsilon}{1}=\epsilon \tag{6–17c}$$

$$\frac{\partial V}{\partial Y}\approx\frac{\epsilon}{\epsilon}=1 \tag{6–17d}$$

$$\frac{\partial^2 U}{\partial X^2}\approx\frac{1}{1\cdot 1}=1 \tag{6–17e}$$

$$\frac{\partial^2 U}{\partial Y^2}\approx\frac{1}{\epsilon\cdot\epsilon}=\frac{1}{\epsilon^2} \tag{6–17f}$$

$$\frac{\partial^2 V}{\partial X^2} \approx \frac{\epsilon}{1 \cdot 1} = \epsilon \tag{6–17g}$$

$$\frac{\partial^2 V}{\partial Y^2} \approx \frac{\epsilon}{\epsilon \cdot \epsilon} = \frac{1}{\epsilon} \tag{6–17h}$$

Furthermore, the change in P with respect to X is of the same order of magnitude as the change of U with respect to X, so that $\partial P/\partial X$ is of order 1.

Relating these orders of magnitude to the terms in equations (6–14) to (6–16) yields

$$U\frac{\partial U}{\partial X} + V\frac{\partial U}{\partial Y} = -\frac{\partial P}{\partial X} + \frac{1}{Re}\left(\frac{\partial^2 U}{\partial X^2} + \frac{\partial^2 U}{\partial Y^2}\right) \tag{6–18}$$

$$(1)(1) + (\epsilon)\left(\frac{1}{\epsilon}\right) = -1 + (\epsilon^2)\left(1 + \frac{1}{\epsilon^2}\right)$$

$$U\frac{\partial V}{\partial X} + V\frac{\partial V}{\partial Y} = -\frac{\partial P}{\partial Y} + \frac{1}{Re}\left(\frac{\partial^2 V}{\partial X^2} + \frac{\partial^2 V}{\partial Y^2}\right) \tag{6–19}$$

$$(1)(\epsilon) + (\epsilon)(1) = -\epsilon + (\epsilon^2)\left(\epsilon + \frac{1}{\epsilon}\right)$$

$$\frac{\partial U}{\partial X} + \frac{\partial V}{\partial Y} = 0 \tag{6–20}$$

$$1 + 1$$

By examining equations (6–18) to (6–20), the following conclusions can be reached:

(1) In boundary-layer theory, it is assumed that the viscous terms $1/Re[(\partial^2 U/\partial X^2) + (\partial^2 U/\partial Y^2)]$ are of the same order of magnitude as the inertia terms $U(\partial U/\partial X) + V(\partial U/\partial Y)$. For this to be true in equation (6–18), $1/Re$ must be of order ϵ^2, since $\partial^2 U/\partial Y^2$ is much larger than $\partial^2 U/\partial X^2$ and dominates the two terms in parentheses. Therefore, the Reynolds number must be relatively large.

(2) In equation (6–19), with $1/Re$ of order ϵ^2 and with $\partial^2 V/\partial Y^2$ dominating $\partial^2 V/\partial X^2$, the terms are of order ϵ. Therefore, unless $\partial P/\partial Y$ is to dominate, it too must be of order ϵ or less. Therefore, $\partial P/\partial Y$ is much smaller than $\partial P/\partial X$, and P can be considered a function of X alone. Therefore, $P = P(X)$ or $p = p(x)$, and $\partial P/\partial X = dP/dX$ or $\partial p/\partial x = dp/dx$. This allows us to assume that the pressure across the boundary layer in the

y-direction is essentially constant. It can be assumed equal to the potential flow pressure existing at the outside of the boundary layer.

(3) Since the first equation is of order 1, and the second equation is of order ϵ, the second equation can be neglected completely.

(4) In equation (6–18), $\partial^2 U/\partial X^2$ can be neglected because it is so small in comparison with $\partial^2 U/\partial Y^2$. This leaves the following dimensionless equations:

$$U\frac{\partial U}{\partial X}+V\frac{\partial U}{\partial Y}=-\frac{dP}{dX}+\frac{1}{Re}\frac{\partial^2 U}{\partial Y^2} \tag{6–21}$$

$$\frac{\partial U}{\partial X}+\frac{\partial V}{\partial Y}=0 \tag{6–22}$$

These are Prandtl's boundary-layer equations in dimensionless form.

The boundary-layer equations in this form are useful in determining the influence of the Reynolds number on the size of the boundary layer for different fluids. From equation (6–21) we see that as Re increases in magnitude, the viscous-force terms $(1/Re)(\partial^2 U/\partial Y^2)$ will get smaller and smaller. The boundary-layer thickness will correspondingly decrease. So, as Re increases, δ_{full} decreases. Furthermore, increasing Re corresponds to decreasing viscosity if $\rho L U_0$ is constant. So, as a general rule, the thickness of the boundary layer decreases as the viscosity decreases.

The boundary-layer equations can be put in terms of dimensional variables by multiplying equation (6–21) by U_0^2/L and equation (6–22) by U_0/L. The resulting equations are

$$u\frac{\partial u}{\partial x}+v\frac{\partial u}{\partial y}=-\frac{g}{\rho}\frac{dp}{dx}+\frac{\mu}{\rho}\frac{\partial^2 u}{\partial y^2} \tag{6–23}$$

$$\frac{\partial u}{\partial x}+\frac{\partial v}{\partial y}=0 \tag{6–24}$$

These are Prandtl's boundary-layer equations for two-dimensional, laminar, incompressible flow. Density and viscosity are assumed constant and known. The pressure gradient along the blade surface, dp/dx, is also known from an ideal-flow solution. The remaining unknowns are u and v, and equations (6–23) and (6–24) are sufficient for their calculation.

It should be noted that the boundary-layer equations are not valid in the presence of shock waves (i.e., where instantaneous adverse pressure gradients of large magnitude occur). Just as flow phenomena in the boundary layer depend on mainly the Reynolds number, conditions in a shock wave depend on primarily the Mach number. Since the influence of Mach number is not included in the boundary-layer equations, they tell us nothing about the interaction of shock waves and boundary layers.

The boundary-layer equations are not completely reliable as separation is approached. One of the assumptions used in their derivation is that the velocity v is much smaller than u. Very close to the separation point, the boundary layer grows rapidly, and v begins to be of the same order as u. Nonetheless, the boundary-layer equations are generally used in calculations right up to the separation point, since the region where V is significant is very small, and little error in the location of the point of separation is incurred. However, these equations should not be used for detailed calculations in the neighborhood of a separated flow region.

The Navier-Stokes equations (6–6) to (6–8) used in the development of the boundary-layer equations were derived for an orthogonal system of coordinates in which the radius of curvature of each of the coordinate axes is quite large (i.e., where curvature effects are negligible). The question arises as to how the boundary-layer equations would change for flow over a curved wall. If a curvilinear orthogonal coordinate system (fig. 6–6) is introduced wherein the x-axis is in the direction of the curved wall and the y-axis is normal to it, a new set of Navier-Stokes equations can be derived for flow in such a system. These equations are given in reference 1. The terms in the equations are very dependent on the radius of curvature r at a position x along the blade surface. The relative orders of magnitude of the individual terms can be estimated in the same manner as was done previously. With the assumption that the boundary-layer thickness is small compared with the radius of curvature of the wall, and for the case where no large variations in curvature occur, so that $dr/dx \approx 1$, the same boundary-layer equations result as were obtained for flat walls. Therefore, the flat-plate boundary-layer equations may be applied to curved walls as well, provided there are no large variations in curvature, such as would occur near sharp edges.

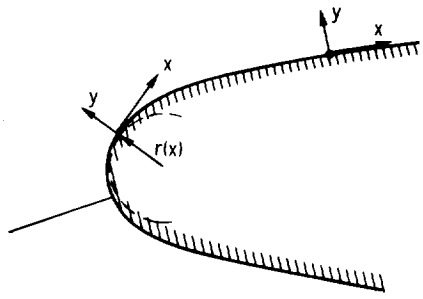

FIGURE 6–6.—Curvilinear coordinate system on a blade.

Laminar Compressible Boundary Layer

An order-of-magnitude analysis can also be performed to derive the equations for a compressible boundary layer. In the incompressible case, viscosity and density were assumed constant, temperature variations were neglected, and the energy equation was not used. For the compressible case, density is no longer constant, viscosity is considered a function of temperature, the equation of state is used to relate pressure and density to temperature, and, if the process is not isothermal, some form of the energy equation is required. The boundary-layer equations for compressible, nonisothermal, variable-viscosity flow will involve three parameters which can be related to temperature. These are viscosity, specific heat, and thermal conductivity.

There are several relations for viscosity as a function of temperature. The most common is probably Sutherland's relation (ref. 1)

$$\frac{\mu}{\mu_0}=\left(\frac{T}{T_0}\right)^{3/2}\frac{T_0+S}{T+S} \tag{6-25}$$

where

μ_0 dynamic viscosity at the reference temperature T_0, (N)(sec)/m^2; lbm/(ft)(sec)
T absolute static temperature, K; °R
T_0 reference temperature, K; °R
S a constant, K; °R (for air, $S=110$ K or 198° R)

A less complicated, but also less accurate, temperature-viscosity relation is the power law

$$\frac{\mu}{\mu_0}=\left(\frac{T}{T_0}\right)^{\omega} \qquad 0.5<\omega<1.0 \tag{6-26}$$

where ω is a constant. For air, ω is approximately 0.65.

Specific heat and thermal conductivity can be related to temperature by least-squares polynomial-curve fits for the particular gas and temperature range involved. With these variables related to temperature, the unknowns in the compressible-boundary-layer problem reduce to u, v, ρ, and T. The four equations relating these variables will be the continuity equation, one component of the momentum equation, the state equation, and the energy equation.

The order-of-magnitude analysis of the continuity and momentum (Navier-Stokes) equations for compressible flow is almost identical to that for incompressible flow. For compressible flow with nonconstant viscosity, the equations analogous to (6–10) to (6–12) are the following:

$$\rho u\frac{\partial u}{\partial x}+\rho v\frac{\partial u}{\partial y}=-g\frac{\partial p}{\partial x}+\frac{\partial}{\partial x}\left[2\mu\frac{\partial u}{\partial x}-\frac{2}{3}\mu\left(\frac{\partial u}{\partial x}+\frac{\partial v}{\partial y}\right)\right]+\frac{\partial}{\partial y}\left[\mu\left(\frac{\partial u}{\partial y}+\frac{\partial v}{\partial x}\right)\right] \tag{6-27}$$

$$\rho u\frac{\partial v}{\partial x}+\rho v\frac{\partial v}{\partial y}=-g\frac{\partial p}{\partial y}+\frac{\partial}{\partial y}\left[2\mu\frac{\partial v}{\partial y}-\frac{2}{3}\mu\left(\frac{\partial u}{\partial x}+\frac{\partial v}{\partial y}\right)\right]+\frac{\partial}{\partial x}\left[\mu\left(\frac{\partial v}{\partial x}+\frac{\partial u}{\partial y}\right)\right] \tag{6-28}$$

$$\frac{\partial(\rho u)}{\partial x}+\frac{\partial(\rho v)}{\partial y}=0 \tag{6-29}$$

If an order-of-magnitude analysis is performed on these equations similar to that for the incompressible-flow equations, the following boundary-layer equations result:

$$\rho u\frac{\partial u}{\partial x}+\rho v\frac{\partial u}{\partial y}=-g\frac{dp}{dx}+\frac{\partial}{\partial y}\left(\mu\frac{\partial u}{\partial y}\right) \tag{6-30}$$

$$\frac{\partial(\rho u)}{\partial x}+\frac{\partial(\rho v)}{\partial y}=0 \tag{6-31}$$

The equation of state is also required for the solution of compressible boundary-layer flow. The state equation is

$$p=\rho RT \tag{6-32}$$

where R is the gas constant, in J/(kg)(K) or (ft)(lbf)/(lbm)(°R).

The final equation required besides the continuity equation, the momentum equation, and the equation of state, is the energy equation. The energy equation for a compressible boundary layer is derived from the energy equation for a perfect gas by means of another order-of-magnitude check. The following is the energy equation for compressible, two-dimensional steady flow of a perfect gas, written in full:

$$\rho c_p\left(u\frac{\partial T}{\partial x}+v\frac{\partial T}{\partial y}\right)=\frac{u}{J}\frac{\partial p}{\partial x}+\frac{v}{J}\frac{\partial p}{\partial y}+\frac{\partial}{\partial x}\left(k\frac{\partial T}{\partial x}\right)+\frac{\partial}{\partial y}\left(k\frac{\partial T}{\partial y}\right)+\frac{\mu}{gJ}\varphi \tag{6-33}$$

where

c_p specific heat at constant pressure, J/(kg)(K); Btu/(lbm)(°R)
J conversion constant, 1; 778 (ft)(lbf)/Btu
k thermal conductivity, W/(m)(K); Btu/(sec)(ft)(°R)

and

$$\varphi=2\left[\left(\frac{\partial u}{\partial x}\right)^2+\left(\frac{\partial v}{\partial y}\right)^2\right]+\left(\frac{\partial v}{\partial x}+\frac{\partial u}{\partial y}\right)^2-\frac{2}{3}\left(\frac{\partial u}{\partial x}+\frac{\partial v}{\partial y}\right)^2 \tag{6-34}$$

If an order-of-magnitude check is performed on the above equations, the following boundary-layer energy equation results:

$$\rho c_p\left(u\frac{\partial T}{\partial x}+v\frac{\partial T}{\partial y}\right)=\frac{u}{J}\frac{dp}{dx}+\frac{\partial}{\partial y}\left(k\frac{\partial T}{\partial y}\right)+\frac{\mu}{gJ}\left(\frac{\partial u}{\partial y}\right)^2 \qquad (6\text{–}35)$$

Equations (6–30), (6–31), (6–32), and (6–35) are the laminar boundary-layer equations for nonisothermal, two-dimensional, compressible flow of a gas obeying the ideal gas law.

Turbulent Boundary-Layer Solution Methods

It is desirable to have a turbulent boundary layer over the major portion of turbine blades. If the boundary layer is not turbulent, separation will probably occur on the blades, with a resulting decrease in their performance. Turbulent flow has irregular fluctuations (mixing or eddy motions) superimposed on the main fluid motion (see fig. 6–2). These fluctuations are so complex that closed-form solutions are not feasible at present. Yet, the mixing motion is very important, since the stresses in the fluid due to fluctuating components of velocity are often of greater magnitude than those due to the mean motion.

There are two approaches to the solution of turbulent boundary-layer flow. The first is the exact solution of the time-dependent, three-dimensional, Navier-Stokes equations. The three-dimensional equations are required, since two-dimensional calculations could never represent the stretching of eddies, which is a prime mechanism of turbulent flow. However, even the largest computers available at the present time cannot handle three-dimensional solutions of these equations on a small enough mesh to represent the fluctuating components of velocity of turbulent flow.

The second approach is to write the equations of continuity, momentum, and energy in terms of mean and fluctuating components of pressure, density, temperature, and velocity. In this approach, the time average of the u component of velocity, for example, is denoted by $\bar{u}$ and the velocity of fluctuation by u'. So the velocities, density, pressure, and temperature are written as follows:

$$u=\bar{u}+u' \qquad (6\text{–}36a)$$

$$v=\bar{v}+v' \qquad (6\text{–}36b)$$

$$\rho=\bar{\rho}+\rho' \qquad (6\text{–}36c)$$

$$p=\bar{p}+p' \qquad (6\text{–}36d)$$

$$T=\bar{T}+T' \qquad (6\text{–}36e)$$

The fluctuations in viscosity, thermal conductivity, and specific heat are

negligible and are not considered. So these three parameters are calculated as functions of the time-averaged value of temperature.

If the flow properties listed in equations (6–36) are substituted into the continuity, momentum, and energy equations for incompressible and compressible flow, a new set of stress terms arises in thees equations. These are called the "apparent" turbulent stresses, or Reynolds stresses. They are of the form $\rho\overline{u'^2}$ and $\rho\overline{u'v'}$, where $\overline{u'v'}$ is the average over time of the product of u' and v'. These new terms in the equations add additional unknowns to the boundary-layer problem for which additional equations are not presently available. For this reason, empirical expressions or approximations are substituted for the Reynolds stress terms before the turbulent boundary-layer equations can be solved.

Turbulent Incompressible Boundary Layer

Substituting the relations of equations (6–36) into equations (6–10), (6–11), and (6–12), and then performing an order-of-magnitude analysis yields the following equations for turbulent, incompressible, boundary-layer flow:

$$\rho\bar{u}\frac{\partial\bar{u}}{\partial x}+\rho\bar{v}\frac{\partial\bar{u}}{\partial y}=-g\frac{d\bar{p}}{dx}+\frac{\partial}{\partial y}\left(\mu\frac{\partial\bar{u}}{\partial y}-\rho\overline{u'v'}\right) \tag{6–37}$$

$$\frac{\partial\bar{u}}{\partial x}+\frac{\partial\bar{v}}{\partial y}=0 \tag{6–38}$$

These equations are analogous to equations (6–23) and (6–24) for laminar flow. Notice, however, the presence of the Reynolds stress term in the momentum equation. This adds a new unknown ($\overline{u'v'}$) to the original two ($\bar{u}$ and $\bar{v}$), thereby making three unknowns with only two equations.

Turbulent Compressible Boundary Layer

Substituting the relations of equations (6–36) into equations (6–27), (6–28), (6–29), (6–32), and (6–33) and then performing an order-of-magnitude analysis yields the following equations for turbulent, compressible, boundary-layer flow:

$$\frac{\partial(\bar{\rho}\bar{u})}{\partial x}+\frac{\partial(\bar{\rho}\bar{v})}{\partial y}+\frac{\partial(\overline{\rho'v'})}{\partial y}=0 \tag{6–39}$$

$$\bar{\rho}\bar{u}\frac{\partial\bar{u}}{\partial x}+\bar{\rho}\bar{v}\frac{\partial\bar{u}}{\partial y}+\overline{\rho'v'}\frac{\partial\bar{u}}{\partial y}=-g\frac{d\bar{p}}{dx}+\frac{\partial}{\partial y}\left(\mu\frac{\partial\bar{u}}{\partial y}-\bar{\rho}\overline{u'v'}\right) \tag{6–40}$$

$$\bar{p}=\bar{\rho}R\bar{T} \tag{6–41}$$

$$\bar{\rho}c_p\left(\bar{u}\frac{\partial \bar{T}_t}{\partial x}+\bar{v}\frac{\partial \bar{T}_t}{\partial y}\right)+c_p\overline{\rho' v'}\frac{\partial \bar{T}_t}{\partial y}=\frac{\bar{u}}{J}\frac{d\bar{p}}{dx}+\frac{\partial}{\partial y}\left(k\frac{\partial \bar{T}_t}{\partial y}\right)$$

$$+\frac{1}{gJ}\frac{\partial}{\partial y}\left[\left(\mu-\frac{k}{c_p}\right)\left(\bar{u}\frac{\partial \bar{u}}{\partial y}\right)\right]-\frac{\partial}{\partial y}\left[c_p\bar{\rho}(\overline{v'T'})\right] \quad (6\text{–}42)$$

where T_t is the absolute total temperature, in K or °R, and is defined as

$$T_t = T+\frac{u^2+v^2}{2gJc_p} \quad (6\text{–}43)$$

We have now derived the basic boundary-layer equations for two-dimensional, laminar and turbulent, incompressible and compressible boundary-layer flow. We should note at this time that this is really only the starting point as far as boundary-layer solutions are concerned. These equations are only the basis for the many, many methods which presently exist for obtaining boundary-layer solutions under various circumstances.

SOLUTION OF BOUNDARY-LAYER EQUATIONS

After velocity profiles are discussed and the important boundary-layer parameters defined, some of the solution methods will be discussed. Included will be the flat-plate, incompressible solution, as well as compressible methods.

Velocity Profiles

One of the principal results obtained from most boundary-layer solutions is a description of the velocity profile in the boundary layer along the blade surface (fig. 6–7). The velocity profile describes mathematically

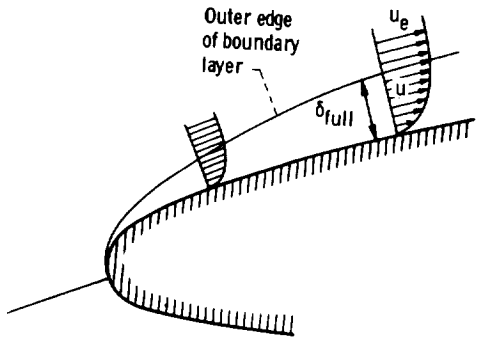

FIGURE 6–7.—Boundary-layer velocity profiles.

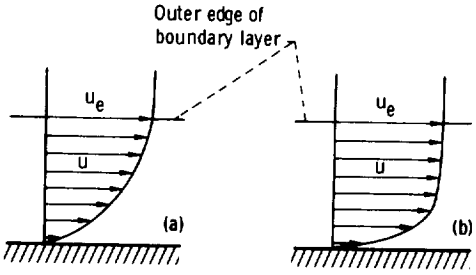

(a) Laminar profile. (b) Turbulent profile.

FIGURE 6–8.—Laminar and turbulent velocity profiles.

the dimensionless velocity u/u_e as a function of the dimensionless distance y/δ_{full} from the blade. The velocity u is the velocity in the boundary layer at a distance y from the surface, and the velocity u_e is the external free-stream velocity at a distance equal to the boundary-layer thickness, δ_{full}, from the surface. Alternately, δ_{full} is often defined as that distance from the blade where the velocity differs by 1 percent from the external velocity, u_e.

Velocity profiles for laminar flow (fig. 6–8(a)) tend to be parabolic in shape, while those for turbulent flow are blunted (fig. 6–8(b)). A commonly used mathematical expression for u/u_e in laminar flow is that originated by Pohlhausen (see ref. 1):

$$\frac{u}{u_e}=a\frac{y}{\delta_{full}}+b\left(\frac{y}{\delta_{full}}\right)^2+c\left(\frac{y}{\delta_{full}}\right)^3+d\left(\frac{y}{\delta_{full}}\right)^4 \tag{6–44}$$

The constants a, b, c, and d are defined in terms of a dimensionless shape parameter

$$\lambda=\frac{\delta_{full}^2}{\mu}\frac{du_e}{dx} \tag{6–45}$$

where

$$a=2+\frac{\lambda}{6} \tag{6–46a}$$

$$b=-\frac{\lambda}{2} \tag{6–46b}$$

$$c=-2+\frac{\lambda}{2} \tag{6–46c}$$

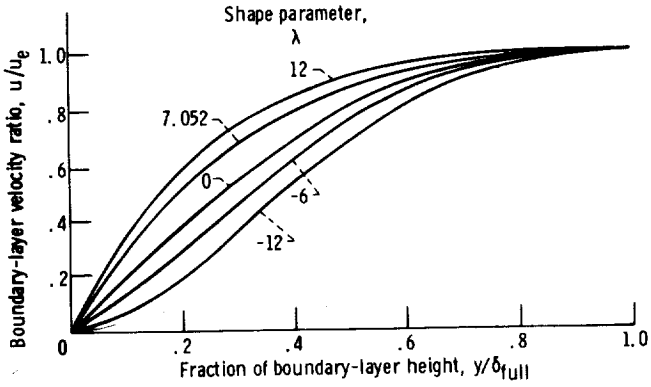

FIGURE 6–9.—Laminar velocity profiles.

$$d = 1 - \frac{\lambda}{6} \tag{6–46d}$$

Velocity profiles for various values of λ are shown in figure 6–9.

Velocity profiles for turbulent flow are often represented by the power law

$$\frac{u}{u_e} = \left(\frac{y}{\delta_{full}}\right)^{1/n} \tag{6–47}$$

Pipe-flow experiments show that the exponent n is a mild function of the Reynolds number and varies from 4 up to about 10. The value of $n = 7$ is most appropriate for boundary-layer flow on a flat plate. The exponent n can be related to other boundary-layer parameters, namely the displacement thickness δ and the momentum thickness θ, which are described in the next section.

Definitions of Important Boundary-Layer Parameters

Solutions of the two-dimensional boundary-layer equations are most often obtained in terms of three important parameters. These are the displacement thickness δ, the momentum thickness θ, and the form factor H. In order to define these parameters, it is necessary to first define the thickness of the boundary layer, δ_{full}. The definition of boundary-layer thickness is rather arbitrary, since transition from the velocity inside the boundary layer to that outside it takes place asymptotically. This is of little importance, however, because the velocity in the boundary layer attains a value which is very close to the external velocity at a small distance from the wall. It is possible to define the boundary-layer thick-

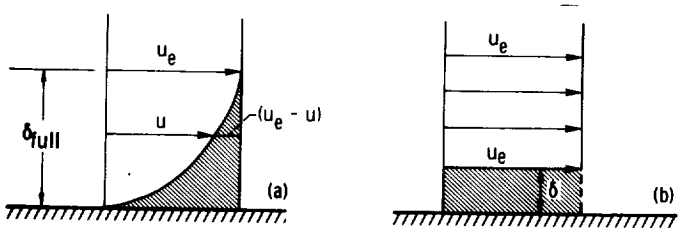

(a) Actual velocity profile. (b) Equivalent profile for equal mass flow.

FIGURE 6–10.—Displacement thickness of a boundary layer.

ness as that distance from the blade where the velocity differs by 1 percent from the external velocity u_e.

The displacement thickness δ, for compressible boundary-layer flow, can be defined with the help of figure 6–10. As seen from figure 6–10(a), the decrease in mass flow within the boundary layer due to the influence of friction is given by

$$\text{Mass defect} = \int_{y=0}^{y=\delta_{full}} (\rho_e u_e - \rho u)\, dy \tag{6–48}$$

where ρ_e is the density, in kg/m^3 or lbm/ft^3, in the free stream outside of the boundary layer. This integrated mass defect can be represented by a distance δ, the displacement thickness, as shown in figure 6–10(b). It is the distance by which the external potential field of flow is displaced outward as a consequence of the decrease in velocity in the boundary layer.

As figure 6–10 shows, the distance δ can be defined by the equation

$$\rho_e u_e \delta = \int_{y=0}^{y=\delta_{full}} (\rho_e u_e - \rho u)\, dy \tag{6–49}$$

Solving for δ gives

$$\delta = \frac{1}{\rho_e u_e} \int_{y=0}^{y=\delta_{full}} (\rho_e u_e - \rho u)\, dy = \int_{y=0}^{y=\delta_{full}} \left(1 - \frac{\rho u}{\rho_e u_e}\right) dy \tag{6–50}$$

The displacement thickness for incompressible flow reduces to

$$\delta = \frac{1}{u_e} \int_{y=0}^{y=\delta_{full}} (u_e - u)\, dy = \int_{y=0}^{y=\delta_{full}} \left(1 - \frac{u}{u_e}\right) dy \tag{6–51}$$

The loss of momentum in the boundary layer due to the presence of friction is given by

$$\text{Momentum defect} = \int_{y=0}^{y=\delta_{full}} \rho u(u_e - u)\, dy \tag{6–52}$$

This momentum defect from the momentum of purely potential flow can be represented by a distance θ, defined by the equation

$$\rho_e u_e^2 \theta = \int_{y=0}^{y=\delta_{full}} \rho u(u_e - u)\, dy \tag{6–53}$$

Solving for θ in this equation gives the definition of the momentum thickness for compressible boundary layers as

$$\theta = \frac{1}{\rho_e u_e^2} \int_{y=0}^{y=\delta_{full}} \rho u(u_e - u)\, dy = \int_{y=0}^{y=\delta_{full}} \frac{\rho u}{\rho_e u_e} \left(1 - \frac{u}{u_e}\right) dy \tag{6–54}$$

The momentum thickness for incompressible flow reduces to

$$\theta = \frac{1}{u_e^2} \int_{y=0}^{y=\delta_{full}} u(u_e - u)\, dy = \int_{y=0}^{y=\delta_{full}} \frac{u}{u_e} \left(1 - \frac{u}{u_e}\right) dy \tag{6–55}$$

The form factor H for both compressible and incompressible flow is defined as the ratio of displacement thickness to momentum thickness:

$$H = \frac{\delta}{\theta} \tag{6–56}$$

There are many other boundary-layer parameters besides δ, θ, and H for two-dimensional, and especially for three-dimensional, boundary layers. These three, however, are the principal parameters used in general boundary-layer studies.

Physical Interpretation of Separation

When separation of flow from a blade or a casing occurs, some of the retarded fluid in the boundary layer is transported away from the surface toward the main stream. When a region with an adverse pressure gradient exists along a surface, the retarded fluid particles cannot, in general, penetrate too far into the region of increased pressure because of their small kinetic energy. Thus, the boundary layer is deflected away from the surface and moves into the main stream. In general, the fluid particles behind the point of separation follow the pressure gradient and move in a direction opposite to the external stream. The point of separation is defined as the limit between forward and reverse flow in the layer in the immediate neighborhood of the wall. At separation,

$$\left(\frac{\partial u}{\partial y}\right)_{y=0} = 0 \tag{6–57}$$

Figure 6–11 illustrates separation occurring along a surface.

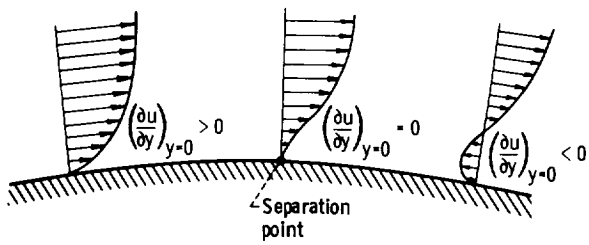

FIGURE 6–11.—Velocity gradients as flow undergoes separation.

By examining Prandtl's boundary-layer equations and considering the relation between pressure gradient dp/dx and velocity distribution $u(y)$, it is possible to infer that separation in a steady flow will occur only in the presence of an adverse pressure gradient (i.e., decelerated flow), $dp/dx>0$. From equation (6–23), with the boundary conditions at the surface being $u=v=0$, we have

$$\mu\left(\frac{\partial^2 u}{\partial y^2}\right)_{y=0} = g\frac{dp}{dx} \tag{6–58}$$

We can now relate velocity profiles to $\partial u/\partial y$, $\partial^2 u/\partial y^2$, and finally to dp/dx through equation (6–58). The equation indicates that in the immediate neighborhood of the wall, the curvature of the velocity profile, $\partial^2 u/\partial y^2$, depends only on the pressure gradient, dp/dx, and the curvature of the velocity profile at the wall changes its sign with the pressure gradient.

Figure 6–12(a) shows a velocity profile that would exist in a boundary layer subjected to a decreasing pressure. For such a profile, figure 6–12(b)

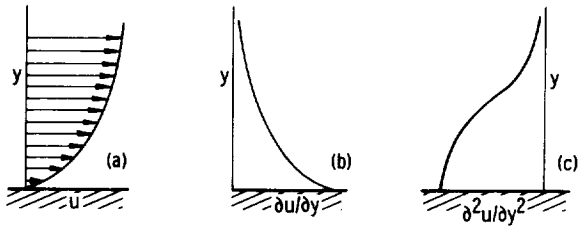

(a) Velocity profile.

(b) Velocity gradient.

(c) Velocity-profile curvature.

FIGURE 6–12.—Velocity distribution in a boundary layer with pressure decrease.

indicates that $\partial u/\partial y$ is positive for all y and decreases as y increases. Furthermore, figure 6–12(c) indicates that $\partial^2 u/\partial y^2$, which is the slope of $\partial u/\partial y$, is negative for all y. From equation (6–58), we know that negative $\partial^2 u/\partial y^2$ corresponds to negative dp/dx. Consequently, a boundary layer subjected to a decreasing pressure (negative dp/dx) will have velocity profiles which are not indicative of impending separation (the form of fig. 6–12(a)).

Figure 6–13(a) shows a profile which would exist in a boundary layer with decelerated flow due to an increasing pressure (adverse pressure gradient). Here, figure 6–13(b) indicates that $\partial u/\partial y$ has a positive slope near the blade surface; that is, $\partial^2 u/\partial y^2$ is positive (fig. 6–13(c)). This corresponds to positive dp/dx. However, since in all cases $\partial^2 u/\partial y^2$ must be less than zero at some distance from the surface, there must exist a point for which $\partial^2 u/\partial y^2 = 0$. This is a point of inflection of the boundary-layer velocity profile. It follows that in a region of retarded potential flow

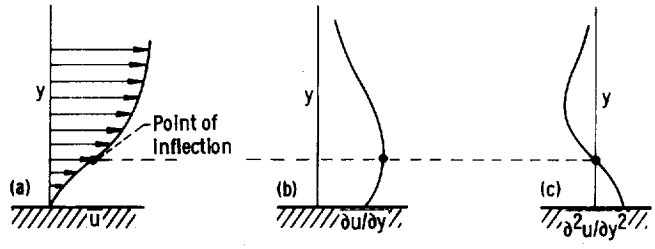

(a) Velocity profile. (b) Velocity gradient. (c) Velocity-profile curvature.

FIGURE 6–13.—Velocity distribution in a boundary layer with pressure increase.

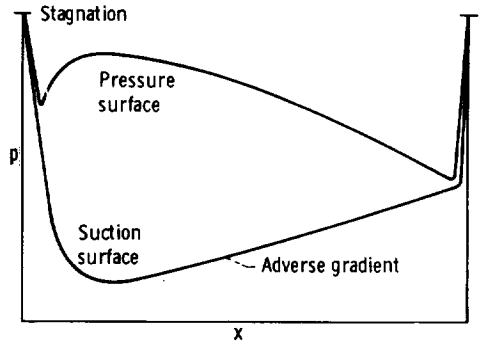

FIGURE 6–14.—Pressure distribution on a turbine blade.

(positive dp/dx), the velocity profile in the boundary layer will have a point of inflection. Since the velocity profile at the point of separation (with $\partial u/\partial y = 0$ at the surface) must have a point of inflection, it follows that, with the assumptions used in deriving equation (6–23), separation can occur only when the potential flow is retarded (i.e., in regions of adverse pressure gradient).

Figure 6–14 indicates a typical pressure distribution on the surface of a turbine blade. The danger zone, as far as separation is concerned, is readily seen to be the rear portion of the suction surface, where the major part of the blade diffusion is taking place.

Laminar Incompressible Boundary Layer on a Flat Plate

Prandtl's boundary-layer theory was first reported in 1904 in Germany. It was later translated and published in 1928 as an NACA Technical Memorandum (ref. 3). The first mathematical solution of Prandtl's equations to be published was the flat-plate solution of Blasius in 1908. This German work was also later translated by NACA (ref. 4).

On a flat plate with steady flow at zero incidence, the velocity from the potential solution is constant. Therefore, $p(x)$ is constant and $dp/dx = 0$. The boundary-layer equations, therefore, reduce to

$$u\frac{\partial u}{\partial x} + v\frac{\partial u}{\partial y} = \nu\frac{\partial^2 u}{\partial y^2} \tag{6–59}$$

where ν is the kinematic viscosity μ/ρ, in m^2/sec or ft^2/sec, and

$$\frac{\partial u}{\partial x} + \frac{\partial v}{\partial y} = 0 \tag{6–60}$$

The following are the boundary conditions:

$$\left.\begin{aligned} u = v = 0 \quad &\text{at} \quad y = 0 \\ u = u_e \quad &\text{at} \quad y = \infty \end{aligned}\right\} \tag{6–61}$$

With the use of a stream function ψ, Blasius transformed the partial differential equation (6–59) into the following ordinary differential equation:

$$f\frac{d^2 f}{dy^2} + 2\frac{d^3 f}{dy^3} = 0 \tag{6–62}$$

where f is a normalized stream function

$$f(\eta) = \frac{\psi}{\sqrt{\nu x u_e}} \tag{6–63}$$

which depends on the dimensionless y-coordinate, η, where

$$\eta = \frac{y}{\sqrt{\frac{\nu x}{u_e}}} \tag{6-64}$$

This equation has the following boundary conditions:

$$\left.\begin{aligned} f = \frac{df}{dy} = 0 \qquad & \text{at} \quad \eta = 0 \\ \frac{df}{dy} = 1 \qquad & \text{at} \quad \eta = \infty \end{aligned}\right\} \tag{6-65}$$

Equation (6–62) cannot be solved exactly. Blasius obtained an approximate solution in the form of a power series expansion about $\eta = 0$ and an asymptotic expansion for $\eta = \infty$, the two solutions being joined at a suitable point. More recently, Howarth (ref. 5) solved the Blasius equation (6–62) with a high degree of accuracy, and provided tabular values for f, df/dy, and d^2f/dy^2 as functions of η. Since $df/dy = u/u_e$, the solution gives the velocity profile of figure 6–15. This profile possesses a very small curvature at the wall and turns rather abruptly further from it in order

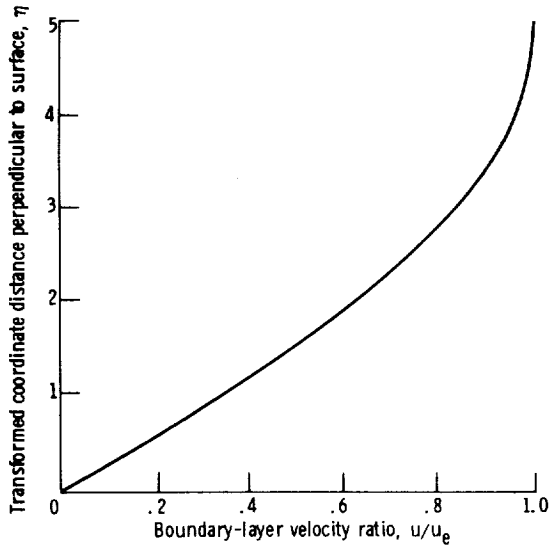

FIGURE 6–15.—Blasius-Howarth velocity profile for flow on a flat plate.

to reach the asymptotic value. At the wall itself, the curve has a point of inflection, since for $y=0$, $\partial^2 u/\partial y^2 = 0$.

From the order-of-magnitude analysis performed to obtain Prandtl's boundary-layer equations, we had the relation

$$\epsilon^2 \approx \delta_{full}^2 \approx \frac{1}{Re} \tag{6–66}$$

For a semi-infinite flat plate, the Reynolds number can be expressed as

$$Re_x = \frac{u_e x}{\nu} \tag{6–67}$$

In order to make equation (6–66) dimensionally correct, we can say

$$\frac{\delta_{full}^2}{x^2} \propto \frac{1}{Re_x} \tag{6–68}$$

or

$$\delta_{full} \propto \sqrt{\frac{\nu x}{u_e}} \tag{6–69}$$

The constant of proportionality can be obtained from Howarth's numerical solution and is equal to 5. So, for a semi-infinite flat plate at zero incidence in laminar flow, we obtain the useful relation for the boundary-layer thickness

$$\delta_{full} = 5.0 \sqrt{\frac{\nu x}{u_e}} \tag{6–70}$$

With the use of Howarth's solution to the Blasius equations, the following relations for other important boundary-layer parameters for laminar flow on a flat plate can also be obtained:

$$\delta = 1.72 \sqrt{\frac{\nu x}{u_e}} \tag{6–71}$$

$$\theta = 0.664 \sqrt{\frac{\nu x}{u_e}} \tag{6–72}$$

$$\frac{g\tau_w}{\rho u_e^2} = 0.332 \sqrt{\frac{\nu}{u_e x}} = \frac{0.332}{\sqrt{Re_x}} \tag{6–73}$$

$$D = \frac{1.328}{g} b \sqrt{\mu \rho l u_e^3} \tag{6–74}$$

$$C_f = 1.328\sqrt{\frac{\nu}{u_e l}} = \frac{1.328}{\sqrt{Re_l}} \tag{6–75}$$

where

τ_w	shear stress on the surface, N/m²; lbf/ft²
D	total drag on both sides of flat plate, N; lbf
b	width of flat plate, m; ft
l	length of flat plate, m; ft
C_f	dimensionless drag or skin friction coefficient for flat plate
Re_l	Reynolds number based on plate length l

It should be noted that all of these relations are valid only for laminar flow; that is, they are valid only where $Re_l < 10^6$, a value that is indicative of laminar flow over the entire length of the plate. For $Re_l > 10^6$, transition to turbulent boundary layer will probably occur, and the expressions in equations (6–71) to (6–75) will be valid only from the leading edge of the plate to the transition point. If transition to turbulent boundary layer does occur, then the drag will be larger than that calculated by equation (6–74).

Integral Methods for Solving the Laminar-Boundary-Layer Equations

The two principal means of solving the laminar-boundary-layer equations are by integral methods and by finite-difference methods. Both means provide approximate solutions, since exact solutions are extremely cumbersome.

Integral methods are based on von Kármán's momentum integral formula. Von Kármán's original work was published in 1912 in Germany and was later translated by NACA (ref. 6). Von Kármán realized that it was not necessary to satisfy the boundary-layer equations for every fluid particle. Instead, he satisfied the boundary-layer equations close to the wall and in the region where external flow is approached by satisfying the boundary conditions. In the remaining region of fluid in the boundary layer, only a mean over the differential equation is satisfied. Such a mean is obtained from the momentum equation (eq. (6–23) or (6–30)) by integration over the boundary-layer thickness. If equations (6–23) and (6–30) are integrated from $y = 0$ to $y = \delta_{full}$, and if the definitions of displacement thickness (eq. (6–50)) and momentum thickness (eq. (6–54)) are introduced, the following equations result. For laminar, incompressible flow,

$$u_e^2 \frac{d\theta}{dx} + (2\theta + \delta) u_e \frac{du_e}{dx} = \frac{g\tau_w}{\rho} \tag{6–76}$$

For laminar, compressible flow,

$$u_e^2 \frac{d\theta}{dx} + (2\theta + \delta - M_e^2\theta) u_e \frac{du_e}{dx} = \frac{g\tau_w}{\rho_e} \tag{6–77}$$

where the subscript e denotes conditions at the outer edge of the boundary layer.

Equation (6–76) or (6–77) leads to an ordinary differential equation for the boundary-layer thickness, provided that a suitable form is assumed for the velocity profile, u/u_e. This allows us to calculate the displacement thickness, δ, the momentum thickness, θ, and the shearing stress at the wall, τ_w. Pohlhausen was the first to use equation (6–76) to obtain a solution for incompressible boundary layers. His work was published in 1921 (refs. 7 and 1). The velocity profile assumed by Pohlhausen was discussed earlier in this chapter, under "Velocity Profiles." Although Pohlhausen's solution is probably the simplest, it is known to give poor results in regions of rising pressure. As a result, various authors have tried to improve and extend his method by assuming different families of velocity distributions.

A famous work among those which followed Pohlhausen's was that of Thwaites (ref. 8). Thwaites collected and compared all known velocity distributions from exact and approximate solutions for laminar incompressible flow. Thwaites' method does not require the solution of ordinary differential equations. He relates the wall shear, its derivative at the wall, and the form factor to one another without specifying a type of velocity profile. To do this, nondimensional forms of these quantities were defined and evaluated with the use of exact solutions for the laminar boundary layer. It developed that a nearly universal relation existed among these quantities for favorable pressure gradients. For adverse gradients, Thwaites selected a single representative relation. A unique correlation was chosen that reduced the solution of an incompressible problem to the evaluation of a single integral. Thwaites' method was extended to compressible fluids by Rott and Crabtree (ref. 9). They recognized that when heat transfer is negligible, and the Prandtl number is equal to 1, a transformation proposed by Stewartson (ref. 10) could be used to relate compressible to incompressible boundary-layer solutions.

One of the best integral methods to appear to date for the solution of laminar boundary layers is that of Cohen and Reshotko (refs. 11 and 12). Their method applies to compressible or incompressible flow over two-dimensional or axially symmetric surfaces. It handles arbitrary free-stream pressure distribution and performs well in areas of adverse pressure gradient. A surface temperature level may be specified, and heat transfer is calculated. Cohen and Reshotko's method is based on Thwaites' correlation concept. Stewartson's transformation (ref. 10) is first applied

to Prandtl's equations. The resulting nonlinear, first-order differential equations are expressed in terms of dimensionless parameters related to the wall shear, the surface heat transfer, and the transformed free-stream velocity. Then Thwaites' concept of a unique interdependence of these parameters is assumed. The evaluation of these quantities is then carried out by utilizing the exact solutions of reference 11. With the resulting relations, methods are derived for the calculation of all the important boundary-layer parameters. In 1960, Luxton and Young published a method (ref. 13) which is as general as Cohen and Reshotko's, but which allows the Prandtl number to have values slightly different from 1.

Finite-Difference Methods for Solving the Laminar-Boundary-Layer Equations

Finite-difference methods for solving the boundary-layer equations have recently come into prominence because of the development of digital computers. Smith and Clutter have done a considerable amount of work in developing this technique (refs. 14 and 15). Another recent reference of interest is that of Krause (ref. 16). These methods give very good results with relatively short running times on the computer.

Eddy-Viscosity and Mixing-Length Concepts in Turbulent Boundary-Layer Flow

Before referencing any of the current methods for solving turbulent boundary-layer flow, the concepts of "eddy viscosity" and "mixing length" should be discussed. These approximation concepts have been used in many of the methods developed to date to relate the Reynolds stresses produced by the mixing motion to the mean values of velocity components. By this means, the Reynolds stresses are given a mathematical form which, upon substitution into the governing equations, leads to differential equations containing only mean values of density, velocity, and pressure. These transformed differential equations constitute the starting point for the calculation of the mean boundary-layer flow.

Boussinesq first worked on this problem in 1877. In analogy with the coefficient of viscosity in Stokes' law for laminar flow

$$\tau_l = \frac{\mu}{g}\frac{\partial u}{\partial y} \tag{6–78}$$

where τ_l is the laminar shear stress, in N/m^2 or lbf/ft^2, he introduced a mixing coefficient, A_τ, for the Reynolds stress in turbulent flow by putting

$$\tau_t = \frac{A_\tau}{g}\frac{\partial \bar{u}}{\partial y} \tag{6–79}$$

where τ_t is the turbulent shear stress, in N/m^2 or lbf/ft^2. In 1880, Reynolds introduced the concept of eddy, or virtual, viscosity, ϵ, where

$$\epsilon = \frac{A_\tau}{\rho} \tag{6–80}$$

Thus, the eddy viscosity is analogous to the kinematic viscosity $\nu = \mu/\rho$. Turbulent stress can then be expressed as

$$\tau_t = \frac{\rho}{g} \epsilon \frac{\partial \bar{u}}{\partial y} = \frac{-\rho}{g} \overline{u'v'} \tag{6–81}$$

With the use of this concept, terms in equations (6–37) and (6–40) such as

$$\frac{\partial}{\partial y}\left(\mu \frac{\partial \bar{u}}{\partial y} - \bar{\rho}\overline{u'v'}\right)$$

can be written as

$$\frac{\partial}{\partial y}\left[(\mu + A_\tau) \frac{\partial \bar{u}}{\partial y}\right]$$

A similar concept can be applied to the energy equation where an eddy, or a virtual, conductivity can be defined. The difficulty with applying the eddy-viscosity method is that A_τ and hence ϵ depend on velocity. It is, therefore, necessary to find empirical relations between these coefficients and the mean velocity.

In 1925, Prandtl introduced a completely different approximation for the Reynolds stresses. His argument is called Prandtl's mixing-length hypothesis, since the mixing length is somewhat analogous to the mean free path in the kinetic theory of gases. The main difference is that kinetic theory concerns itself with the microscopic motion of particles, whereas Prandtl's concept deals with the macroscopic motion of large clusters of fluid particles. Deriving Prandtl's expression for shear stress requires a good deal of discussion of his physical model of turbulent flow, all of which is contained in reference 1. His final expression is

$$\tau_t = \frac{\rho}{g} l^2 \left|\frac{d\bar{u}}{dy}\right| \frac{d\bar{u}}{dy} = -\frac{\rho}{g} \overline{u'v'} \tag{6–82}$$

where l is the mixing length, in m or ft.

On comparing Prandtl's expression (eq. (6–82)) with that of Boussinesq (eq. (6–81)), it appears that little has been gained. The unknown eddy viscosity ϵ of the first expression has merely been replaced by the unknown mixing length l of the second expression. However, Prandtl's equation (6–82) is generally more suitable for the calculation of turbulent motion than is equation (6–81). Turbulent drag is roughly proportional to the

square of velocity, and the same result is obtained from (6–82) if the mixing length is assumed to be independent of the magnitude of velocity. So, mixing length is a purely local function, although we cannot say it is a property of the fluid. It is far simpler to make assumptions about the mixing length l than about the eddy viscosity ϵ, and this constitutes the superiority of Prandtl's expression over that of Boussinesq.

Integral Methods for Solving the Turbulent Boundary-Layer Equations

Just as with the laminar-boundary-layer equations, there are both integral methods and finite-difference methods for solving the turbulent boundary-layer equations. Both of these provide approximate solutions, since exact solutions for turbulent flow are now impossible.

Gruschwitz was the first to propose a method for solving the equations for an incompressible turbulent boundary layer. His work was published in Germany in 1931. A rash of works followed, most of them making improvements to the calculational technique and empirical data used by Gruschwitz. Ludwieg and Tillmann, whose work was published in Germany in 1949 and was translated by NACA in 1950 (ref. 17), proposed an empirical relation for the skin-friction term in the momentum integral equation. This relation is still used in many current methods. Stewartson's transformations (ref. 10) are likewise used in many methods for solving the turbulent-boundary-layer equations.

Maskell, in 1951 (ref. 18), proposed an improved method for incompressible turbulent boundary layers. He replaced the momentum equation by an empirically determined approximation which is directly integrable and thus determines the momentum thickness. A profile parameter is obtained from an empirical auxiliary differential equation. The Ludwieg-Tillmann skin-friction formula is used to calculate the skin-friction distribution and to determine a separation point for flows with adverse pressure gradient.

Truckenbrodt, whose work was published in Germany in 1952 and was translated by NACA in 1955 (ref. 19), proposed solutions for both laminar and turbulent incompressible boundary-layer flows. The method is simple and, like Maskell's method, does not use the momentum integral equation. It applies to both two-dimensional and rotationally symmetrical flows. Because of its simplicity and relatively accurate results, Truckenbrodt's method is still used for incompressible turbulent boundary layers.

Compressible turbulent boundary layers were first treated adequately with the use of integral methods by Reshotko and Tucker in 1957 (ref. 20). Prior to their work, the Kármán momentum integral equation had been utilized with an assumed boundary-layer velocity profile, usually the power law, and one of several empirical skin-friction relations. When

pressure gradient was present, an auxiliary equation, usually the moment-of-momentum equation, was used. (This equation is obtained by multiplying the integrand of the momentum integral equation by a distance normal to the surface and then integrating with respect to that distance.) The momentum integral equation and the auxiliary equation were then solved simultaneously.

Reshotko and Tucker's method, applicable to compressible flow with heat transfer and pressure gradient, also uses the momentum and moment-of-momentum integral equations. These are expressed in incompressible form and are uncoupled with the use of Stewartson's transformation (ref. 10) and the results of Maskell (ref. 18). The Ludwieg-Tillmann skin-friction relation is used in a form suitable for compressible flow with heat transfer through application of Eckert's reference-enthalpy concept (ref. 21). An approximation for the shear-stress distribution through the boundary layer and the power-law velocity profile are used to simplify the moment-of-momentum equation. Separation is located as the point where the skin friction, when extrapolated, becomes zero. This method, until several years ago, was the best available for compressible turbulent boundary layers. It is still widely used in many computer programs today.

One of the best integral methods available today for compressible turbulent boundary layers is that of Sasman and Cresci (ref. 22). It is simply an extension of the Reshotko-Tucker method. It uses somewhat the same analysis, but no attempt is made to uncouple the momentum and moment-of-momentum integral equations. These equations are solved simultaneously after introduction of boundary-layer shear-stress distributions obtained from recent numerical results of equilibrium turbulent boundary-layer analysis. The Sasman-Cresci analysis is better than that of Reshotko-Tucker at predicting separation in regions of adverse pressure gradient. McNally (ref. 23) has developed a computer program based on the Cohen-Reshotko (refs. 11 and 12) and Sasman-Cresci (ref. 22) techniques. An additional source of information on compressible turbulent boundary-layer analysis is the work of Herring and Mellor (ref. 24).

Finite-Difference Methods for Solving the Turbulent Boundary-Layer Equations

Finite-difference methods for solving the turbulent boundary-layer equations have recently begun to appear. Cebeci and Smith have done a large portion of this work to date (refs. 25, 26, and 27). Bradshaw, Ferriss, and Atwell have also developed methods for the turbulent boundary layer (refs. 28 and 29) based on the use of the turbulent energy equation. Patankar and Spalding have developed still another method for handling the turbulent boundary-layer equations (refs. 30 and 31). A great deal of work is going on in this field at the present time, and no method is yet

clearly superior to any of the others. Two relatively recent publications (refs. 32 and 33) compare many of the most prominent methods, both integral and finite difference, for solving the turbulent boundary layer.

CONCLUDING REMARKS

The selection of a method of solution suitable to a particular boundary-layer problem requires some familiarity with the various methods available. This can be achieved by studying some of the more recent references that have been mentioned herein. The present discussion of the methods of solution has been intended to show the historical development of solution techniques, the variety of methods available, and the complexity of the whole boundary-layer problem, especially where turbulent flows are involved.

REFERENCES

1. SCHLICHTING, HERMANN (J. KESTIN, TRANS.): Boundary Layer Theory. McGraw-Hill Book Co., Inc., any edition.
2. BIRD, R. BYRON; STEWART, WARREN E.; AND LIGHTFOOT, EDWIN N.: Transport Phenomena. John Wiley & Sons, Inc., 1960.
3. PRANDTL, L.: Motion of Fluids with Very Little Viscosity. NACA TM 452, 1928.
4. BLASIUS, H.: The Boundary Layers in Fluids with Little Friction. NACA TM 1256, 1950.
5. HOWARTH, L.: On the Solution of the Laminar Boundary Layer Equations. Proc. Roy. Soc. (London), Ser. A, vol. 164, no. 919, Feb. 18, 1938, pp. 547–579.
6. VON KÁRMÁN, TH: On Laminar and Turbulent Friction. NACA TM 1092, 1946.
7. POHLHAUSEN, K.: Approximate Integration of the Differential Equation of the Limit Surface of Laminar Motion. Zeit. f. Math. Mech., vol. 1, Aug. 1921, pp. 252–268.
8. THWAITES, B.: Approximate Calculation of the Laminar Boundary Layer. Aeronaut. Quart., vol. 1, Nov. 1949, pp. 245–280.
9. ROTT, NICHOLAS; AND CRABTREE, L. F.: Simplified Laminar Boundary-Layer Calculations for Bodies of Revolution and for Yawed Wings. J. Aeron. Sci., vol. 19, no. 8, Aug. 1952, pp. 553–565.
10. STEWARTSON, K.: Correlated Incompressible and Compressible Boundary Layers. Proc. Roy. Soc. (London), Ser. A, vol. 200, no. 1060, Dec. 22, 1949, pp. 84–100.
11. COHEN, CLARENCE B.; AND RESHOTKO, ELI: Similar Solutions for the Compressible Laminar Boundary Layer with Heat Transfer and Pressure Gradient. NACA TR 1293, 1956.
12. COHEN, CLARENCE B.; AND RESHOTKO, ELI: The Compressible Laminar Boundary Layer with Heat Transfer and Arbitrary Pressure Gradient. NACA TR 1294, 1956.
13. LUXTON, R. E.; AND YOUNG, A. D.: Generalized Methods for the Calculation of the Laminar Compressible Boundary-Layer Characteristics with Heat Transfer and Non-Uniform Pressure Distribution. R&M–3233, Aeronautical Research Council, Gt. Britain, 1962.

14. SMITH, A. M. O.; AND CLUTTER, DARWIN W.: Solution of the Incompressible Laminar Boundary-Layer Equations. AIAA J., vol. 1, no. 9, Sept. 1963, pp. 2062–2071.
15. SMITH, A. M. O.; AND CLUTTER, DARWIN W.: Machine Calculation of Compressible Laminar Boundary Layers. AIAA J., vol. 3, no. 4, Apr. 1965, pp. 639–647.
16. KRAUSE, EGON: Numerical Solution of the Boundary-Layer Equations. AIAA J., vol. 5, no. 7, July 1967, pp. 1231–1237.
17. LUDWIEG, HUBERT; AND TILLMANN, W.: Investigations of the Wall-Shearing Stress in Turbulent Boundary Layers. NACA TM 1285, 1950.
18. MASKELL, E. C.: Approximate Calculation of the Turbulent Boundary Layer in Two-Dimensional Incompressible Flow. Rep. AERO 2443, Royal Aircraft Establishment, Nov. 1951.
19. TRUCKENBRODT, E.: A Method of Quadrature for Calculation of the Laminar and Turbulent Boundary Layer in Case of Plane and Rotationally Symmetrical Flow. NACA TM 1379, 1955.
20. RESHOTKO, ELI; AND TUCKER, MAURICE: Approximate Calculation of the Compressible Turbulent Boundary Layer with Heat Transfer and Arbitrary Pressure Gradient. NACA TN 4154, 1957.
21. ECKERT, E. R. G.: Engineering Relations for Friction and Heat Transfer to Surfaces in High Velocity Flow. J. Aeron. Sci., vol. 22, no. 8, Aug. 1955, pp. 585–587.
22. SASMAN, PHILIP K.; AND CRESCI, ROBERT J.: Compressible Turbulent Boundary Layer with Pressure Gradient and Heat Transfer. AIAA J., vol. 4, no. 1, Jan. 1966, pp. 19–25.
23. MCNALLY, WILLIAM D.: FORTRAN Program for Calculating Compressible Laminar and Turbulent Boundary Layers in Arbitrary Pressure Gradients. NASA TN D–5681, 1970.
24. HERRING, H. JAMES; AND MELLOR, G. L.: A Method of Calculating Compressible Turbulent Boundary Layers. NASA CR–1144, 1968.
25. CEBECI, T.; SMITH, A. M. O.; AND MOSINSKIS, G.: Solution of the Incompressible Turbulent Boundary-Layer Equations with Heat Transfer. J. Heat Transfer, vol. 92, no. 1, Feb. 1970, pp. 133–143.
26. SMITH, A. M. O.; AND CEBECI, T.: Numerical Solution of the Turbulent-Boundary-Layer Equations. Rep. DAC–33735, Douglas Aircraft Co. (AD–656430), May 1967.
27. CEBECI, T.; AND SMITH, A. M. O.: A Finite-Difference Method for Calculating Compressible Laminar and Turbulent Boundary Layers. J. Basic Eng., vol. 92, no. 3, Sept. 1970, pp. 523–535.
28. BRADSHAW, P.; FERRISS, D. H.; AND ATWELL, N. P.: Calculation of Boundary-Layer Development Using the Turbulent Energy Equation. J. Fluid Mech., vol. 28, pt. 3, May 26, 1967, pp. 593–616.
29. BRADSHAW, P.: Calculation of Boundary-Layer Development Using the Turbulent Energy Equation. IX: Summary. Rep. NPL–Aero–1287, National Physical Lab., Jan. 30, 1969.
30. PATANKAR, S. V.; AND SPALDING, D. B.: A Finite-Difference Procedure for Solving the Equations of the Two-Dimensional Boundary Layer. Int. J. Heat Mass Transfer, vol. 10, no. 10, Oct. 1967, pp. 1389–1411.
31. PATANKAR, S. V.; AND SPALDING, D. B.: Heat and Mass Transfer in Boundary Layers. C.R.C. Press, 1967.
32. COLES, D. E.; AND HIRST, E. A., EDS.: Proceedings, Computation of Turbulent Boundary Layers—1968, AFOSR–IFP–Stanford Conference. Stanford Univ. Press, 1969.

33. BERTRAM, MITCHEL H., ED.: Compressible Turbulent Boundary Layers. NASA SP–216, 1969.

SYMBOLS

A_τ	turbulent flow mixing coefficient, (N)(sec)/m²; lbm/(ft)(sec)
a	constant in eq. (6–44)
b	width of flat plate, m; ft constant in eq. (6–44)
C_f	skin-friction coefficient for a flat plate
c	constant in eq. (6–44)
c_p	specific heat at constant pressure, J/(kg)(K); Btu/(lbm)(°R)
D	total drag on flat plate, N; lbf
d	constant in eq. (6–44)
f	Blasius dimensionless stream function defined by eq. (6–63)
$\mathbf{f}$	general body force vector, N/kg; lbf/lbm
f_x	component of body force $\mathbf{f}$ in x-direction, N/kg; lbf/lbm
f_y	component of body force $\mathbf{f}$ in y-direction, N/kg; lbf/lbm
f_z	component of body force $\mathbf{f}$ in z-direction, N/kg; lbf/lbm
g	conversion constant, 1; 32.17 (lbm)(ft)/(lbf)(sec²)
H	form factor, defined by eq. (6–56)
$\mathbf{i}$	unit vector in the x-direction
J	conversion constant, 1; 778 (ft)(lbf)/Btu
$\mathbf{j}$	unit vector in the y-direction
k	thermal conductivity, W/(m)(K); Btu/(sec)(ft)(°R)
$\mathbf{k}$	unit vector in the z-direction
L	characteristic length (e.g., the blade chord), m; ft
l	Prandtl mixing length, m; ft length of flat plate, m; ft
M_e	Mach number external to the boundary layer
n	exponent on the turbulent velocity profile, eq. (6–47)
P	dimensionless pressure, defined by eq. (6–13e)
p	static pressure, N/m²; lbf/ft²
R	gas constant, J/(kg)(K); (ft)(lbf)/(lbm)(°R)
Re	Reynolds number based on L and U_0, as defined by eq. (6–13f)
Re_l	Reynolds number based on l, as defined in eq. (6–75)
Re_x	Reynolds number based on x, as defined by eq. (6–67)
r	radius of curvature of blade surface, m; ft
S	constant in eq. (6–25), K; °R
T	absolute static temperature, K; °R
T_t	absolute total temperature, K; °R
T_0	reference temperature used in eq. (6–25), K; °R
t	time, sec
U	dimensionless velocity in x-direction, defined by eq. (6–13c)
U_0	free-stream velocity upstream of blade, m/sec; ft/sec
u	component of general velocity vector $\mathbf{u}$ in the x-direction, m/sec; ft/sec

$\mathbf{u}$	general velocity vector, m/sec; ft/sec
u_e	free-stream velocity at the outer edge of the boundary layer, m/sec; ft/sec
V	dimensionless velocity in y-direction, defined by eq. (6–13d)
v	component of general velocity vector $\mathbf{u}$ in the y-direction, m/sec; ft/sec
w	component of general velocity vector $\mathbf{u}$ in the z-direction, m/sec; ft/sec
X	dimensionless x-coordinate, defined by eq. (6–13a)
x	x-coordinate, m; ft coordinate parallel to boundary surface, m; ft
Y	dimensionless y-coordinate, defined by eq. (6–13b)
y	y-coordinate, m; ft coordinate perpendicular to boundary surface, m; ft
z	z-coordinate, m; ft
δ	displacement thickness, m; ft
δ_{full}	boundary-layer thickness, m; ft
ϵ	eddy viscosity defined by eq. (6–80), m²/sec; ft²/sec a dimensionless quantity much less than 1
η	Blasius transformed y-coordinate defined by eq. (6–64)
θ	momentum thickness, m; ft
λ	dimensionless shape parameter defined by eq. (6–45)
μ	dynamic viscosity, (N)(sec)/m²; lbm/(ft)(sec)
μ_0	dynamic viscosity at reference temperature T_0, (N)(sec)/m²; lbm/(ft)(sec)
ν	kinematic viscosity, m²/sec; ft²/sec
ρ	density, kg/m³; lbm/ft³
ρ_e	free-stream density external to the boundary layer, kg/m³; lbm/ft³
τ_l	laminar shear stress, N/m²; lbf/ft²
τ_t	turbulent shear stress, N/m²; lbf/ft²
τ_w	shear stress at the wall, N/m²; lbf/ft²
φ	function defined by eq. (6–34)
ψ	Blasius stream function, m²/sec; ft²/sec
ω	constant in eq. (6–26)

Superscripts:

$\bar{}$	time average
$'$	fluctuating component

CHAPTER 7

Boundary-Layer Losses

By Herman W. Prust, Jr.

The primary cause of losses in a turbine is the boundary layer that builds up on the blade and end-wall surfaces. In particular, these losses are the friction loss resulting from the flow of the viscous fluid over the surfaces, the pressure-drag loss resulting from the flow of fluid past the blade trailing edge, and the loss downstream of the blades resulting from the mixing of the low-velocity boundary-layer fluid with the high-velocity free-stream fluid. Chapter 6 presented an introduction to boundary-layer theory, by means of which the surface boundary-layer buildup can be analytically described. This chapter covers analytical and experimental methods for determining the friction, trailing-edge, and mixing losses associated with the boundary layer. The theory presented herein refers primarily to two-dimensional blade-section boundary layers. Methods for obtaining three-dimensional blade plus end-wall losses from the two-dimensional results are also discussed.

A fundamental objective in blade-row design is to minimize the energy loss resulting from the flow of fluid through the blade row. Therefore, the final expressions for loss developed in this chapter are in terms of kinetic-energy loss coefficients. These coefficients express the loss in fluid kinetic energy as a fractional part of the ideal kinetic energy of the actual flow through the blade row. Efficiency based on kinetic energy can be obtained by subtracting these coefficients from unity, and this is consistent with the blade-row efficiency definition used in chapter 2.

Before proceeding with the discussion of boundary-layer parameters and loss coefficients, the blade-row station locations and associated pressure and velocity distributions will be introduced with the aid of figure 7–1. These pressure and velocity distributions and the associated dis-

cussion refer to an attached boundary layer only. A separated boundary layer, with its associated reversal of flow at the surface, is thicker, yields a higher loss, and cannot be analyzed in the same manner, if at all.

Figure 7–1(a) indicates the four station locations that will be referred

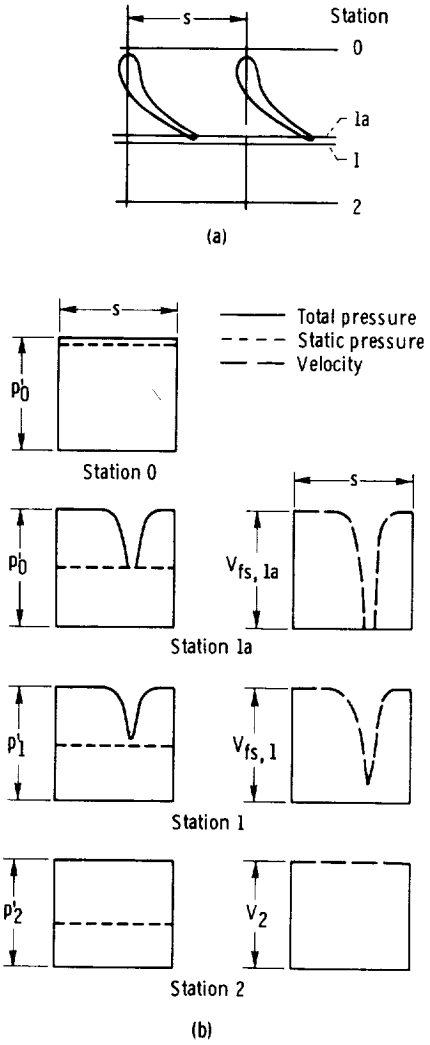

(a) Station locations.
(b) Pressure and velocity distributions.

FIGURE 7–1.—Station locations and associated pressure and velocity distributions.

to in this chapter. Station 0 represents the inlet to the blade row. At this station, a uniform total pressure p_0' is assumed, as indicated in figure 7–1(b). Station $1a$ is just within the trailing edge of the blade. The boundary layers developed on the blade surfaces result in velocity and pressure profiles as shown in figure 7–1(b). Velocity varies from the free-stream value $V_{fs,1a}$ to zero at the blade surfaces. There is, of course, no flow through the region of the solid trailing edge. Total pressure varies from the free-stream value $p'_{fs,1a}=p_0'$ to the static pressure p_{1a} at the blade surfaces. This static pressure is assumed constant across station $1a$, as is the flow angle α_{1a}. At station $1a$, only the surface friction loss has occurred.

Station 1 is just beyond the blade trailing edge, where the boundary-layer fluid has filled the void, but where little mixing with the free stream has occurred. This is indicated in figure 1(b) by the station-1 profiles showing flow throughout the entire wake region. Here too, static pressure and flow angle are assumed constant across the station. Between stations $1a$ and 1, the trailing-edge loss occurs. Station 2 is located at a distance sufficiently downstream of the blade row that complete mixing, with the associated mixing loss, has taken place. The velocity and total-pressure profiles are again uniform.

In order to simplify analysis and discussion, a number of variables have been assumed constant across the various stations. Uniformity of inlet conditions is a universal convenience that usually can be approached in component tests but seldom exists in actual applications. Experiments have shown that static pressure and flow angle do vary somewhat across both free stream and boundary layer at stations $1a$ and 1. In some instances, which will be later identified, this variation can be accounted for. Although some downstream mixing of the flow does take place, a completely uniform downstream state is merely a hypothetical convenience.

BOUNDARY-LAYER PARAMETERS

When a real fluid flows over a surface, a loss results due to both friction between the fluid and the surface and friction between the layers of fluid in the region adjacent to the surface. As shown by figure 7–2, the fluid velocity in the boundary-layer region varies from zero velocity on the surface to free-stream velocity V_{fs} at the full boundary-layer height δ_{full}. To describe the losses in flow, momentum, and energy resulting from the presence of the boundary layer, certain parameters are used. Some of these (displacement thickness, momentum thickness, form factor) were introduced in the last chapter and will be reviewed here; in addition, others specifically used for obtaining the desired kinetic-energy coefficients will be introduced and defined.

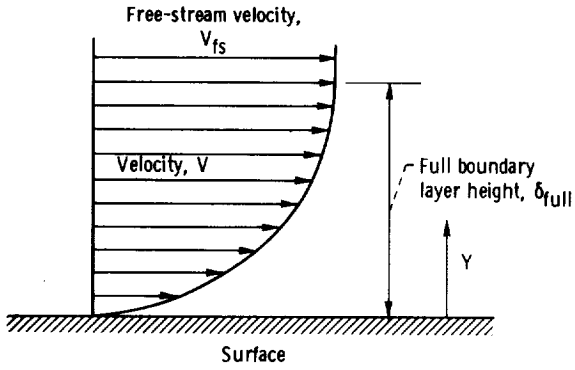

FIGURE 7–2.—Typical boundary-layer velocity profile.

The displacement thickness δ, which is indicative of the loss in mass flow, is defined by

$$\delta(\rho V)_{fs} = \int_0^{\delta_{full}} (\rho V)_{fs}\, dY - \int_0^{\delta_{full}} (\rho V)\, dY \qquad (7\text{–}1)$$

where

δ	displacement thickness, m; ft
δ_{full}	boundary-layer thickness, m; ft
V	fluid velocity, m/sec; ft/sec
ρ	fluid density, kg/m^3; lb/ft^3
Y	distance in direction normal to boundary layer, m; ft
$( )_{fs}$	free-stream (ideal) conditions

Equation (7–1) states that the loss in mass flow of the fluid in the boundary layer is equal to the ideal flow which would pass through a length (or an area) equal to the displacement thickness. Solving for δ yields

$$\delta = \int_0^{\delta_{full}} dY - \int_0^{\delta_{full}} \frac{\rho V}{(\rho V)_{fs}}\, dY \qquad (7\text{–}2)$$

The momentum thickness θ, which is indicative of the momentum loss, is defined by

$$\theta(\rho V^2)_{fs} = \int_0^{\delta_{full}} (\rho V V_{fs})\, dY - \int_0^{\delta_{full}} \rho V^2\, dY \qquad (7\text{–}3)$$

where θ is the momentum thickness, in m or ft. Equation (7–3) states that the loss in momentum of the fluid in the boundary layer is equal to the

ideal momentum of the ideal flow which would pass through a length (or an area) equal to the momentum thickness. Solving for θ yields

$$\theta = \int_0^{\delta_{full}} \frac{\rho V}{(\rho V)_{fs}} dY - \int_0^{\delta_{full}} \frac{\rho V^2}{(\rho V^2)_{fs}} dY \tag{7-4}$$

The loss in kinetic energy can be similarly expressed in terms of an energy thickness defined by

$$\frac{1}{2}\psi(\rho V^3)_{fs} = \frac{1}{2}\int_0^{\delta_{full}} (\rho V V_{fs}^2)\, dY - \frac{1}{2}\int_0^{\delta_{full}} (\rho V^3)\, dY \tag{7-5}$$

where ψ is the energy thickness, in m or ft. Equation (7–5) states that the loss in kinetic energy of the fluid in the boundary layer is equal to the ideal kinetic energy of the ideal flow which would pass through a length (or an area) equal to the energy thickness. Solving for ψ yields

$$\psi = \int_0^{\delta_{full}} \frac{\rho V}{(\rho V)_{fs}} dY - \int_0^{\delta_{full}} \frac{\rho V^3}{(\rho V^3)_{fs}} dY \tag{7-6}$$

Ratios of the aforementioned thickness terms are also used as basic boundary-layer parameters. The form factor H is defined as

$$H = \frac{\delta}{\theta} \tag{7-7}$$

Substituting equations (7–2) and (7–4) into equation (7–7) and defining a dimensionless distance y as

$$y = \frac{Y}{\delta_{full}} \tag{7-8}$$

yields

$$H = \frac{\int_0^1 dy - \int_0^1 \frac{\rho V}{(\rho V)_{fs}} dy}{\int_0^1 \frac{\rho V}{(\rho V)_{fs}} dy - \int_0^1 \frac{\rho V^2}{(\rho V^2)_{fs}} dy} \tag{7-9}$$

An energy factor E is defined as

$$E = \frac{\psi}{\theta} \tag{7-10}$$

Substituting equations (7–6), (7–4), and (7–8) into equation (7–10) yields

$$E=\frac{\int_0^1 \frac{\rho V}{(\rho V)_{fs}}dy-\int_0^1 \frac{\rho V^3}{(\rho V^3)_{fs}}dy}{\int_0^1 \frac{\rho V}{(\rho V)_{fs}}dy-\int_0^1 \frac{\rho V^2}{(\rho V^2)_{fs}}dy} \tag{7-11}$$

Velocity profiles for turbulent flow are often represented by a power profile of the type

$$\frac{V}{V_{fs}}=y^n \tag{7-12}$$

where the value of the exponent n is most often between 0.1 and 0.25.

Note that this power profile is here expressed as y^n, while the same profile in chapter 6 (eq. (6–47)) is expressed as $y^{1/n}$. The exponent expressed as $1/n$ is consistent with general boundary-layer theory usage. The exponent expressed as n, however, is consistent with reference 1, wherein the equations that follow are derived. Therefore, the specific numerical value to be used for n will depend on the form being used for the exponent.

With this velocity profile, equations (7–9) and (7–11) can be integrated in series form, and the form and energy factors for turbulent flow can be expressed in terms of the exponent n and the free-stream critical velocity ratio V/V_{cr}. The resulting equations derived in reference 1 are

$$H=\frac{\frac{1}{n+1}+\frac{3A_{fs}}{3n+1}+\frac{5A_{fs}^2}{5n+1}+\cdots}{\frac{1}{(n+1)(2n+1)}+\frac{A_{fs}}{(3n+1)(4n+1)}+\frac{A_{fs}^2}{(5n+1)(6n+1)}+\cdots} \tag{7-13}$$

and

$$E=\frac{2\left[\frac{1}{(n+1)(3n+1)}+\frac{A_{fs}}{(3n+1)(5n+1)}+\frac{A_{fs}^2}{(5n+1)(7n+1)}+\cdots\right]}{\frac{1}{(n+1)(2n+1)}+\frac{A_{fs}}{(3n+1)(4n+1)}+\frac{A_{fs}^2}{(5n+1)(6n+1)}+\cdots} \tag{7-14}$$

where

$$A_{fs}=\frac{\gamma-1}{\gamma+1}\left(\frac{V}{V_{cr}}\right)_{fs}^2 \tag{7-15}$$

and γ is the ratio of specific heat at constant pressure to specific heat at constant volume, and V_{cr} is the fluid velocity, in m/sec or ft/sec, at the critical (Mach 1) flow condition. For incompressible flow, where V/V_{cr} approaches zero, equations (7–13) and (7–14) reduce to

$$H_{inc}=2n+1 \tag{7–16}$$

and

$$E_{inc}=\frac{2(2n+1)}{3n+1} \tag{7–17}$$

Values of the form and energy factors for turbulent compressible flow are shown in figure 7–3 for V/V_{cr} varying from 0 to 1.4 and n varying from 0 to 1.5. It can be seen that the form factor varies much more than does the energy factor. For any constant exponent n, the energy factor is almost independent of V/V_{cr}.

The boundary-layer parameters just presented are general and can refer to a boundary layer on any type of body. They are directly useful in certain aerodynamic work. For instance, the drag of a body can be obtained directly from the momentum thickness. In turbine work, however, where the flow is confined to the physical boundaries of the blade row, it is simpler and more meaningful to express the losses as a fractional part of the ideal quantities that could pass through the blade row. The thickness parameters so expressed are herein termed "dimensionless thickness parameters" and are defined on the basis of zero trailing-edge thickness.

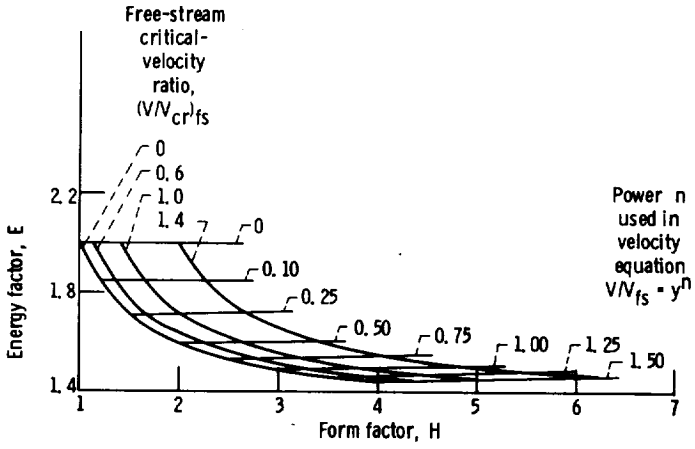

FIGURE 7–3.—Effect of compressibility on variation of energy factor with form factor. (Data from ref. 1.)

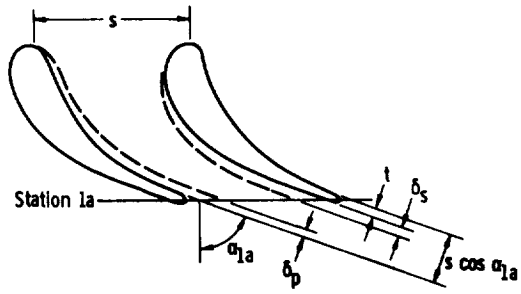

FIGURE 7–4.—Nomenclature for **trailing-edge** region.

These dimensionless thickness parameters must represent the sum of the suction- and pressure-surface thicknesses.

With the assumption that flow conditions in all channels are the same, the dimensionless thickness parameters are obtained by dividing the losses in flow, momentum, and energy for a single blade-row channel by the corresponding ideal quantities that could pass through one blade-row channel. The total losses for one channel, as indicated in figure 7–4, are composed of the suction-surface loss plus the pressure-surface loss, or

$$\delta_{tot}=\delta_s+\delta_p \tag{7–18}$$

$$\theta_{tot}=\theta_s+\theta_p \tag{7–19}$$

$$\psi_{tot}=\psi_s+\psi_p \tag{7–20}$$

where the subscripts *tot*, *s*, and *p* denote total value, suction-surface value, and pressure-surface value, respectively. Thus, in terms of the previously defined boundary-layer thicknesses, the dimensionless boundary-layer thicknesses are expressed as

$$\delta^*=\frac{\delta_{tot}(\rho V)_{fs}}{s\cos\alpha(\rho V)_{fs}}=\frac{\delta_{tot}}{s\cos\alpha} \tag{7–21}$$

$$\theta^*=\frac{\theta_{tot}(\rho V^2)_{fs}}{s\cos\alpha(\rho V^2)_{fs}}=\frac{\theta_{tot}}{s\cos\alpha} \tag{7–22}$$

$$\psi^*=\frac{\psi_{tot}\left(\frac{1}{2}\right)(\rho V^3)_{fs}}{s\cos\alpha\left(\frac{1}{2}\right)(\rho V^3)_{fs}}=\frac{\psi_{tot}}{s\cos\alpha} \tag{7–23}$$

where

δ^* dimensionless displacement thickness
θ^* dimensionless momentum thickness
ψ^* dimensionless energy thickness
s blade spacing, m; ft
α fluid flow angle from axial direction, deg

Equations (7–21), (7–22), and (7–23) express the losses in flow, momentum, and energy, respectively, as fractions of their respective ideal quantities for the blade row if the trailing-edge thickness is assumed to be zero. These equations can be subscripted to apply at either station $1a$, within the trailing edge, or station 1, beyond the trailing edge.

BLADE-ROW LOSS COEFFICIENTS

As mentioned previously, the losses are to be expressed in terms of kinetic-energy loss coefficients. In this section, methods for evaluating the friction, trailing-edge, and mixing losses and expressing them in terms of the kinetic-energy loss coefficients will be presented.

Surface-Friction Losses

The kinetic-energy loss coefficient $\bar{e}_{1a}$, defined as the loss in kinetic energy as a fraction of the ideal kinetic energy of the blade-row actual flow, can be expressed in terms of the boundary-layer dimensionless thicknesses as

$$\bar{e}_{1a} = \frac{\psi^*_{1a} s \cos \alpha_{1a} (\rho V^3)_{fs,1a}}{(s \cos \alpha_{1a} - \delta^*_{1a} s \cos \alpha_{1a} - t)(\rho V^3)_{fs,1a}} \tag{7–24}$$

where t is the blade-row trailing-edge thickness, in m or ft. (Refer to fig. 7–4 for the nomenclature in the region of the trailing edge of the blade.) Since this coefficient is referenced to station $1a$, just within the blade-row trailing edge, it represents only the surface-friction loss. If a trailing-edge dimensionless thickness is expressed as

$$t^* = \frac{t}{s \cos \alpha_{1a}} \tag{7–25}$$

equation (7–24) reduces to

$$\bar{e}_{1a} = \frac{\psi^*_{1a}}{1 - \delta^*_{1a} - t^*} \tag{7–26}$$

In order to evaluate the loss coefficient $\bar{e}_{1a}$ from equation (7–26), it is necessary to know the values of the dimensionless energy thickness ψ^*_{1a}

and the dimensionless displacement thickness δ^*_{1a}. These can be evaluated either experimentally or analytically, as will be discussed herein.

Experimental determination.—In determining experimental loss values, it is impractical to measure the density and velocity directly. Instead, pressure data are taken, and the density and velocity are related to pressure functions. The pressure data required for computing the friction loss consist of (see fig. 7–1) the upstream total pressure p_0', the blade-exit static pressure p_{1a}, and the total-pressure loss survey data $p_0'-p'_{1a}$ for one blade space. Since the dimensionless boundary-layer thicknesses express the losses of the blade row as a fractional part of the ideal quantities which could pass through the blade row, the dimensionless displacement thickness can be expressed in terms of the flow across one blade pitch as

$$\delta^*_{1a}=\frac{s\cos\alpha_{1a}(\rho V)_{fs,1a}-t^*s\cos\alpha_{1a}(\rho V)_{fs,1a}-\cos\alpha_{1a}\int_0^s(\rho V)_{1a}\,du}{s\cos\alpha_{1a}(\rho V)_{fs,1a}} \tag{7–27}$$

where u is the distance in the tangential direction, in m or ft. Equation (7–27) simplifies to

$$\delta^*_{1a}=1-t^*-\int_0^1\left(\frac{\rho V}{\rho_{fs}V_{fs}}\right)_{1a}d\left(\frac{u}{s}\right) \tag{7–28}$$

In a similar manner, the dimensionless momentum and energy thicknesses can be expressed as

$$\theta^*_{1a}=\frac{\int_0^1(\rho VV_{fs})_{1a}\,d\left(\frac{u}{s}\right)-\int_0^1(\rho V^2)_{1a}\,d\left(\frac{u}{s}\right)}{(\rho V^2)_{fs,1a}}$$

$$=\int_0^1\left[1-\left(\frac{V}{V_{fs}}\right)_{1a}\right]\left(\frac{\rho V}{\rho_{fs}V_{fs}}\right)_{1a}d\left(\frac{u}{s}\right) \tag{7–29}$$

and

$$\psi^*_{1a}=\frac{\int_0^1(\rho VV_{fs}^2)_{1a}\,d\left(\frac{u}{s}\right)-\int_0^1(\rho V^3)_{1a}\,d\left(\frac{u}{s}\right)}{(\rho_{fs}V_{fs}^3)_{1a}}$$

$$=\int_0^1\left[1-\left(\frac{V}{V_{fs}}\right)^2_{1a}\right]\left(\frac{\rho V}{\rho_{fs}V_{fs}}\right)_{1a}d\left(\frac{u}{s}\right) \tag{7–30}$$

Assuming that the total temperature T' and the static pressure p_{1a} in

the boundary layer are the same as in the free stream, the density ratio $(\rho/\rho_{fs})_{1a}$ can be related to the pressure ratio p'_{1a}/p_0' as follows: From the isentropic relation,

$$\left(\frac{\rho}{\rho'}\right)_{1a} = \left(\frac{p}{p'}\right)_{1a}^{1/\gamma} \tag{7-31}$$

$$\left(\frac{\rho}{\rho'}\right)_{fs,1a} = \left(\frac{p}{p'}\right)_{fs,1a}^{1/\gamma} \tag{7-32}$$

Since $p'_{fs,1a} = p_0'$ and $\rho'_{1a}/\rho'_{fs,1a} = p'_{1a}/p_0'$ (from the ideal gas law, with $T'_{1a} = T'_{fs,1a} = T_0'$), division of equation (7–31) by equation (7–32) yields

$$\left(\frac{\rho}{\rho_{fs}}\right)_{1a} = \left(\frac{p'_{1a}}{p_0'}\right)^{(\gamma-1)/\gamma} \tag{7-33}$$

The velocity ratio $(V/V_{fs})_{1a}$ can be related to the pressure ratios $(p/p')_{1a}$ and p_{1a}/p_0' as follows: From the total-temperature definition and isentropic relation, equations (1–51) and (1–52) of chapter 1, we can write

$$\frac{V^2}{2gJc_pT'} = 1 - \frac{T}{T'} = 1 - \left(\frac{p}{p'}\right)^{(\gamma-1)/\gamma} \tag{7-34}$$

where

g conversion constant, 1; 32.17 (lbm)(ft)/(lbf)(sec²)
J conversion constant, 1; 778 (ft)(lb)/Btu
c_p specific heat at constant pressure, J/(kg)(K); Btu/(lb)(°R)

Subscripting equation (7–34) once for station $1a$ and again for free-stream values at $1a$, dividing the first of these equations by the second, and recalling that $p'_{fs,1a} = p_0'$ and $T'_{fs,1a} = T'_{1a}$ yields

$$\left(\frac{V}{V_{fs}}\right)_{1a}^2 = \frac{1 - \left(\dfrac{p_{1a}}{p'_{1a}}\right)^{(\gamma-1)/\gamma}}{1 - \left(\dfrac{p_{1a}}{p_0'}\right)^{(\gamma-1)/\gamma}} \tag{7-35}$$

With the density and velocity ratios expressed in terms of the measured pressures by equations (7–33) and (7–35), it is now possible to integrate equations (7–28), (7–29), and (7–30) and evaluate the dimensionless boundary-layer thicknesses. Then, the kinetic-energy loss coefficient $\bar{e}_{1a}$ can be computed from equation (7–26).

The kinetic-energy loss coefficient thus determined is a two-dimensional

coefficient; that is, it is based on data either from a two-dimensional cascade or from a constant radius of an annular cascade. (The annular cascade can be, and often is, the full stator or rotor from a turbine.) In order to obtain a three-dimensional loss coefficient for a blade row, data are taken at a number of radii sufficient to adequately cover the annulus, and the two-dimensional dimensionless boundary-layer thicknesses are calculated as shown previously for each radius. Three-dimensional boundary-layer thicknesses are then obtained by radial integration from hub to tip:

$$\delta^*_{1a,3D} = \frac{\int_{r_h}^{r_t} \delta^*_{1a} (\rho V)_{fs,1a} \cos \alpha_{1a} \, r \, dr}{\int_{r_h}^{r_t} (\rho V)_{fs,1a} \cos \alpha_{1a} \, r \, dr} \tag{7-36}$$

$$\theta^*_{1a,3D} = \frac{\int_{r_h}^{r_t} \theta^*_{1a} (\rho V^2)_{fs,1a} \cos \alpha_{1a} \, r \, dr}{\int_{r_h}^{r_t} (\rho V^2)_{fs,1a} \cos \alpha_{1a} \, r \, dr} \tag{7-37}$$

$$\psi^*_{1a,3D} = \frac{\int_{r_h}^{r_t} \psi^*_{1a} (\rho V^3)_{fs,1a} \cos \alpha_{1a} \, r \, dr}{\int_{r_h}^{r_t} (\rho V^3)_{fs,1a} \cos \alpha_{1a} \, r \, dr} \tag{7-38}$$

In terms of the measured pressures, these integrals are expressed as

$$\delta^*_{1a,3D} = \frac{\int_{r_h}^{r_t} \delta^*_{1a} (p_{1a})^{1/\gamma} \left[1 - \left(\frac{p_{1a}}{p_0'} \right)^{(\gamma-1)/\gamma} \right]^{1/2} \cos \alpha_{1a} \, r \, dr}{\int_{r_h}^{r_t} (p_{1a})^{1/\gamma} \left[1 - \left(\frac{p_{1a}}{p_0'} \right)^{(\gamma-1)/\gamma} \right]^{1/2} \cos \alpha_{1a} \, r \, dr} \tag{7-39}$$

$$\theta^*_{1a,3D} = \frac{\int_{r_h}^{r_t} \theta^*_{1a}(p_{1a})^{1/\gamma}\left[1-\left(\frac{p_{1a}}{p_0'}\right)^{(\gamma-1)/\gamma}\right]\cos\alpha_{1a}\, r\, dr}{\int_{r_h}^{r_t} (p_{1a})^{1/\gamma}\left[1-\left(\frac{p_{1a}}{p_0'}\right)^{(\gamma-1)/\gamma}\right]\cos\alpha_{1a}\, r\, dr} \tag{7-40}$$

$$\psi^*_{1a,3D} = \frac{\int_{r_h}^{r_t} \psi^*_{1a}(p_{1a})^{1/\gamma}\left[1-\left(\frac{p_{1a}}{p_0'}\right)^{(\gamma-1)/\gamma}\right]^{3/2}\cos\alpha_{1a}\, r\, dr}{\int_{r_h}^{r_t} (p_{1a})^{1/\gamma}\left[1-\left(\frac{p_{1a}}{p_0'}\right)^{(\gamma-1)/\gamma}\right]^{3/2}\cos\alpha_{1a}\, r\, dr} \tag{7-41}$$

The three-dimensional kinetic-energy loss coefficient is then obtained in a manner similar to equation (7–26):

$$\bar{e}_{1a,3D} = \frac{\psi^*_{1a,3D}}{1-\delta^*_{1a,3D}-t_m^*} \tag{7-42}$$

where t_m^* is the trailing-edge dimensionless thickness at the mean radius and is used to represent the average value for the blade row.

Analytical determination.—The kinetic-energy loss coefficient $\bar{e}_{1a}$ can also be evaluated with the use of analytically determined boundary-layer thickness parameters. While not as reliable as experimental values, analytical values are much less costly and time consuming to obtain. Analytical methods for calculating the basic boundary-layer parameters are discussed and referenced in chapter 6. The boundary-layer solutions are not simple, and the better methods require computer solution. Boundary-layer computer programs currently in use at the NASA Lewis Research Center include one (ref. 2) based on an integral method solution and another based on the finite difference method of reference 3.

An equation used in the study of reference 4 to compute turbulent boundary-layer momentum thickness was

$$\theta_{1a} = \frac{0.231}{\left(\frac{\rho V}{\rho' V_{cr}}\right)_{fs,1a}\left(\frac{V}{V_{cr}}\right)^{(1+H_{1a})}_{fs,1a}} \times \left\{ \int_0^t \frac{\left[\left(\frac{\rho V}{\rho' V_{cr}}\right)_{fs}\left(\frac{V}{V_{cr}}\right)^{(1+H)}_{fs}\right]^{1.268}\left(\frac{\mu}{\rho V}\right)^{0.268}_{fs}(1-A_{fs})^{0.467}\, dx}{10^{0.678(2n+1)}} \right\}^{0.7686} \tag{7-43}$$

where

A_{fa} parameter defined by equation (7–15)
x distance along blade surface from forward stagnation point, m; ft
l blade-surface distance from forward to rear stagnation point, m; ft
μ viscosity, (N)(sec)/m^2; lb/(ft)(sec)

The development of this equation is presented in reference 4. It is assumed that the boundary layer has a power-law velocity profile. In reference 4, the exponent n was obtained from the referenced equation

$$\frac{1}{n}=2.6\left[\left(\frac{\rho V}{\mu}\right)_{fa} x\right]^{1/14} \tag{7–44}$$

Equation (7–43) must be evaluated for both the suction and pressure surfaces of the blade. The free-stream velocities and densities required for equations (7–43) and (7–44) are those free-stream values adjacent to the blade-surface boundary layers. These can be obtained by any of the channel flow analysis techniques discussed in chapter 5.

Values of the form factor H as required in equation (7–43) and of the form factor H_{1a} and energy factor E_{1a} at station $1a$ for each surface can be obtained from equations (7–13) and (7–14). With θ_{1a}, H_{1a}, and E_{1a} known for both the suction and pressure surfaces, the various boundary-layer thickness parameters and the kinetic-energy loss coefficient $\bar{e}_{1a}$ can be evaluated from the equations presented earlier in this chapter. For the turbine stator blade studied in reference 4, the analytical values, as calculated from equation (7–43), of the boundary-layer momentum thickness for the blade and for the two surfaces individually were reasonably close to the experimental values. In general, however, results obtained from equation (7–43) will not be as accurate as those obtained from the computer programs of references 2 and 3.

Three-dimensional boundary-layer parameters could be calculated directly from equations (7–36) to (7–38). The two-dimensional thickness parameters would have to be analytically determined at a number of radii sufficient to establish the variation over the blade length and would also have to be determined, somehow, over the end-wall surfaces. Such a procedure would require considerable effort, so the simplified method of reference 5 for predicting three-dimensional losses from two-dimensional mean-section losses is commonly used. Results obtained by this method have shown good agreement with experimental results.

In the method of reference 5, the following assumptions are made: (1) The average momentum loss for the blade surface can be represented by the dimensionless momentum thickness at the blade mean section;

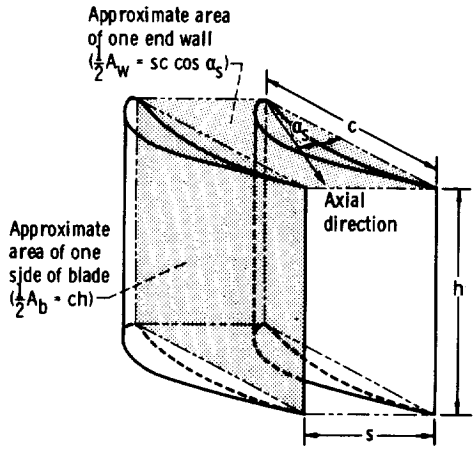

FIGURE 7–5.—Schematic diagram of equivalent two-dimensional blade used to calculate the effect of end-wall area on blade loss.

(2) the momentum loss per unit area on the inner and outer end walls is the same as the average momentum loss per unit area on the blade surface; and (3) the blade configuration can be satisfactorily approximated by an equivalent two-dimensional blade, as shown in figure 7–5, having a constant cross section, spacing, and stagger angle equal to those at the mean section of the given blade. The surface area of one equivalent blade (see fig. 7–5) is

$$A_b = 2ch \tag{7–45}$$

where

A_b total surface area (sum of suction-surface and pressure-surface areas) of one blade, m^2; ft^2
c blade chord, m; ft
h blade height, m; ft

The inner and outer end-wall area for one passage is

$$A_w = 2sc \cos \alpha_s \tag{7–46}$$

where

A_w total surface area of passage end walls (sum of inner and outer end-wall areas), m^2; ft^2
α_s blade stagger angle, deg

Now, taking the average momentum loss $\theta^*_{1a,m}$ over the blade radial length

and modifying it to include the end-wall losses yields

$$\theta^*_{1a,3D} = \theta^*_{1a,m}\left(\frac{A_b + A_w}{A_b}\right) = \theta^*_{1a,m}\left(1 + \frac{s\cos\alpha_s}{h}\right) \tag{7–47}$$

The three-dimensional energy and displacement thickness parameters are then calculated as

$$\psi^*_{1a,3D} = E_{1a,m}\theta^*_{1a,3D} \tag{7–48}$$

and

$$\delta^*_{1a,3D} = H_{1a,m}\theta^*_{1a,3D} \tag{7–49}$$

Mean-section values are used for the energy and form factors. Although the energy and form factors were originally defined in terms of individual boundary-layer thicknesses, it is indicated in reference 4 that they can be satisfactorily used as is done in equations (7–48) and (7–49). The three-dimensional kinetic-energy loss coefficient is then obtained from equation (7–42).

Trailing-Edge Loss

The kinetic-energy loss coefficient $\bar{e}_{te}$ that represents the loss associated with flow past the blade trailing edge can be determined either experimentally or analytically.

Experimental determination.—Experimental values of blade trailing-edge loss coefficient $\bar{e}_{te}$ are obtained from differences between experimental two-dimensional loss coefficients $\bar{e}_1$, which include both surface-friction loss and trailing-edge loss, and loss coefficients $\bar{e}_{1a}$, which include only the blade surface-friction loss. Thus,

$$\bar{e}_{te} = \bar{e}_1 - \bar{e}_{1a} \tag{7–50}$$

Loss coefficients $\bar{e}_{1a}$, which include only surface-friction loss, are obtained as described previously. Loss coefficients $\bar{e}_1$, which include both surface-friction loss and trailing-edge loss, are determined in exactly the same manner except that the total-pressure loss and static pressure are measured at different locations. The surface-friction loss coefficients were based on data obtained just within the blade trailing edge at station 1*a*, where the trailing-edge loss has not yet occurred. To determine the loss coefficients which include both surface-friction loss and trailing-edge loss, the measurements must be made at a location just downstream of the blade row, corresponding to station 1 in figure 7–1, where the trailing-edge loss, but little mixing, has occurred.

Analytical determination.—In reference 6, experimental drag coefficients are presented for a large number of surface discontinuities. Included in the reference are experimental data for sheet-metal joints of different

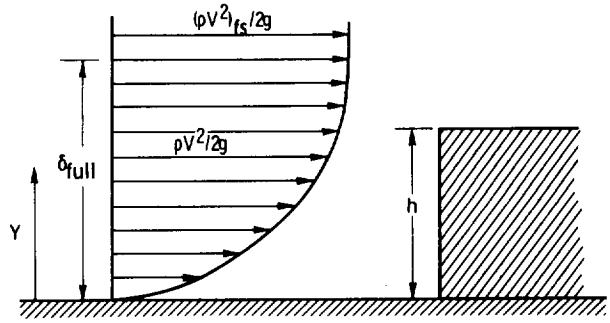

FIGURE 7–6.—Schematic diagram of body in boundary layer.

geometry, bolt and rivet heads of different geometry, and airfoil trailing edges. It is indicated that the pressure-drag loss due to the discontinuity behaves similarly regardless of the flow direction over the discontinuity. Therefore, the loss due to flow past a trailing edge will be treated analytically as if the loss were due to a body placed in the path of a boundary layer.

As indicated in reference 6, the drag of a small body of height h, equal to or less than the full boundary-layer height δ_{full}, placed in a turbulent boundary layer, as shown in figure 7–6, corresponds approximately to the effective dynamic pressure of the part of the boundary layer equal to the height of the body. Thus,

$$D = q_{eff} h C_D \tag{7-51}$$

where

D drag on body, N/m; lb/ft
h height of body, m; ft
C_D drag coefficient

and the effective dynamic pressure q_{eff} is expressed as

$$q_{eff} = \frac{1}{h}\int_0^h \frac{\rho V^2}{2g}\, dY \tag{7-52}$$

Drag is related to momentum thickness as

$$D = \frac{\theta(\rho V^2)_{fs}}{g} \tag{7-53}$$

Therefore, a dimensionless momentum thickness θ^*_{te} representing the trailing-edge loss is obtained by combining equations (7–51) and (7–53) with a properly subscripted form of equation (7–22):

$$\theta^*_{te}=\frac{q_{eff}hC_D}{s\cos\alpha_1\dfrac{(\rho V^2)_{fs}}{g}} \tag{7-54}$$

The flow angle α_1 is related to the angle α_{1a} as discussed in chapter 4 (eqs. (4–26) and (4–27)).

Before equation (7–54) can be evaluated, the effective dynamic pressure must be determined. The ratio of the effective dynamic pressure to the free-stream dynamic pressure is equal to

$$\frac{q_{eff}}{q_{fs}}=\frac{1}{h}\int_0^h\left(\frac{\rho}{\rho_{fs}}\right)\left(\frac{V}{V_{fs}}\right)^2 dY \tag{7-55}$$

For turbulent flow, the variation of velocity in the boundary layer can be expressed with the use of the simple power profile presented previously. Combining equations (7–8) and (7–12) yields

$$\frac{V}{V_{fs}}=\left(\frac{Y}{\delta_{full}}\right)^n \tag{7-56}$$

Assuming that the total temperature and static pressure in the boundary layer and free stream are the same and using the ideal gas law and equation (1–64) of chapter 1 gives

$$\frac{\rho}{\rho_{fs}}=\frac{\dfrac{T_{fs}}{T_0'}}{\dfrac{T}{T_0'}}=\frac{1-\dfrac{\gamma-1}{\gamma+1}\left(\dfrac{V}{V_{cr}}\right)^2_{fs}}{1-\dfrac{\gamma-1}{\gamma+1}\left(\dfrac{V}{V_{cr}}\right)^2} \tag{7-57}$$

Substituting equations (7–56) and (7–57) in equation (7–55) and using the parameter A_{fs} defined by equation (7–15) yields

$$\frac{q_{eff}}{q_{fs}}=\frac{1}{h}(1-A_{fs})\int_0^h\frac{1}{\left[1-A_{fs}\left(\dfrac{Y}{\delta_{full}}\right)^{2n}\right]}\left(\frac{Y}{\delta_{full}}\right)^{2n}dY \tag{7-58}$$

Performing a binomial expansion and integrating then gives

$$\frac{q_{eff}}{q_{fs}}=(1-A_{fs})\left[\left(\frac{h}{\delta_{full}}\right)^{2n}\frac{1}{2n+1}+\left(\frac{h}{\delta_{full}}\right)^{4n}\frac{A_{fs}}{(4n+1)}+\left(\frac{h}{\delta_{full}}\right)^{6n}\frac{A_{fs}^2}{(6n+1)}+\cdots\right] \tag{7-59}$$

Substituting equation (7–59) in equation (7–54) and using trailing-edge thickness t in place of body height h finally yields

$$\theta^*_{te}=\frac{tC_D}{2s\cos\alpha_1}(1-A_{fs})\left[\left(\frac{t}{\delta_{full}}\right)^{2n}\frac{1}{2n+1}+\left(\frac{t}{\delta_{full}}\right)^{4n}\frac{A_{fs}}{(4n+1)}+\left(\frac{t}{\delta_{full}}\right)^{6n}\frac{A_{fs}^2}{(6n+1)}+\cdots\right] \quad (7\text{–}60)$$

The boundary-layer thickness δ_{full} to be used in equation (7–60) should be the sum of the suction- and pressure-surface values.

Equation (7–60) is for compressible flow. In many cases, at least when n is not well known, the following simplified equation, which assumes incompressible flow and $n=1/7$ (commonly used for turbulent flow), is adequate:

$$\theta^*_{te}=0.375\sqrt[3]{\frac{t}{\delta_{full}}}\frac{tC_D}{s\cos\alpha_1} \quad (7\text{–}61)$$

The information in reference 6 indicates that the drag coefficient C_D can be set equal to 0.16 for a rounded trailing edge and 0.22 for a square trailing edge. The corresponding values reported in reference 7 and converted to the same basis as equation (7–61) are 0.14 for a rounded trailing edge and 0.22 for a square trailing edge. Frequently, δ_{tot} instead of δ_{full} will be available. In such a case, for incompressible flow,

$$\delta_{full}=\delta_{tot}\left(\frac{1}{n}+1\right) \quad (7\text{–}62)$$

and for compressible flow,

$$\delta_{full}=\frac{\delta_{tot}}{1-(1-A_{fs})\left(\frac{1}{n+1}+\frac{A_{fs}}{3n+1}+\frac{A_{fs}^2}{5n+1}+\cdots\right)} \quad (7\text{–}63)$$

Equations (7–60) and (7–61) give the fractional loss in blade-row momentum due to the blade trailing edge. To find the corresponding kinetic-energy loss coefficient, it is necessary to find the fractional losses in flow and kinetic energy. As a simple approximation, the form and energy factors, evaluated from equations (7–13) and (7–14) for compressible flow and from equations (7–16) and (7–17) for incompressible flow, are used to obtain

$$\delta^*_{te}=H\theta^*_{te} \quad (7\text{–}64)$$

and

$$\psi^*_{te}=E\theta^*_{te} \quad (7\text{–}65)$$

At station 1, which is just downstream of the blade trailing edge, fluid has flowed into the area behind the trailing edge and there is no longer a void due to trailing-edge blockage. Therefore, a kinetic-energy loss coefficient is obtained as

$$\bar{e}_{te}=\frac{\psi^*_{te}}{1-\delta^*_{te}} \tag{7–66}$$

This loss coefficient expresses the loss in kinetic energy as a fraction of the ideal kinetic energy of the flow that would exist if the trailing-edge loss were the only loss. The trailing-edge kinetic-energy loss coefficient for incompressible flow is plotted against trailing-edge thickness in figure 7–7 for several values of the ratio of trailing-edge thickness to boundary-layer thickness. This figure is based on the momentum loss as expressed by equation (7–61). The flow loss associated with blade-surface friction is not included in equation (7–66). Therefore, this trailing-edge kinetic-energy loss coefficient is approximately, but not rigorously, additive with the surface-friction loss coefficient. Expression of the combined friction and trailing-edge loss in terms of a kinetic-energy loss coefficient is discussed in the next section.

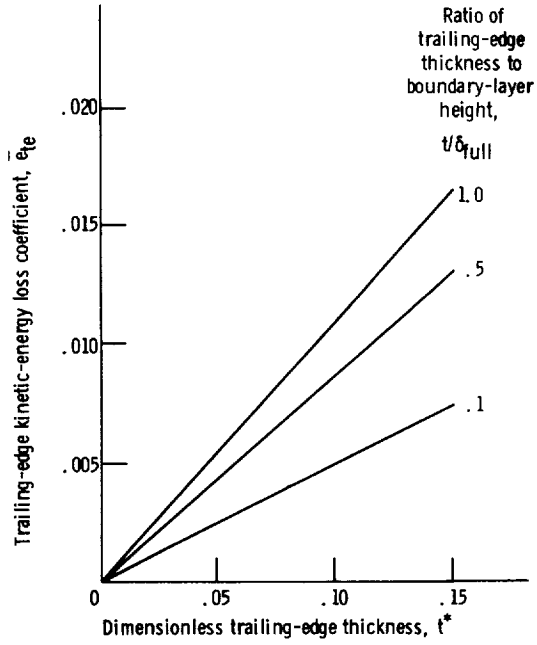

FIGURE 7–7.—Effect of trailing-edge blockage on kinetic-energy loss coefficient. Form factor $H=1.3$; energy factor $E=1.8$; drag coefficient $C_D=0.16$.

Combined Friction and Trailing-Edge Loss

As stated in the discussion of the trailing-edge loss, the boundary-layer thickness parameters and a kinetic-energy loss coefficient expressing the combined friction and trailing-edge loss can be obtained by making the experimental measurements at a location corresponding to station 1, which is just downstream of the trailing edge. In this way, we obtain experimental values of δ_1^*, θ_1^*, and ψ_1^* from appropriately subscripted versions of equations (7–28), (7–29), and (7–30). The value of $\bar{e}_1$ is then obtained as

$$\bar{e}_1 = \frac{\psi_1^*}{1-\delta_1^*} \tag{7–67}$$

Analytically, the boundary-layer thickness parameters at station 1 are obtained by adding the surface-friction loss to the trailing-edge loss. Before the friction and trailing-edge boundary-layer thickness parameters can be added, they must be expressed on the basis of the same ideal flow. The friction-loss dimensionless thicknesses at station $1a$ (δ_{1a}^*, θ_{1a}^*, ψ_{1a}^*) are expressed in terms of an ideal flow without trailing-edge blockage. However, there is a trailing-edge blockage at station $1a$, where the ideal flow with blockage must be comparable to the ideal flow at station 1, where there is no blockage. Therefore, the friction-loss boundary-layer thickness parameters are adjusted to account for the true (with blockage) ideal flow as follows:

$$\delta_{1,f}^* = \delta_{1a}^* \left(\frac{s \cos \alpha_{1a}}{s \cos o_{1a} - t} \right) \tag{7–68}$$

$$\theta_{1,f}^* = \theta_{1a}^* \left(\frac{s \cos \alpha_{1a}}{s \cos \alpha_{1a} - t} \right) \tag{7–69}$$

and

$$\psi_{1,f}^* = \psi_{1a}^* \left(\frac{s \cos \alpha_{1a}}{s \cos \alpha_{1a} - t} \right) \tag{7–70}$$

where the subscript f refers to the loss due to surface friction. Adding the friction and trailing-edge loss parameters then yields the combined loss parameters at station 1:

$$\delta_1^* = \delta_{1,f}^* + \delta_{te}^* \tag{7–71}$$

$$\theta_1^* = \theta_{1,f}^* + \theta_{te}^* \tag{7–72}$$

and

$$\psi_1^* = \psi_{1,f}^* + \psi_{te}^* \tag{7–73}$$

And the value of $\bar{e}_1$ is then obtained from equation (7–67).

After-Mix Loss

The after-mix loss is the total loss that includes the surface-friction loss, the trailing-edge loss, and the mixing loss. The after-mix loss coefficient $\bar{e}_2$ is determined as described in this section, and the mixing loss, if desired, is obtained by subtracting the previously determined $\bar{e}_1$ from $\bar{e}_2$.

To determine the after-mix loss experimentally would require that the pressure measurements be made downstream of the blading where complete mixing has occurred. This is impractical for several reasons: (1) The length for complete mixing, while quite long, is unknown; (2) the after-mix loss would have to be corrected for side-wall friction for the mixing length, thus leading to possible error; and (3) after the flow had mixed, values of after-mix $p_0' - p_2'$ would be constant and small enough that the possibility of measurement error would be relatively large. For these reasons, values of after-mix loss are obtained analytically with the use of either experimentally or analytically determined before-mix (station 1) loss parameters.

The basic equations for determining the after-mix conditions are those for conservation of mass, momentum in the tangential direction, and momentum in the axial direction during mixing. Equating the mass flow rate before mixing (station 1) and after mixing (station 2) yields

$$\int_0^1 (\rho V)_1 \cos \alpha_1 \, d\left(\frac{u}{s}\right) = \cos \alpha_2 (\rho V)_2 \tag{7–74}$$

From conservation of momentum in the tangential direction we get

$$\int_0^1 (\rho V^2)_1 \sin \alpha_1 \cos \alpha_1 \, d\left(\frac{u}{s}\right) = \sin \alpha_2 \cos \alpha_2 (\rho V^2)_2 \tag{7–75}$$

and from conservation of momentum in the axial direction we get

$$g \int_0^1 p_1 \, d\left(\frac{u}{s}\right) + \int_0^1 (\rho V^2) \cos^2 \alpha_1 \, d\left(\frac{u}{s}\right) = g p_2 + \cos^2 \alpha_2 (\rho V^2)_2 \tag{7–76}$$

Although these equations are subscripted for two-dimensional flow, they can also be applied to three-dimensional flow by integrating radially.

If experimental survey data were available at station 1, the integrals in the above equations could be directly evaluated even with variations in static pressure and flow angle. These conservation equations could be written for any before-mix location at which data were available, and then used to evaluate the after-mix loss coefficient. In the case where the before-mix station is not station 1, it would not be possible to determine

the mixing loss completely by experimental means. In most cases, however, it is only the final after-mix loss that is desired, and survey measurements are usually made a little farther downstream of the trailing edge, where angle and pressure variations have somewhat damped out.

If static pressure and flow angle are constant across station 1, it is possible to express equations (7–74) to (7–76) in terms of the previously used boundary-layer parameters, as was done in reference 1. The analysis herein differs from that of reference 1 only in that the before-mix station used in reference 1 corresponds to station 1a herein. Equation (7–28) subscripted for station 1, where there is no trailing-edge void, can be written as

$$\int_0^1 (\rho V)_1 \, d\left(\frac{u}{s}\right) = (1-\delta_1^*)(\rho V)_{fs,1} \tag{7–77}$$

Subscripting equation (7–29) for station 1 and combining it with equation (7–77) yields

$$\int_0^1 (\rho V^2)_1 \, d\left(\frac{u}{s}\right) = (1-\delta_1^*-\theta_1^*)(\rho V^2)_{fs,1} \tag{7–78}$$

Substituting equations (7–77) and (7–78) into equations (7–74) to (7–76) yields the following equations for conservation of mass and momentum in terms of the boundary-layer parameters previously determined:

$$\cos\alpha_1(1-\delta_1^*)(\rho V)_{fs,1} = \cos\alpha_2(\rho V)_2 \tag{7–79}$$

$$\sin\alpha_1\cos\alpha_1(1-\delta_1^*-\theta_1^*)(\rho V^2)_{fs,1} = \sin\alpha_2\cos\alpha_2(\rho V^2)_2 \tag{7–80}$$

$$gp_1+\cos^2\alpha_1(1-\delta_1^*-\theta_1^*)(\rho V^2)_{fs,1} = \cos^2\alpha_2(\rho V^2)_2+gp_2 \tag{7–81}$$

These equations, along with the ideal gas law and the conservation-of-energy equation ($T_1' = T_2'$), can be solved simultaneously as shown in reference 1 to obtain $\bar{e}_2$, the after-mix kinetic-energy loss coefficient, for both compressible and incompressible flow.

For incompressible flow, the solution for $\bar{e}_2$ is

$$\bar{e}_2 = 1-\frac{\sin^2\alpha_1\left(\dfrac{1-\delta_1^*-\theta_1^*}{1-\delta_1^*}\right)^2+\cos^2\alpha_1(1-\delta_1^*)^2}{1+2\cos^2\alpha_1\left[(1-\delta_1^*)^2-(1-\delta_1^*-\theta_1^*)\right]} \tag{7–82}$$

For compressible flow, no explicit solution was found, and the following steps are required to obtain $\bar{e}_2$:

(1) The parameters C and D are computed from

$$C=\frac{(1-A_{fs,1})\,\dfrac{\gamma+1}{2\gamma}+\cos^2\alpha_1(1-\delta_1^*-\theta_1^*)\left(\dfrac{V}{V_{cr}}\right)^2_{fs,1}}{\cos\alpha_1(1-\delta_1^*)\left(\dfrac{V}{V_{cr}}\right)_{fs,1}} \tag{7-83}$$

$$D=\left(\frac{V}{V_{cr}}\right)_{fs,1}\sin\alpha_1\left(\frac{1-\delta_1^*-\theta_1^*}{1-\delta_1^*}\right) \tag{7-84}$$

(2) The quantity $(V_x/V_{cr})_2$ is obtained from

$$\left(\frac{V_x}{V_{cr}}\right)_2=\frac{\gamma C}{\gamma+1}-\sqrt{\left(\frac{\gamma C}{\gamma+1}\right)^2-1+\left(\frac{\gamma-1}{\gamma+1}\right)D^2} \tag{7-85}$$

(3) The density ratio $(\rho/\rho')_2$ is obtained from

$$\left(\frac{\rho}{\rho'}\right)_2=\left\{1-\left(\frac{\gamma-1}{\gamma+1}\right)\left[D^2+\left(\frac{V_x}{V_{cr}}\right)^2_2\right]\right\}^{1/(\gamma-1)} \tag{7-86}$$

(4) The total pressure ratio p_2'/p_0' is obtained from

$$\frac{p_2'}{p_0'}=\frac{\left(\dfrac{\rho V}{\rho' V_{cr}}\right)_{fs,1}\cos\alpha_1(1-\delta_1^*)}{\left(\dfrac{\rho V_x}{\rho' V_{cr}}\right)_2} \tag{7-87}$$

(5) The pressure ratio $(p/p')_2$ is obtained from

$$\left(\frac{p}{p'}\right)_2=\left(\frac{\rho}{\rho'}\right)^\gamma_2 \tag{7-88}$$

(6) Finally, $\bar{e}_2$ is obtained from

$$\bar{e}_2=\frac{\left(\dfrac{p_0'}{p_2'}\right)^{(\gamma-1)/\gamma}-1}{\left(\dfrac{p_0'}{p_2}\right)^{(\gamma-1)/\gamma}-1} \tag{7-89}$$

Values of $\bar{e}_2$ include all the blade-row loss; that is, the frictional loss of the blade row, the trailing-edge loss, and the mixing loss. Values of $\bar{e}_1$

include all the blade-row losses except mixing loss. Therefore,

$$\bar{e}_{mix} = \bar{e}_2 - \bar{e}_1 \tag{7-90}$$

where $\bar{e}_{mix}$ is the fractional loss in available energy due to mixing.

BLADE-ROW LOSS CHARACTERISTICS

In this section, experimentally and analytically determined losses of the various types considered will be presented and compared, and the effect of blade-row geometry on losses will be discussed.

Distribution and Comparison of Losses

Figure 7–8, taken from reference 8, compares experimentally and analytically determined values of kinetic-energy loss coefficients at three different angle settings for a given stator and at three stations representing different losses. The loss coefficient $\bar{e}_{1a,m}$, obtained just within the blade trailing edge, represents the surface-friction loss at the mean (arithmetic mean radius) section; the coefficient $\bar{e}_{1,m}$, obtained just beyond the trailing edge, represents the friction loss plus trailing-edge loss at the mean section; and the coefficient $\bar{e}_{2,3D}$ represents the total loss for the annulus including blade and end-wall friction, trailing-edge drag, and mixing. In general, agreement between the experimental and analytical loss coefficients is reasonably good.

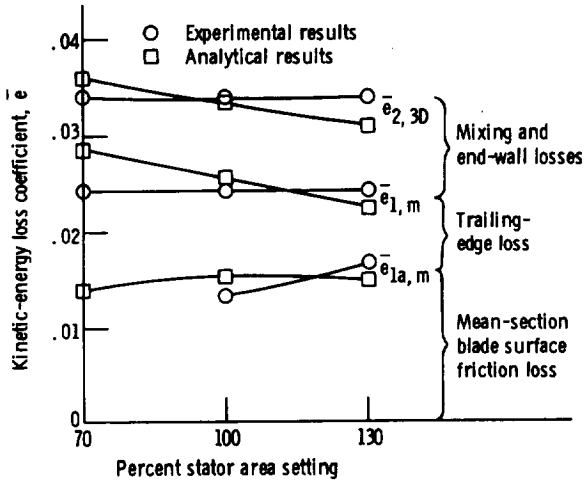

FIGURE 7–8.—Comparison of experimental and analytical loss coefficients for different stator area settings. (Data from ref. 8.)

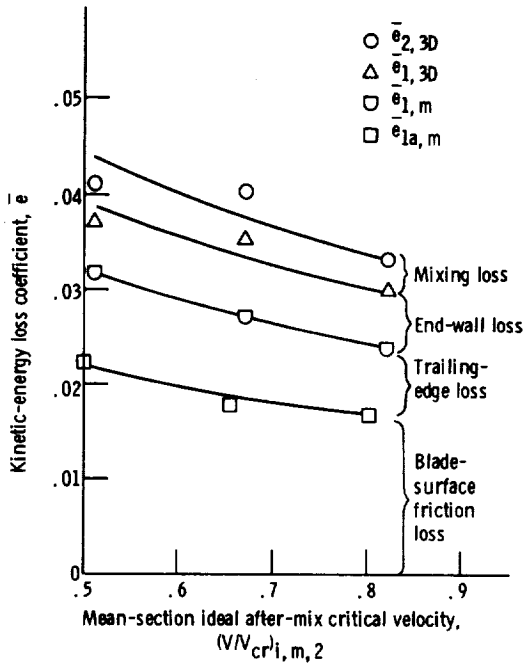

FIGURE 7–9.—Variation of loss coefficients with velocity. (Data from ref. 9.)

Figure 7–8 gives some idea of the distribution of losses in a stator blade row, but does not separate the mixing and end-wall losses. Figure 7–9, taken from reference 9, shows the variation in loss coefficient with velocity. Loss coefficient is seen to decrease slightly with increasing velocity. This figure also shows separately the mixing and end-wall losses, as well as the other blade-row losses.

In this particular case, the friction loss was about 2 percent of the stator ideal energy and about one-half of the total stator loss. The trailing-edge loss was about one-quarter of the total loss. In general, the trailing-edge loss will vary with trailing-edge blockage as was shown in figure 7–7. The end-wall loss, which was about 15 percent of the total loss for this case, will vary with the design, depending primarily on radius ratio and spacing. The mixing loss made up the remaining 10 percent of the total loss. The loss breakdown will, of course, vary with the stator design, but the comparison does indicate that each of the losses may be of consequence.

Effect of Blade-Row Geometry on Losses

A study of the effect of turbine geometry on turbulent-flow boundary-layer loss is presented in reference 10. In that study, the assumption was

made that the momentum loss per unit blade surface varies as the inverse of the chord Reynolds number to the m power:

$$\frac{\theta_{tot}}{c} \propto Re_c^{-m} \tag{7-91}$$

where Re_c is a Reynolds number based on blade chord c. Expanding equation (7–91) by multiplying and dividing by like terms, substituting into equation (7–22), and then using equation (7–47) to express the three-dimensional effect yielded an equation of the form

$$\theta^*_{3D} \propto \left(\frac{h}{s}\right)^m \left[1+\frac{\cos \alpha_2}{\left(\frac{h}{s}\right)}\right] \left(\frac{\theta_{tot}}{c}\right)_{ref} \left(\frac{c}{s}\right)^{1-m} Re_h^{-m} \tag{7-92}$$

$$f\left(\frac{h}{s}\right) \qquad f\left(\frac{c}{s}\right) \qquad f(Re_h)$$

where Re_h is a Reynolds number based on blade height h. As indicated, the three-dimensional momentum thickness parameter can be expressed as a function of the geometric variables—height-to-spacing ratio h/s, blade solidity c/s, and height Reynolds number Re_h. The reference value of θ_{tot}/c, as explained in reference 9, is based on the minimum loss for a given solidity and, therefore, becomes a function of solidity. The exponent m is set equal to $\frac{1}{5}$ in the analysis.

In reference 10, the derivative of the dimensionless momentum thickness θ^*_{3D} with respect to each of the geometric variables was obtained in order to find the minimum-loss value of each variable in terms of the other variables (there is no minimum for height Reynolds number). With the optimum values known, the relative variations in momentum loss around the minimum values were then determined. The results of the analysis from reference 10 are shown in figures 7–10, 7–11, and 7–12. Also shown in each figure is the nature of the geometry variation associated with the change in each variable.

Figure 7–10 shows that a wide variation (50 percent or more) in h/s value around the optimum causes little increase in momentum loss. This results from the two counteracting effects of changes in chord Reynolds number and end-wall area. Figure 7–11 shows that the solidity of a blade may be varied considerably from optimum with some, but not excessive, loss. Comparison of the results in figures 7–10 and 7–11 shows that the loss is more sensitive to solidity than to the height-to-spacing ratio. The curve shape of figure 7–11 reflects also the counteracting influences of chord Reynolds number and end-wall area.

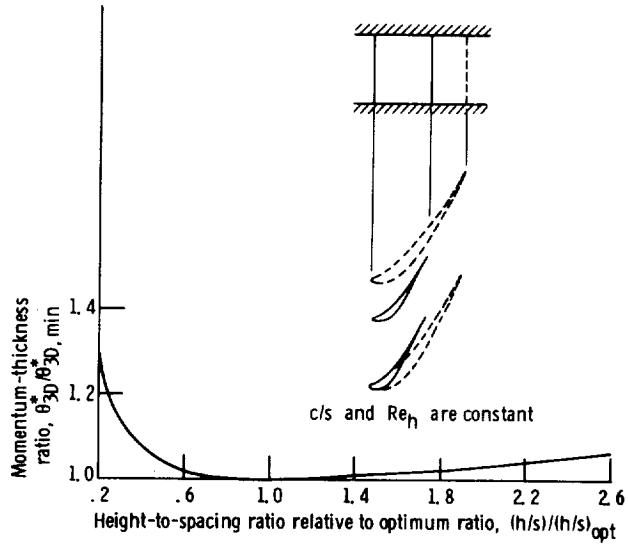

FIGURE 7–10.—Variation of momentum-thickness ratio with variation in height-to-spacing ratio. (Data from ref. 10.)

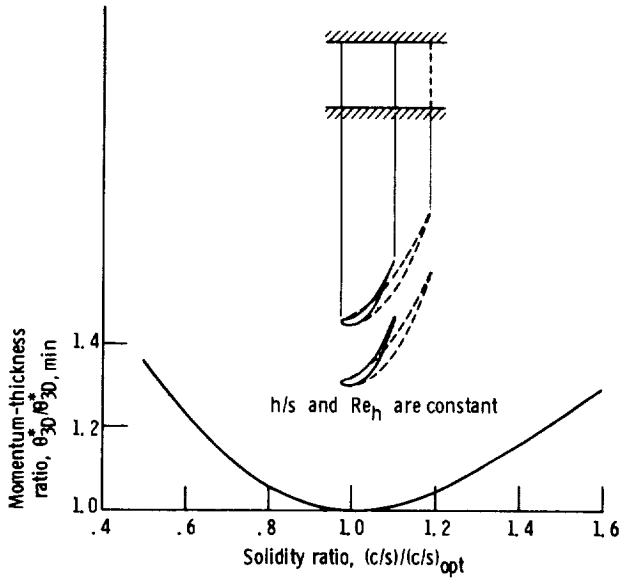

FIGURE 7–11.—Variation of momentum-thickness ratio with solidity ratio. (Data from ref. 10.)

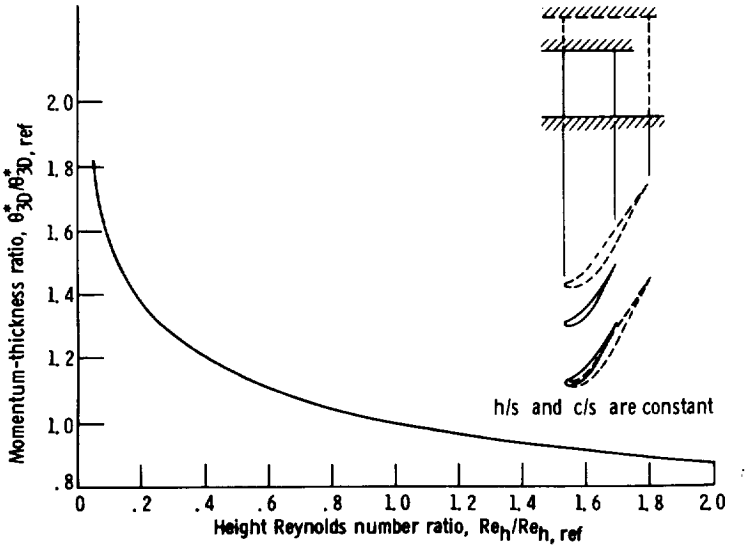

FIGURE 7–12.—Variation of momentum-thickness ratio with height Reynolds number ratio. (Data from ref. 10.)

Figure 7–12 shows the variation of momentum-thickness ratio with height Reynolds number ratio. While the figure indicates a change in Reynolds number due to change in geometry, the change in Reynolds number could also result from change in inlet flow conditions. The curve shape, then, results from the loss being inversely proportional to the Reynolds number to the $m=\frac{1}{5}$ power. These results show that an increase in height Reynolds number results in improved performance. The height Reynolds number is sometimes used in correlating the performance of different turbomachines.

REFERENCES

1. STEWART, WARNER, L.: Analysis of Two-Dimensional Compressible-Flow Loss Characteristics Downstream of Turbomachine Blade Rows in Terms of Basic Boundary-Layer Characteristics. NACA TN 3515, 1955.
2. MCNALLY, WILLIAM D.: FORTRAN Program for Calculating Compressible Laminar and Turbulent Boundary Layers in Arbitrary Pressure Gradients. NASA TN D–5681, 1970.
3. PATANKAR, S. V.; AND SPALDING, D. B.: Heat and Mass Transfer in Boundary Layers. CRC Press, 1967.
4. WHITNEY, WARREN J.; STEWART, WARNER L.; AND MISER, JAMES W.: Experimental Investigation of Turbine Stator-Blade-Outlet Boundary-Layer Characteristics and a Comparison with Theoretical Results. NACA RM E55K24, 1956.

5. STEWART, WARNER L.; WHITNEY, WARREN J.; AND WONG, ROBERT Y.: Use of Mean-Section Boundary-Layer Parameters in Predicting Three-Dimensional Turbine Stator Losses. NACA RM E55L12a, 1956.
6. HOERNER, SIGHARD F.: Fluid-Dynamic Drag. Midland Park, N.J., 1965.
7. PRUST, HERMAN W., JR.; AND HELON, RONALD M.: Effect of Trailing-Edge Geometry and Thickness on the Performance of Certain Turbine Stator Blading. NASA TN D–6637, 1972.
8. PRUST, HERMAN W.; MOFFITT, THOMAS P.; AND BIDER, BERNARD: Effect of Variable Stator Area on Performance of a Single-Stage Turbine Suitable for Air Cooling. V—Stator Detailed Losses with 70-Percent Design Area. NASA TM X–1696, 1968.
9. MOFFITT, THOMAS P.; PRUST, HERMAN W., JR.; AND BIDER, BERNARD: Effect of Variable Stator Area on Performance of a Single-Stage Turbine Suitable for Air Cooling. II—Stator Detailed Losses with 130-Percent Design Area. NASA TM X–1635, 1968.
10. MISER, JAMES W.; STEWART, WARNER L.; AND WHITNEY, WARREN J.: Analysis of Turbomachine Viscous Losses Affected by Changes in Blade Geometry. NACA RM E56F21, 1956.

SYMBOLS

A_b	surface area of one blade, m^2; ft^2
A_{fs}	parameter defined by equation (7–15)
A_w	surface area of end walls for one passage, m^2; ft^2
C	parameter defined by equation (7–83)
C_D	drag coefficient
c	blade chord, m; ft
c_p	specific heat at constant pressure, J/(kg)(K); Btu/(lb)(°R)
D	drag, N/m; lb/ft parameter defined by equation (7–84)
E	energy factor
$\bar{e}$	kinetic-energy loss coefficient
g	conversion constant, 1; 32.17 (lbm)(ft)/(lbf)(sec^2)
H	form factor
h	blade height, m; ft height of body placed in boundary layer, m; ft
J	conversion constant, 1; 778 (ft)(lb)/Btu
l	blade surface distance from forward to rear stagnation point, m; ft
m	exponent in equation (7–91)
n	turbulent boundary-layer velocity profile exponent
p	absolute pressure, N/m^2; lb/ft^2
q	dynamic pressure, N/m^2; lb/ft^2
Re_c	chord Reynolds number
Re_h	height Reynolds number
r	radius, m; ft
s	blade spacing, m; ft
T	absolute temperature, K; °R
t	trailing-edge thickness, m; ft
u	distance in tangential direction, m; ft
V	fluid velocity, m/sec; ft/sec
x	distance along blade surface from forward stagnation point, m; ft
Y	distance from surface normal to boundary layer, m; ft
y	distance from surface normal to boundary layer expressed as fraction of boundary-layer thickness
α	fluid flow angle from axial direction, deg
α_s	blade stagger angle from axial direction, deg
γ	ratio of specific heat at constant pressure to specific heat at constant volume
δ	boundary-layer displacement thickness, m; ft
δ_{full}	boundary-layer thickness, m; ft

θ	boundary-layer momentum thickness, m; ft
μ	viscosity, (N) (sec)/m^2; lb/(ft) (sec)
ρ	density, kg/m^3; lb/ft^3
ψ	boundary-layer energy thickness, m; ft

Subscripts:

cr	critical flow conditions
eff	effective
f	friction
fs	free stream
h	hub
i	ideal
inc	incompressible
m	mean section
min	minimum
mix	mixing
opt	optimum
p	pressure surface
ref	reference
s	suction surface
t	tip
te	trailing edge
tot	total
x	axial component
0	blade-row inlet
1	just beyond trailing edge of blade row
1*a*	just within trailing edge of blade row
2	downstream uniform state
3*D*	three dimensional

Superscripts:

′	absolute total state
*	dimensionless value

CHAPTER 8

Miscellaneous Losses

By Richard J. Roelke

In the last chapter, the boundary-layer losses associated with the flow process in the blade channel were discussed. To determine the overall design-point efficiency of a turbine, other losses must also be considered; these include tip-clearance loss and disk-friction loss. In some instances, these losses represent a very small part of the turbine output and may be neglected; however, in other instances, these losses can be of such magnitude as to influence the selection of the turbine design point. The sum of these losses normally comprises all the losses that are considered in the design of a full-admission axial-flow turbine. If, however, a partial-admission turbine is being considered, there are additional losses that must be included. The partial-admission losses usually considered are the pumping loss in the inactive blade channels and the filling-and-emptying loss in the blade passages as they pass through the admission arc. Finally, a loss that occurs at off-design operation of any turbine is the incidence loss, which will also be covered herein.

TIP-CLEARANCE LOSS

Because a turbine must operate with some clearance between the tips of the rotor blades and the casing, some fraction of the fluid leaks across the tips, thus causing a reduction in turbine work output. This leakage loss is affected, first of all, by the nature of the tip geometry; that is, by the amount of radial clearance, by recesses in the casing, and by tip shrouds. For a given tip geometry, the amount of blade reaction affects the leakage loss, since a large pressure difference across the tip (high reaction) causes more higher-kinetic-energy flow to leak through the tip

gap from the pressure side to the suction side of the blade. With an unshrouded blade, this leakage flow not only causes a loss due to its own reduced work, but also causes an unloading of the blade, primarily in the tip region. Analytical evaluation of the drop in turbine efficiency caused by tip-clearance leakage is inherently difficult because of the complex flow problem. Several empirical expressions for clearance loss have been developed, and some of these are summarized in reference 1; however, they are rather complicated, and the author states that none is entirely satisfactory.

A number of tests have been made at the NASA Lewis Research Center to determine the effect of tip clearance and tip geometry on axial-flow impulse and reaction turbines. An examination of some of the results of these tests helps to obtain a better understanding of the tip-clearance loss. Figure 8–1 shows the angle traces at the blade exit of a 5-inch single-stage turbine (ref. 2). Two things to be noted from the angle traces are that the flow in the clearance space and near the tip was not fully turned,

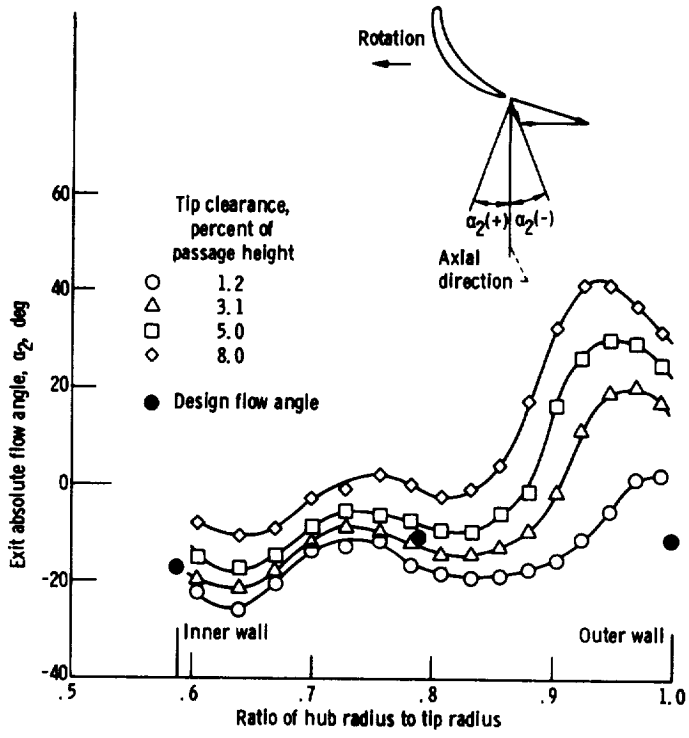

FIGURE 8–1.—Variation of exit flow angle with radius ratio for four rotor tip clearances. (Data from ref. 2.)

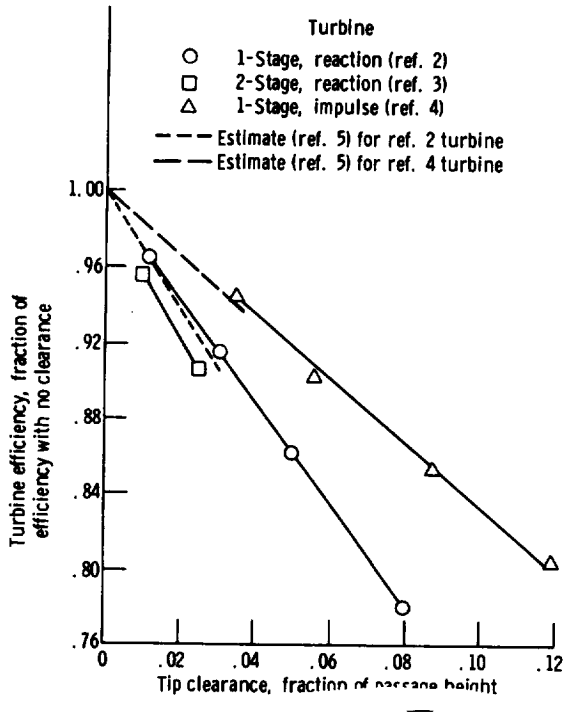

FIGURE 8–2.—Effect of tip clearance on efficiency.

even at the smallest clearance tested, and that underturning of the flow increased with increasing tip clearance, and this effect occurred all the way down to the hub. This underturning of the flow unloads the blade aerodynamically and results in lower turbine output and efficiency. The decrease in efficiency for this turbine, as well as for two others, is shown in figure 8–2.

The solid lines in figure 8–2 represent test results from single-stage (ref. 2) and two-stage (ref. 3) reaction turbines and from a single-stage impulse turbine (ref. 4). All turbines were unshrouded. The importance that the level of reaction plays in the clearance loss is clearly evident from the figure. For the same ratio of tip clearance to blade height, the losses in efficiency for the reaction turbines were about double that for the impulse turbine.

The dashed lines in figure 8–2 are estimates of the efficiency losses for the two single-stage turbines (refs. 2 and 4) as obtained from the curves published in reference 5 (as fig. 1.6) and reproduced here as figure 8–3. Extrapolation of the experimental data of figure 8–2 shows that figure 8–3 gives satisfactory estimates of tip-leakage loss for small tip clearances.

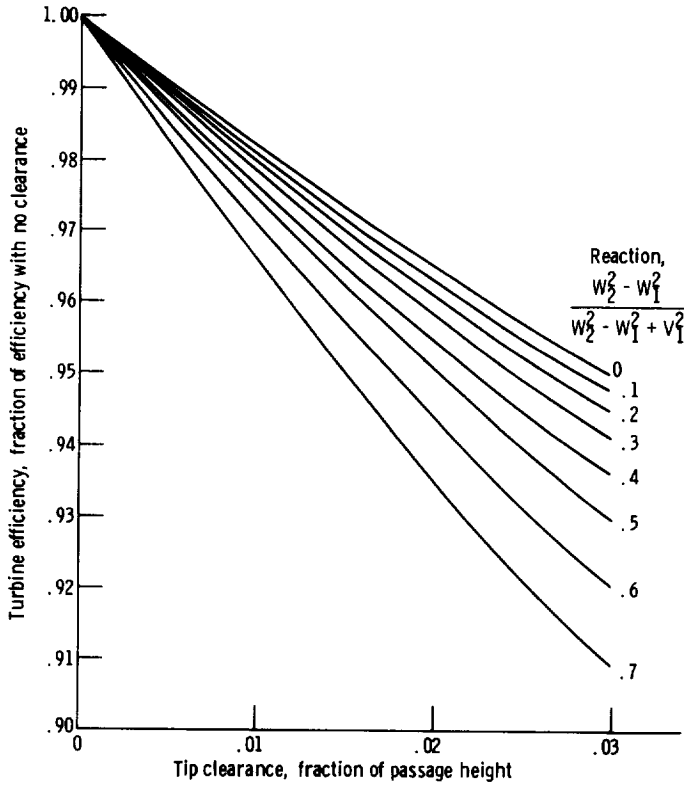

FIGURE 8–3.—Tip-clearance correlation for unshrouded blades. (Data from ref. 5.)

Reviewing the results shown in figures 8–2 and 8–3, it is apparent that the loss in efficiency increases with increasing reaction, and for moderate to large ratios of tip clearance to blade height, the loss is appreciable.

In addition to reducing the tip clearance, methods for reducing the tip-leakage losses include recessing the casing above the blade tip while increasing the blade height, and adding a tip shroud. These loss-reduction schemes can be used either individually or in combination. The single-stage impulse turbine of reference 4 was tested at several ratios of tip clearance to blade height, both without and with the recessed casing and the tip shroud. Figure 8–4 shows the three general configurations tested in reference 4, and the turbine-performance results are shown in figure 8–5. A clearer understanding of the performance characteristics is possible if the loss mechanisms are considered. The factors affecting turbine work for the reduced blade-height configuration as compared to a zero-clearance configuration consist of (1) reduced blade loading area, (2) clearance-gap leakage flow, (3) mixing of the leakage flow with channel throughflow,

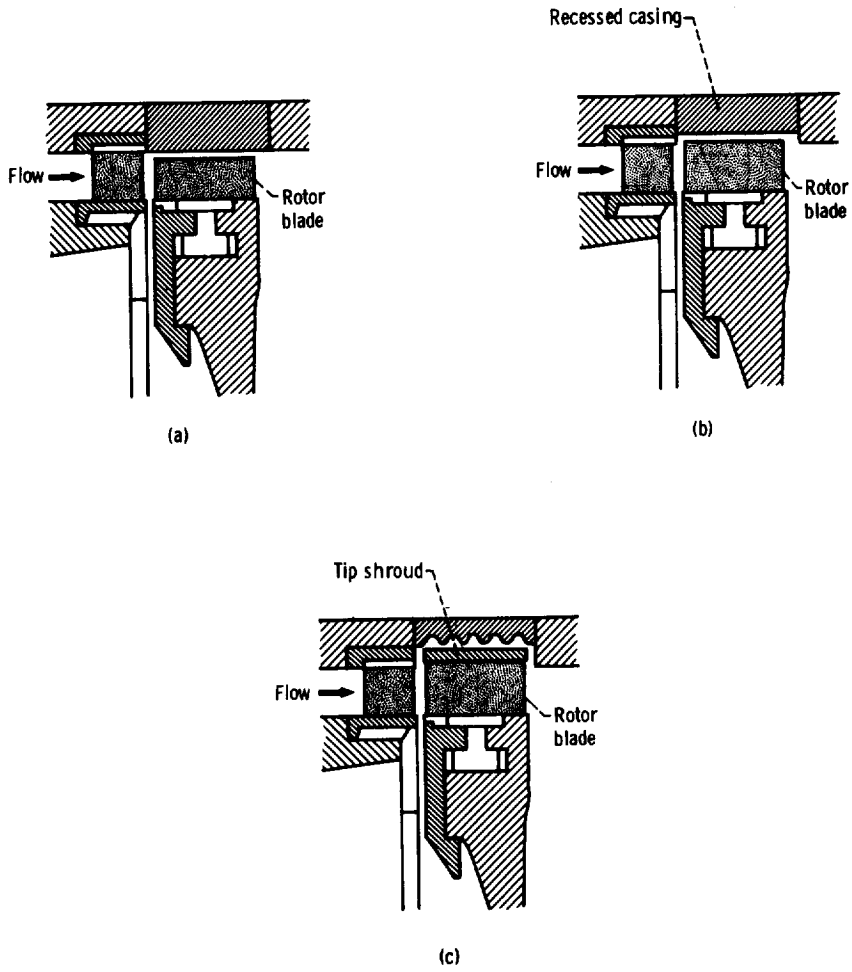

(a) Reduced blade height (relative to zero-clearance blade height).
(b) Recessed casing.
(c) Shrouded rotor.

FIGURE 8–4.—Tip-clearance configurations investigated for impulse turbine (ref. 4).

and (4) blade unloading (as a result of flow going from the pressure side to the suction side). With the recessed-casing configuration, the blade extended to the passage outer radius and was of constant height as the clearance gap was changed by varying the amount of casing recess. Therefore, the reduced blade loading area was eliminated, and the leakage flow was reduced because of the indirect leakage path. With the shroud added to the blade, the blade unloading was eliminated, and the leakage flow was further reduced. Note from figure 8–5, however, that at tip-clearance

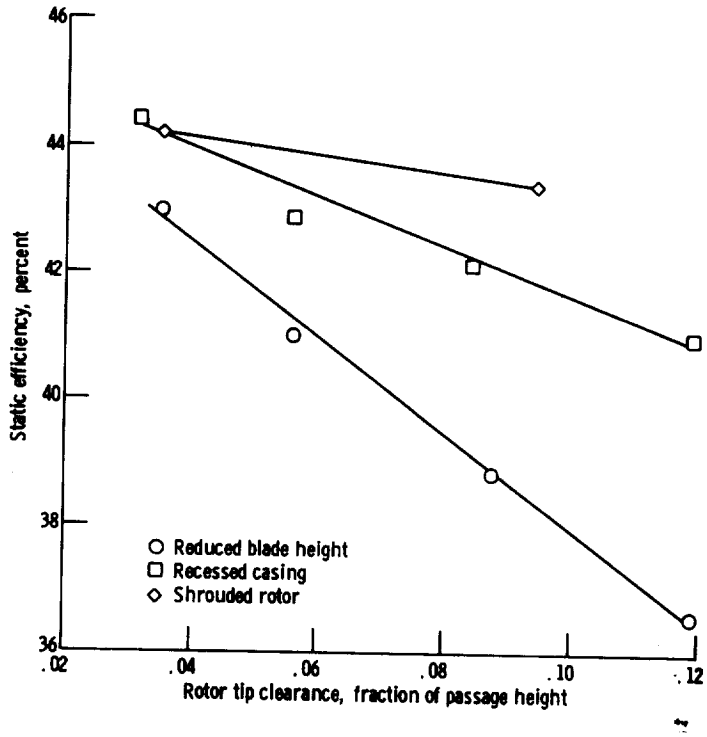

FIGURE 8–5.—Effect of tip-clearance configurations on turbine efficiency. (Data from ref. 4.)

fractions below some value, about 0.035 in this instance, the shroud no longer provides an increase in efficiency. This can be attributed to an increasing friction loss between shroud and casing as the clearance gap is decreased.

The comparative results shown in figure 8–5 for different blade-tip geometries are dependent upon that particular design and may not apply to other turbines. This is particularly true of the shrouded blade, since the leakage flow depends not only on the clearance span and pressure difference but also on the number of seals used. With respect to the recessed-casing configuration, it should be noted that the blade should not extend into the recess. If it does, the overlapping section will just be churning stagnant fluid and creating additional losses.

In summary, tip-clearance loss presents a complicated flow problem influenced by many factors and is not easily predicted with consistent accuracy. The clearance gap required for a turbine depends primarily on diameter (larger clearance for larger diameter) and, as seen previously, the loss increases as the ratio of clearance gap to blade height increases.

For any given diameter, therefore, the tip-clearance loss increases with increasing hub- to tip-radius ratio. It becomes increasingly difficult to maintain a desired small ratio of clearance gap to blade height as the turbine, and hence the blade height, becomes smaller. For a given radius ratio, therefore, the loss is more severe for small turbines and less severe for larger turbines. If tip leakage is considered to be a problem in a particular case, it might be worthwhile to carry out tests to evaluate the leakage effects.

DISK-FRICTION LOSS

The disk-friction loss (or windage loss) is due to the skin friction and circulation of fluid between the rotating disk and the stationary casing. In addition, some turbines for hot applications, for example aircraft engines, have a small steady stream of lower-temperature gas that bathes and cools the rotor disk. This cooling gas flows along the rotor-disk surface from near the engine centerline outward to the base of the blades. The qualitative nature of the flow patterns around rotor disks without and with throughflow of cooling gas are shown in figure 8–6. Equations for estimating the associated losses are presented herein.

No Throughflow

For the case with no throughflow, as in figure 8–6(a), the thin layer of fluid close to the rotating surface is thrown outward by centrifugal action

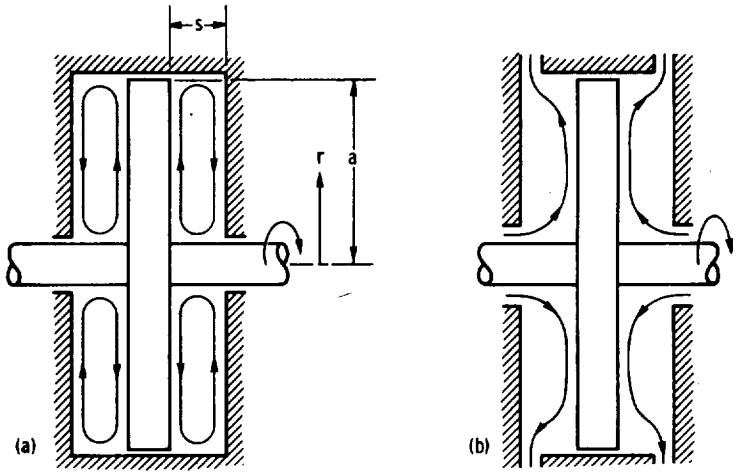

(a) Without throughflow. (b) With throughflow.

FIGURE 8–6.—Flow patterns for rotating disks.

and returns via the stationary wall to the inner radius, thereby building up a continuous circulatory effect. Consider an element of area on one side of the disk

$$dA = 2\pi r\, dr \tag{8–1}$$

where A is the area, in m^2 or ft^2, of one side of the disk, and r is the radius, in m or ft, of the area element dA. The fluid shear stress τ, in N/m^2 or lb/ft^2, acting over this area at the radius r produces a resisting torque to the disk rotation of

$$\frac{dM_o}{2} = \tau 2\pi r^2\, dr \tag{8–2}$$

where M_o is the resisting torque, in N-m or lb-ft, for both sides of a disk in the case of no throughflow. The shear stress can be expressed as

$$\tau = \frac{C_f}{2g}\rho V_u^2 \tag{8–3}$$

where

C_f fluid shear-stress coefficient
g conversion constant, 1; 32.17 (lbm)(ft)/(lbf)(sec^2)
ρ density, kg/m^3; lb/ft^3
V_u tangential component of fluid absolute velocity, m/sec; ft/sec

At the disk surface, the fluid tangential velocity is

$$V_u = r\omega \tag{8–4}$$

where ω is the angular velocity, in rad/sec. By substituting equation (8–4) into (8–3), the total torque for both sides of the disk can be written as

$$M_o = \int_0^a \frac{2\pi}{g} C_f \rho \omega^2 r^4\, dr \tag{8–5}$$

where a is the disk rim radius, in m or ft. Performing the integration yields

$$M_o = C_{M,o}\rho \frac{\omega^2 a^5}{2g} \tag{8–6}$$

where $C_{M,o}$ is a torque coefficient for the case of no throughflow. The disk-friction loss expressed as power is then the torque times the angular velocity:

$$P_{df} = \frac{M_o \omega}{J} = C_{M,o} \frac{\rho \omega^3 a^5}{2gJ} \tag{8–7}$$

where P_{df} is the disk-friction power loss, in W or Btu/sec, and J is a

conversion constant (equal to 1, or 778 (ft)(lb)/Btu). The form of equation (8–7) that is found in most handbooks is

$$P_{df} = K_{df}\rho N^3 D_r^5 \tag{8–8}$$

where

K_{df} disk-friction power-loss coefficient
N rotative speed
D_r disk rim diameter

A number of investigators have published values of the constant K_{df} in equation (8–8) to be used for different circumstances, while others have made small changes to the exponents to better fit the available data. The wide assortment of semiempirical equations used to predict this loss is, no doubt, due to variations of the test-apparatus geometry, the somewhat oversimplified model from which equation (8–7) is derived, and the existence of different types of flow that can occur in the space between the rotor and the casing. One thing that can be noted from equation (8–7) or (8–8) is that for a given blade speed, lower loss is obtained by having a smaller diameter and a higher rotative speed.

An extensive investigation has been conducted (refs. 6 and 7) to determine the effect of chamber proportions on disk friction and to present a clearer picture of the several modes of flow that may exist. In general, four modes of flow, or flow regimes, can exist in the axial space between the casing and the rotating disk, depending on the chamber dimensions and the flow Reynolds number. The torque coefficient $C_{M,o}$ was evaluated both theoretically and experimentally in each regime. A description of each regime and the associated equations for the torque coefficient are as follows:

Regime I: Laminar Flow, Small Clearance. Boundary layers on the rotor disk and casing are merged, so that a continuous variation in velocity exists across the axial gap s. Figure 8–7(a) indicates the nature of the variations in the radial and tangential components of fluid velocity at a given radius in the gap. The best equation for torque coefficient, both theoretically and empirically, is

$$C_{M,o} = \frac{2\pi}{(s/a)R} \tag{8–9}$$

where s is the axial distance, in m or ft, between disk and casing, and R is the Reynolds number defined as

$$R = \frac{\omega a^2 \rho}{\mu} \tag{8–10}$$

where μ is the dynamic viscosity, in (N)(sec)/m² or lb/(ft)(sec).

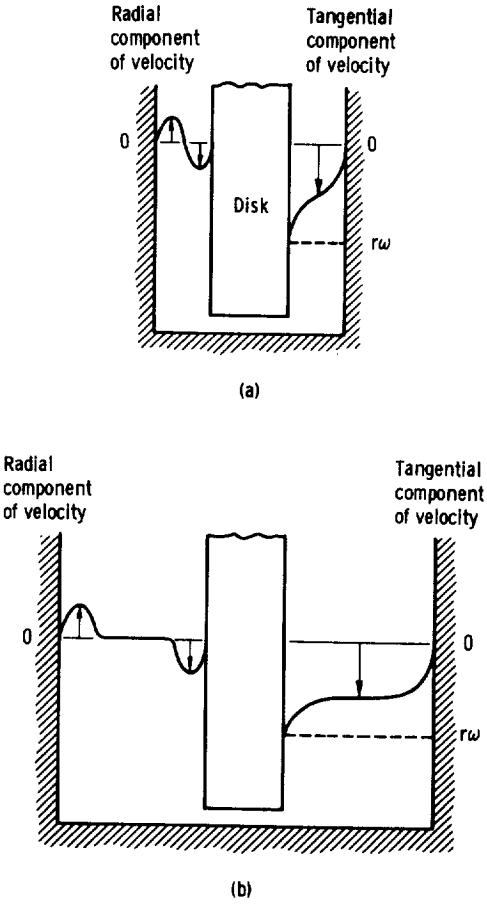

(a) Flow regimes I and III.
(b) Flow regimes II and IV.

FIGURE 8–7.—Velocity patterns around rotating disks without throughflow.

Regime II: Laminar Flow, Large Clearance. The combined thickness of the boundary layers on the rotor and on the casing is less than the axial gap, and between these boundary layers there exists a core of rotating fluid in which no change in velocity occurs. Figure 8–7(b) shows the variations in the radial and tangential velocity components for this case. The best theoretical and empirical equations for torque coefficient are

$$C_{M,o}=\frac{C_{II}}{R^{1/2}} \tag{8–11}$$

where C_{II} is a function of (s/a), as shown in figure 8–8(a), and

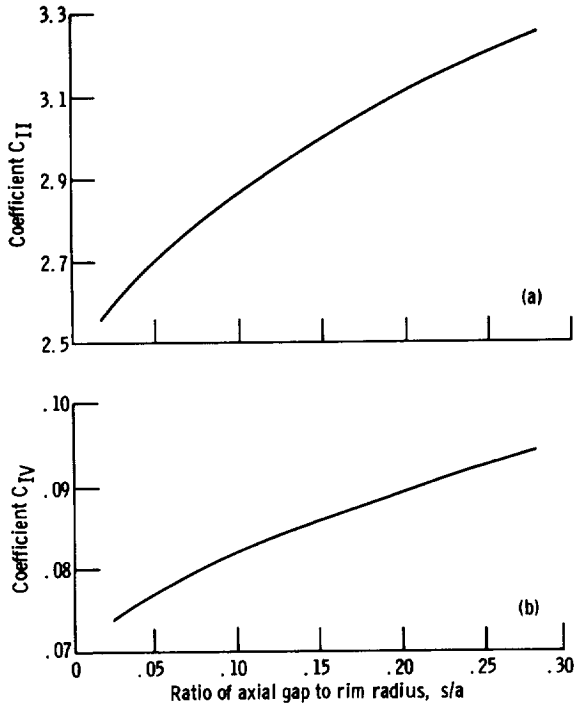

(a) Flow regime II.
(b) Flow regime IV.

FIGURE 8–8.—Evaluation of torque coefficients. (Data from ref. 6.)

$$C_{M,o}=\frac{3.70(s/a)^{1/10}}{R^{1/2}} \tag{8–12}$$

respectively.

Regime III: Turbulent Flow, Small Clearance. The turbulent counterpart of Regime I. The best theoretical and empirical equations for torque coefficient are

$$C_{M,o}=\frac{0.0622}{(s/a)^{1/4}R^{1/4}} \tag{8–13}$$

and

$$C_{M,o}=\frac{0.080}{(s/a)^{1/6}R^{1/4}} \tag{8–14}$$

respectively.

Regime IV: Turbulent Flow, Large Clearance. The turbulent counterpart of Regime II. The best theoretical and empirical equations for torque coefficient are

$$C_{M,o}=\frac{C_{IV}}{R^{1/5}} \tag{8–15}$$

where C_{IV} is a function of (s/a), as shown in figure 8–8(b), and

$$C_{M,o}=\frac{0.102(s/a)^{1/10}}{R^{1/5}} \tag{8–16}$$

respectively.

The particular flow regime that exists at any Reynolds number can be determined by plotting torque coefficient against Reynolds number from equations (8–9), (8–11), (8–13), and (8–15), as shown in figure 8–9 for several values of s/a. The discontinuities (changes in slope) in the lines of figure 8–9 indicate transition from one regime to another. In this figure, the flow regimes are determined by matching the slopes of the lines with

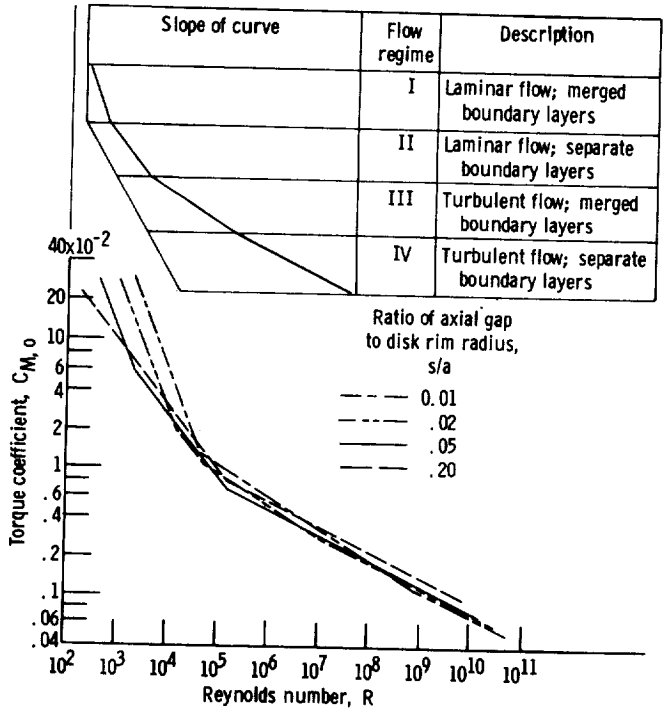

FIGURE 8–9.—Theoretical variation of torque coefficient with Reynolds number for no throughflow. (Data from ref. 6.)

those shown in the insert in the figure. Torque-coefficient values (ref. 6) determined experimentally with a 50.8-centimeter (20-in.) disk rotated in water and oil for several values of s/a verify the theory.

Throughflow

For the case of the rotating disk with throughflow, as in figure 8–6(b), the friction torque increases with the throughflow. This problem has been analyzed for low values of throughflow with regime-IV flow. In this case, it is assumed that the fluid enters the chamber near the centerline with no angular velocity and leaves at the rim with some angular velocity $K_o\omega a$. The symbol K_o represents the ratio of the angular velocity of the rotating core of gas to the angular velocity of the disk. The increase in torque, ΔM, over that without throughflow is the rate of change of angular momentum of the fluid flowing through the system:

$$\Delta M = 2\rho \frac{Q}{g} (K_o\omega a) a = 2\rho \frac{Q}{g} K_o\omega a^2 \tag{8–17}$$

where Q is the volumetric throughflow rate, in m^3/sec or ft^3/sec, in the clearance space on one side of the disk. The total torque for the throughflow case is then

$$M = M_o + \Delta M = \frac{C_{M,o}\rho\omega^2 a^5}{2g} + 2\frac{\rho}{g} QK_o\omega a^2 \tag{8–18}$$

The value of K_o is approximately 0.45 for s/a ratios from 0.025 to 0.12.

An assessment of the power loss can be obtained by calculating the friction torque of the throughflow case compared to that of the no-throughflow case:

$$\frac{M}{M_o} = 1 + \frac{2\rho QK_o\omega a^2}{\frac{1}{2} C_{M,o}\rho\omega^2 a^5} = 1 + \frac{4K_o}{C_{M,o}} \frac{Q}{\omega a^3} \tag{8–19}$$

Substituting equation (8–16) for $C_{M,o}$ yields

$$\frac{M}{M_o} = 1 + \frac{K_o R^{1/5}}{0.0255(s/a)^{1/10}} \frac{Q}{\omega a^3} = 1 + 39.2 \frac{K_o}{(s/a)^{1/10}} \Upsilon \tag{8–20}$$

where Υ is a dimensionless throughflow number defined as

$$\Upsilon = \frac{Q}{\omega a^3} R^{1/5} \tag{8–21}$$

According to the data of reference 7, equation (8–20) predicts values that are somewhat high; moreover, the effect of s/a is not accurately

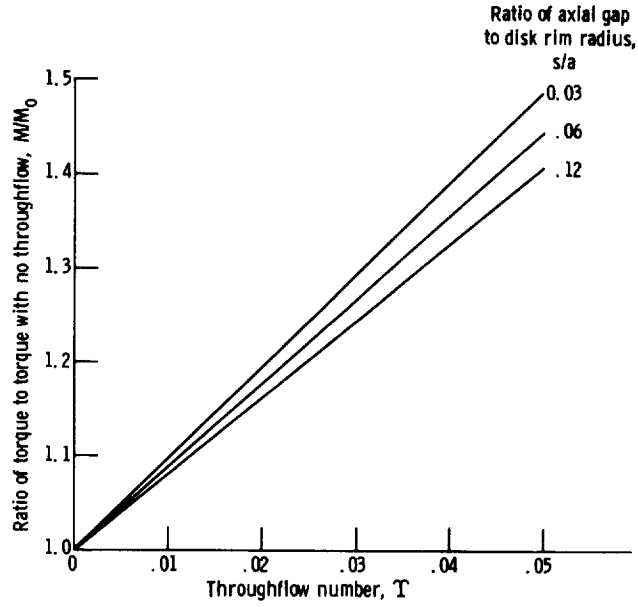

FIGURE 8–10.—Empirical variation of torque with throughflow number. (Data from ref. 7.)

given by $(s/a)^{1/10}$. Empirically, the test data are represented to within ± 5 percent by the relation

$$\frac{M}{M_o} = 1 + 13.9K_o \frac{\Upsilon}{(s/a)^{1/8}} \tag{8–22}$$

Equation (8–22) is plotted in figure 8–10 for several s/a values.

PARTIAL-ADMISSION LOSSES

Full-admission axial-flow turbines are used for most applications; however, unusual conditions sometimes arise for which a partial-admission turbine may be a better choice. If, for example, the design mass-flow rate is so small that a normal full-admission design would give very-small blade heights, then it may be advantageous to use partial admission. The losses due to partial admission with long blades may be less than the leakage and low Reynolds-number losses of the full-admission turbine having short blades. In addition, for a given rotative speed, partial admission allows the freedom of larger diameter and higher blade-jet speed ratios. Also, the use of partial admission may be a convenient way to reduce power output

of an existing full-admission turbine (physically block some of the stator passages). In general, partial-admission turbines have high specific-work output and low volumetric-flow rates.

As mentioned previously in this chapter, the partial-admission losses are the pumping loss in the inactive blade channels and the filling-and-emptying loss encountered as the blades pass through the active sector. This latter loss has been referred to as expansion, scavenging, or sector loss. The mechanisms of partial-admission losses are not clearly or fully understood, but they do result in a decrease in output power and efficiency when compared to the same turbine operating with full admission.

The pumping loss is that loss caused by the inactive blades rotating in a fluid-filled casing, and expressions for it are somewhat similar in form to, and often combined with, the expression for the disk-friction loss. These expressions all seem to trace back to reference 8, where the results of several experimental investigations are summarized. The equations for estimating pumping-power loss that resulted from these investigations showed that the effects of blade height and diameter on the pumping-power loss are quite uncertain, as evidenced by variations in the exponents on these terms. Further, the nature and location of obstructions (adjacent blade rows, casing wall, etc.) or lack of such in the vicinity of the three open sides of the blade channel were accounted for only by differences in the empirical loss coefficient. Therefore, it appears that a generally applicable expression for pumping-power loss is yet to be found.

The one equation perhaps most often used is

$$P_p = K_p \rho U_m^3 l^{1.5} D_m (1-\epsilon) \tag{8-23}$$

where

P_p	pumping-power loss, W; (ft)(lb)/sec
K_p	pumping-power loss coefficient, $1/m^{1/2}$; $(lbf)(sec^2)/(lbm)(ft^{3/2})$
U_m	blade mean-section speed, m/sec; ft/sec
l	blade height, m; ft
D_m	blade mean-section diameter, m; ft
ϵ	active fraction of stator-exit area

The value of the coefficient K_p as reported in reference 8 and converted to the units used herein is 3.63 $l/m^{1/2}$, or 0.0105 $(lbf)(sec^2)/(lbm)(ft^{3/2})$, for an unenclosed rotor. For the same rotors enclosed, the coefficient values were one-quarter to one-half of the above values. More recently, the combined disk-friction and pumping losses for a single-stage rotor enclosed by the turbine housing were reported in reference 9. If a disk-friction loss estimated by equation (8–7) is subtracted from the combined losses of reference 9 and if the remaining loss is converted to the form of equation (8–23), the coefficient K_p is found to be 5.92 $l/m^{1/2}$, or 0.0171 $(lbf)(sec^2)/(lbm)(ft^{3/2})$. This is significantly higher than the coefficients

reported in reference 8, and the difference is attributed to primarily the lack of an adequate loss model.

The other partial-admission loss shall herein be called the sector loss. Imagine a blade channel as it just starts to enter the active sector. It is filled with relatively stagnant fluid that must be pushed out by the high-momentum fluid leaving the nozzle. This scavenging will continue until the blade channel is completely within the active sector. As the blade channel passes out of the active sector, a second sector loss occurs. As the inlet to the blade channel is cut off from the nozzle active arc, less and less high-momentum fluid enters the channel. Since this fluid has the entire blade channel area to flow into, it is rapidly diffused as it flows through the rotor. These losses cause an overall decrease in the momentum of the fluid passing through the rotor, thus decreasing the available energy of the fluid. It was reported in reference 10 that this decrease in momentum may be found by multiplying the rotor-exit momentum by a loss coefficient

$$K_s=\left(1-\frac{p}{3f}\right) \tag{8–24}$$

where p is the rotor-blade pitch, in m or ft, and f is the nozzle active arc length, in m or ft. Effectively, K_s is a rotor velocity coefficient that accounts for the sector loss.

The effect of the sector loss on turbine efficiency is determined as follows. With the use of equations (2–6) and (2–14), from volume 1, and the associated velocity diagram geometry, we can express the specific work of an axial-flow turbine as

$$\Delta h'=\frac{U_m}{gJ}\left(W_{u,1}-W_{u,2}\right)=\frac{U_m}{gJ}\left(W_1\sin\beta_1-W_2\sin\beta_2\right) \tag{8–25}$$

where

$\Delta h'$	turbine specific work, J/kg; Btu/lb
W_u	tangential component of relative velocity, m/sec; ft/sec
W	relative velocity, m/sec; ft/sec
β	fluid relative angle measured from axial direction, deg

The subscripts 1 and 2 refer to the rotor inlet and exit, respectively. For an impulse turbine (which most partial-admission turbines are), where $\beta_1=-\beta_2$,

$$\Delta h'=\frac{U_m}{gJ}W_1\sin\beta_1(1+K_w) \tag{8–26}$$

where K_w is the rotor relative-velocity ratio W_2/W_1 for the full-admission turbine. For the partial-admission turbine, applying the sector loss

coefficient yields

$$W_2 = K_w K_s W_1 \tag{8–27}$$

So, for the partial-admission turbine,

$$\Delta h'_{pa} = \frac{U_m}{gJ} W_1 \sin \beta_1 (1 + K_w K_s) \tag{8–28}$$

Since efficiency is

$$\eta = \frac{\Delta h'}{\Delta h_{id}} \tag{8–29}$$

where Δh_{id} is the turbine ideal specific work, in J/kg or Btu/lb, the efficiency of the partial-admission turbine with respect to that of the full-admission turbine is

$$\frac{\eta_{pa}}{\eta} = \frac{\Delta h'_{pa}}{\Delta h'} \tag{8–30}$$

Substituting equations (8–26) and (8–28) into equation (8–30) then yields

$$\eta_{pa} = \eta \frac{1 + K_w K_s}{1 + K_w} \tag{8–31}$$

The efficiency penalty expressed by equation (8–31) accounts for the sector loss only; the pumping loss discussed earlier will reduce the overall efficiency further. Equation (8–24) indicates that a partial-admission turbine rotor should have closely spaced blades to reduce the sector loss; however, as more blades are added to the rotor, the blade profile loss will increase. Also, the effect of the number of rotor blades on the pumping loss is not known. Therefore, the complete optimization of a partial-admission design cannot be done analytically at present.

In the study of reference 9, the efficiency of a small axial-flow turbine was determined over a range of admissions from 12 to 100 percent. The total loss due to partial-admission operation was taken as the difference between the full- and the partial-admission efficiencies. The blade pumping and disk-friction losses were measured separately and were subtracted from the total partial-admission loss to give what was called other partial-admission losses. These other losses include the sector loss and any loss due to leakage from the active sector to the inactive sector. The partial-admission losses of reference 9 are plotted against admission-arc fraction in figure 8–11. The combined pumping and disk-friction loss increased with decreasing arc fraction, while the other losses remained nearly constant over the range of arcs tested.

Predicted efficiencies (from ref. 10) are plotted against blade-jet speed

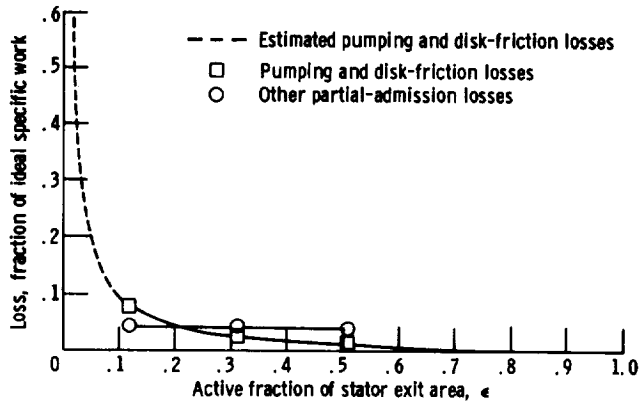

FIGURE 8–11.—Variation of partial-admission losses with active fraction of stator area. (Data from ref. 9.)

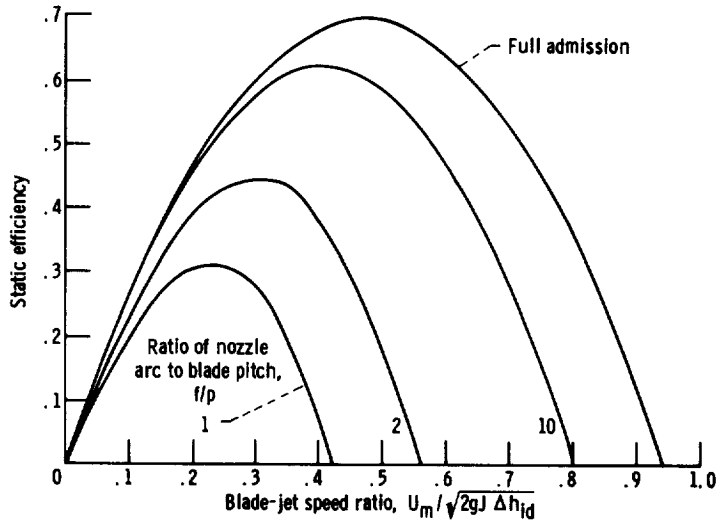

FIGURE 8–12.—Design-point performance of partial- and full-admission turbines. (Data from ref. 10.)

ratio (see discussion in vol. 1, ch. 2) in figure 8–12 for a particular turbine operating with full admission and with three different amounts of partial admission. The expected reduction in peak efficiency with reduced arc of admission is seen. The important thing to note from this figure is the reduction in optimum blade-jet speed ratio as admission arc is reduced. Aerodynamic efficiency is a maximum at a blade-jet speed ratio of 0.5,

irrespective of admission arc, and decreases with decreasing blade speed. Blade-pumping and disk-friction losses, which decrease with decreasing blade speed, become a larger part of the gross aerodynamic power as admission arc decreases. Therefore, as admission arc is reduced, the maximum net output power (aerodynamic power minus blade-pumping and disk-friction power) is obtained at lower blade speeds. Thus, for the design of a partial-admission turbine, the partial-admission losses must be factored into the design before an optimum or near-optimum blade-jet speed ratio can be selected.

INCIDENCE LOSS

The incidence loss is that loss which occurs when the gas enters a blade row (either stator or rotor) at some angle other than the optimum flow angle. Flow incidence would normally only occur at off-design conditions, since, theoretically at least, all gas and blade angles are matched at the design condition. The nomenclature used when speaking of incidence is shown in figure 8–13. The dashed line running through the blade profile is the camber line and defines the blade inlet angle. The incidence angle is defined as

$$i = \alpha - \alpha_b \tag{8–32}$$

where

i incidence angle, deg
α fluid flow angle from axial direction, deg
α_b blade inlet angle from axial direction, deg

The fluid flow angle must be the absolute angle for stators and the relative angle for rotors. The incidence angle may be positive or negative, as indicated in figure 8–13. The sign of the incidence angle is important because cascade tests have shown that the variation of loss with incidence angle is different for positive and negative angles.

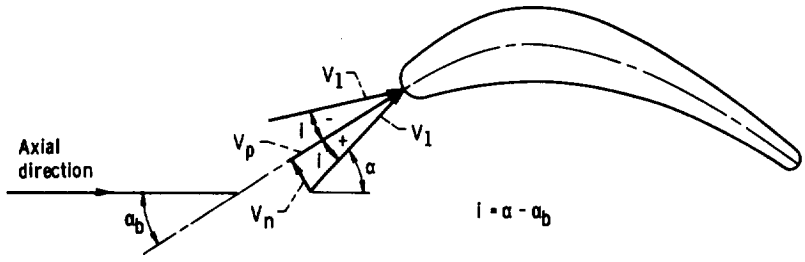

FIGURE 8–13.—Blade incidence nomenclature.

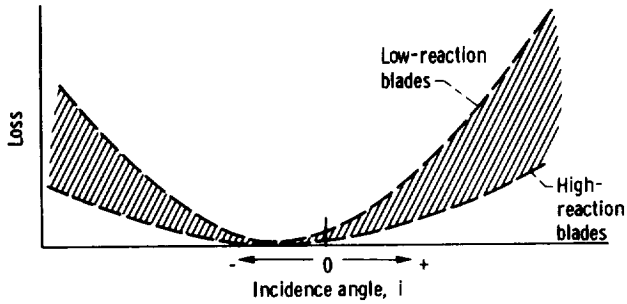

FIGURE 8–14.—Characteristics of blade incidence loss.

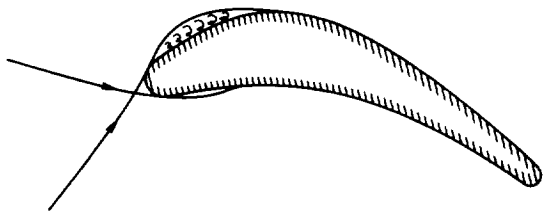

FIGURE 8–15.—Local flow separation on blade surface.

The general nature of the variation of incidence loss with incidence angle is shown by figure 8–14, which represents a summary of cascade test results. The loss curve is not symmetrical about the zero incidence angle, but shows a loss that is larger for positive incidence than for negative incidence. This may be due to some local separation on the suction surface at large positive incidence, as indicated in figure 8–15, and the lack, or smaller area, of separation at the same value of negative incidence. Also, blades in which the mean acceleration of the gas flow is large (high-reaction blades) have a wide range of incidence over which loss is low, whereas low-reaction blades have higher losses for the same incidence range.

Another thing to be noted from figure 8–14 is that the minimum loss does not occur at zero incidence, but at some small amount of negative incidence. This may be explained by the sketch of figure 8–16. The stagnation streamlines for two inlet flow angles are shown; one at zero incidence and the other at some small negative incidence with respect to the blade inlet angle. Both tests and theory show that the stagnation streamline curves upward as the flow impacts on the blade leading edge, and the true zero incidence occurs when there is some negative incidence

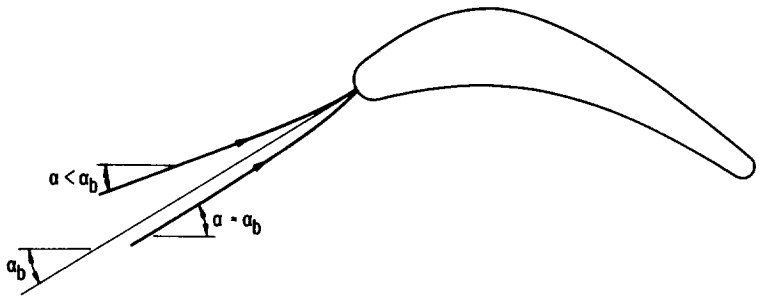

FIGURE 8–16.—Curvature of stagnation streamline at blade inlet.

relative to the free-stream flow. The incidence angle at minimum loss is usually $-4°$ to $-8°$. Because of this, some turbine designers design their blades with a small amount of negative incidence, while others do not because of the small difference involved.

The magnitude of the incidence loss takes on importance when the off-design performance of a turbine must be predicted. A method for determining incidence loss based on test data is described in reference 11. An analytical method is described here with the aid of figure 8–13. The inlet velocity V_1 can be resolved into a component V_n normal to, and a component V_p parallel to the blade inlet direction (camber line at inlet). If it is assumed that the parallel component passes through the blade row without any entry loss and that the normal component is entirely lost, the recovered kinetic energy is

$$\frac{V_p^2}{2gJ}=\frac{V_1^2}{2gJ}\left(\frac{V_p}{V_1}\right)^2=\frac{V_1^2}{2gJ}\cos^2 i \tag{8–33}$$

and the kinetic-energy loss due to incidence is

$$L_i=\frac{V_1^2}{2gJ}(1-\cos^2 i) \tag{8–34}$$

In order to account for the differences in loss variation with positive and negative incidence, the effect of blade-row reaction, and the minimum loss not occurring at zero incidence, equation (8–34) has been generalized to

$$L_i=\frac{V_1^2}{2gJ}[1-\cos^n (i-i_{opt})] \tag{8–35}$$

where i_{opt} is the optimum (minimum-loss) incidence angle. This type of equation has proved satisfactory when used in off-design performance

prediction methods such as that of reference 12. Where specific incidence-loss data are lacking, values of $n=2$ for negative incidence and $n=3$ for positive incidence have been used satisfactorily.

REFERENCES

1. HORLOCK, JOHN H.: Axial Flow Turbines. Butterworth Inc., 1966.
2. HOLESKI, DONALD E.; AND FUTRAL, SAMUEL M., JR.: Effect of Rotor Tip Clearance on the Performance of a 5-Inch Single-Stage Axial-Flow Turbine. NASA TM X-1757, 1969.
3. KOFSKEY, MILTON G.; AND NUSBAUM, WILLIAM J.: Performance Evaluation of a Two-Stage Axial-Flow Turbine for Two Values of Tip Clearance. NASA TN D-4388, 1968.
4. KOFSKEY, MILTON G.: Experimental Investigation of Three Tip-Clearance Configurations Over a Range of Tip Clearance Using a Single-Stage Turbine of High Hub- to Tip-Radius Ratio. NASA TM X-472, 1961.
5. HONG, YONG S.; AND GROH, F. G.: Axial Turbine Loss Analysis and Efficiency Prediction Method. Rep. D4-3220, Boeing Co., Mar. 11, 1966.
6. DAILY, J. W.; AND NECE, R. E.: Chamber Dimension Effects on Induced Flow and Frictional Resistance of Enclosed Rotating Disks. J. Basic Eng., vol. 82, no. 1, Mar. 1960, pp. 217-232.
7. DAILY, J. W.; ERNST, W. D.; AND ASHEDIAN, V. V.: Enclosed Rotating Disks with Superposed Throughflow: Mean Study and Periodic Unsteady Characteristics of the Induced Flow. Rep. R-64-16, Massachusetts Inst. Tech. (AROD-2500-2, AD-443060), Apr. 1964.
8. STODOLA, A. (LOUIS C. LOEWENSTEIN, TRANS.): Steam and Gas Turbines. Vol. I. McGraw-Hill Book Co., Inc., 1927. Reprinted by Peter Smith, 1945, pp. 200-201.
9. KLASSEN, HUGH A.: Cold-Air Investigation of Effects of Partial Admission on Performance of 3.75-Inch Mean-Diameter Single-Stage Axial-Flow Turbine. NASA TN D-4700, 1968.
10. STENNING, ALAN H.: Design of Turbines for High-Energy-Fuel Low-Power-Output Applications. Rep. 79, Dynamic Analysis and Control Lab., Massachusetts Inst. Tech., Sept. 30, 1953.
11. AINLEY, D. G.; AND MATHIESON, G. C. R.: An Examination of the Flow and Pressure Losses in Blade Rows of Axial-Flow Turbines. R&M-2891, Aeronautical Research Council, Gt. Britain, 1955.
12. FLAGG, E. E.: Analytical Procedure and Computer Program for Determining the Off-Design Performance of Axial-Flow Turbines. NASA CR-710, 1967.

SYMBOLS

A	area on one side of rotor disk, m^2; ft^2
a	disk rim radius, m; ft
C_{II}	coefficient used to evaluate $C_{M,o}$ in regime II by equation (8–11)
C_{IV}	coefficient used to evaluate $C_{M,o}$ in regime IV by equation (8–15)
C_f	fluid shear-stress coefficient
$C_{M,o}$	torque coefficient with no throughflow
D	diameter, m; ft
f	nozzle active arc length, m; ft
g	conversion constant, 1; 32.17 (lbm) (ft)/(lbf) (sec^2)
$\Delta h'$	turbine specific work, J/kg; Btu/lb
Δh_{id}	turbine ideal specific work based on ratio of inlet-total pressure to exit-static pressure, J/kg; Btu/lb
i	incidence angle, deg
J	conversion constant, 1; 778 (ft) (lb)/Btu
K_{df}	disk-friction power-loss coefficient
K_o	ratio of rotating-core angular velocity to disk angular velocity
K_p	pumping power loss coefficient, $1/m^{1/2}$; (lbf) (sec^2)/(lbm) ($ft^{3/2}$)
K_s	sector loss coefficient
K_w	rotor velocity coefficient for full-admission impulse turbine
L_i	incidence loss, J/kg; Btu/lb
l	blade height, m; ft
M	frictional resistance torque for both sides of rotor disk, N-m; lb-ft
N	rotative speed, rad/sec; rev/min
n	exponent in equation (8–35)
P_{df}	disk-friction power loss, W; Btu/sec
P_p	pumping power loss, W; Btu/sec
p	rotor-blade pitch, m; ft
Q	volumetric throughflow rate, m^3/sec; ft^3/sec
R	Reynolds number
r	radius, m; ft
s	axial distance between rotor disk and casing, m; ft
U	blade speed, m/sec; ft/sec
V	absolute velocity, m/sec; ft/sec
W	relative velocity, m/sec; ft/sec
α	fluid flow angle from axial direction, deg
α_b	blade inlet angle from axial direction, deg
β	fluid relative angle measured from axial direction, deg
ϵ	active fraction of stator exit area
η	turbine static efficiency
μ	dynamic viscosity, (N) (sec)/m^2; lb/(ft) (sec)
ρ	density, kg/m^3; lb/ft^3

τ	fluid shear stress, N/m^2; lb/ft^2
Υ	throughflow number defined by equation (8–21)
ω	angular velocity, rad/sec

Subscripts:

m	mean section
n	component normal to blade inlet direction
o	no throughflow
opt	optimum
p	component parallel to blade inlet direction
pa	partial admission
r	disk rim
u	tangential component
1	rotor inlet blade-row inlet
2	rotor exit

☆ U.S. GOVERNMENT PRINTING OFFICE: 1974 O—523-092